RADIATION EFFECTS ON MICROELECTROMECHANICAL SYSTEMS

By

Wenjun Liao

Dissertation

Submitted to the Faculty of the

Graduate School of Vanderbilt University

In partial fulfillment of the requirements

for the degree of

DOCTOR OF PHILOSOPHY

in

Electrical Engineering

August 31, 2018

Nashville, Tennessee

Approved:

Michael L. Alles, Ph.D.

Jimmy L. Davidson, Ph.D.

Daniel M. Fleetwood, Ph.D.

Sokrates T. Pantelides, Ph.D.

Robert A. Reed, Ph.D.

Ronald D. Schrimpf, Ph.D.

Enxia Zhang, Ph.D.

To my amazing daughter, Allison Liao, wise beyond her years
And
To my beloved wife, Jingjing Bu, infinitely supportive

ACKNOWLEDGEMENTS

TABLE OF CONTENTS

LIST OF TABLES

LIST OF FIGURES

NOMENCLATURE

Abbreviation/Symbol	Description
MEMS	Microelectromechanical System
TID	Total ionizing dose
DD	Displacement Damage
pMUT	Piezoelectric Micromachined Ultrasonic Transducers
2D	Two-dimensional
SiC	Silicon Carbide
SEE	Single Event Effect
2DACs	Two-dimensional atomic crystals
AFM	Atomic force microscopy
MoS_2	Molybdenum disulfide
PZT	Lead Zirconate Titanate
CTE	Coefficients of Thermal Expansion
TRIM	Transport of Ions in Matter
SRIM	The Stopping and Range of Ions in Matter
GEO	Geosynchronous Orbit
LEO	Low Earth Orbit
rad	Radiation Absorbed Dose
FEM	Finite Element Method
MC	Monte Carlo
DUT	Device Under Test
DC	Direct Current
AC	Alternating Current
DTRA	Defense Threat Reduction Agency
IV	Current versus Voltage
MOS	Metal on Semiconductor

CHAPTER I

1. INTRODUCTION

1.1 Overview

The pervasiveness of Micro-Electro-Mechanical Systems (MEMS), along with the advancement in materials technologies, have stimulated increased interest in understanding the potential of these technologies for use in radiation environments [1]. MEMS technologies will fill an increasing demand for lighter, smarter components and systems. The dramatic reduction in size and power consumption provided by MEMS make these ideally suited for a range of application areas including consumer, medical, military, and space devices [2]. Since MEMS technology is new, most of the research has been centered on technological advances and demonstrating the potential benefits available with MEMS, with little emphasis placed on understanding their reliability. The reliability of MEMS utilized within a space system is compounded by the potentially harsh radiation environment. There is little research about reliability of piezoelectric MEMS and electrothermal MEMS in radiation environments [3]. With the possibility that piezoelectric MEMS and electrothermal MEMS will be used to enhance current capabilities for systems operating in harsh radiation environments comes the reality that these MEMS must be known to operate predictably in those environments. This research directly contributes to the reliability knowledge base.

Isolated two-dimensional (2D) materials are especially suitable for applications in ultra-miniaturized MEMS [1]. However, as their scale decreases, MEMS become potentially more sensitive to changes in their electrical and physical properties. As the ultimate thin-film geometry, 2DACs (two-dimensional atomic crystals) present unique considerations for the study of radiation effects. It is very important to understand the differences between bulk and 2D materials in radiation environments and their influence on MEMS. SRIM, a Monte Carlo computer code to calculate how a moving ion transfers its energy to the target atoms in bulk materials, cannot directly be applicable to two dimensional (2D) systems. A new Monte Carlo computer code is needed to describe how an ion transfers its energy to 2D materials.

The dramatic reductions in size and power consumption offered by MEMS offer compelling advantages for potential adoption in space and military systems. The understanding

of extreme environment operational capabilities, and models of the observed effects provided by this research are necessary factors to enable capitalization on these benefits.

1.2   Objectives and Approach

The overall objective of the research is to develop a fundamental understanding of the interaction mechanisms of ionizing and displacement damage with MEMS. This work is significant both because the topics have not been studied in detail and because of the depth at which this work will investigate the interaction mechanisms.

The interactions between radiation effects and MEMS have been mainly investigated by experimental methods. The MEMS mechanical and electronic property changes due to radiation exposure are observed by using experimental characterization and the parametric changes are calculated.

The four specific objectives addressed in this dissertation are:

1. Investigate the radiation effects on piezoelectric micromachined ultrasonic transducers, including charge trapping influences on electrical properties and mechanical properties. Study the interaction mechanism of dielectric charges with piezoelectric MEMS dynamic responses.
2. Investigate the radiation effects on electrothermal microscanners, including charge trapping influences on electrical properties and mechanical properties. Study the interaction mechanism of dielectric charges with electrothermal MEMS static responses.
3. Investigate displacement damage effects on ultra-thin membranes, including displacement damage scaling effects and development of a new measurement method to stop ions in ultra-thin membranes.
4. Develop a framework for evaluating the displacement damage mechanisms of energetic ions onto 2DACs. This includes the analysis of carbon atoms movements and a Monte Carlo simulation methodology for defect density calculation.

1.3   Structure of the dissertation

This dissertation is organized into six chapters. Chapter 2 contains a review of relevant literature pertaining to the research in this dissertation. Chapter 3 discusses the radiation effects mechanisms of pMUTs, including evaluation of the dielectric layer charging and the data analysis methodology used, in particular the determination of the relationship between resonant frequency and trapped charge density. Chapter 4 discusses the interaction mechanisms of TID with the electrothermal microscanners. Chapter 5 discusses the displacement damage on ultra-thin materials, including SiC membranes and 2DACs. A Monte Carlo simulation methodology is used to evaluate displacement damage in 2DACs. Chapter 6 summarizes the results and presents recommendations for future work.

2. BACKGROUND

2.1 Radiation Environment

Radiation can originate from several sources encountered by a device over its lifetime. For this research, the sources can be classified into two environments: space radiation and nuclear reactor environments. A thorough description of these environments is provided by Ma [4] and Olesen [5]. These radiation environments will briefly be described in the following sections.

2.1.1 Space Radiation

Devices operating on satellites or other spacecraft are subjected to several ionizing radiation sources. The type of radiation encountered is dictated by the level of orbit of the spacecraft. The space radiation environment near the Earth's surface, usually 1 to 10 Earth radii, is of most interest since most spacecraft orbits range in altitude from 100 miles to 22,300 miles (geostationary orbit). Within this range of orbits spacecraft will encounter electrically charged particles trapped by the Earth's magnetosphere (Figure 2.1) and high-energy particles from cosmic rays. The two types of radiation commonly encountered within the space arena are trapped electrons and trapped protons.
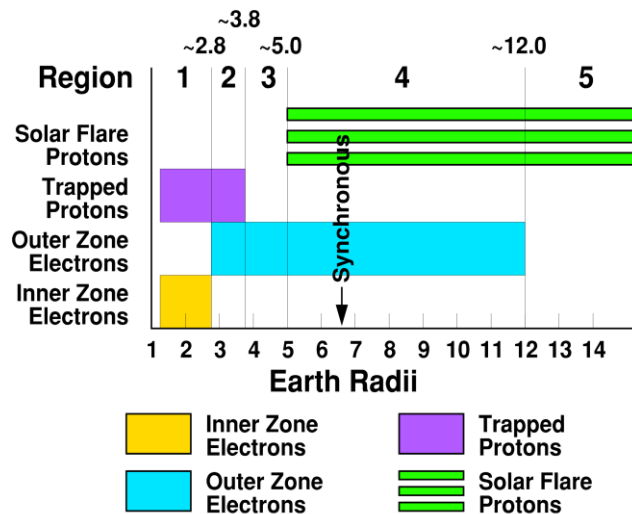
Figure 2.1. The charged particles trapped by the Earth's magnetosphere (adapted from [6]).

Energies of electrons trapped in the Earth's magnetosphere can range from low energies, kilo-electron-Volts (keV), to around 5 mega-electron-volts (MeV). These electrons are trapped in a region termed the Van Allen Belts which is centered on the geomagnetic equator and extends from approximately 1.2 to 11 Earth radii [6]. The region is commonly separated into two regions, the inner and outer belts. Although there is no distinct division, the outer extent of the inner belt is commonly taken to be 10,000 km. Energies of protons trapped in the Earth's magnetosphere can range up to approximately 800 MeV. Trapped protons are generally found in the same region as are the trapped electrons; however, the regions of high flux are not coincidental for the two particles.

The amount of total ionizing dose accumulated by a device in the space environment depends on the orbit of the satellite, the length of the mission, the solar activity and the amount of shielding on the satellite.

2.1.2   Nuclear Reactors

Nuclear power plants are a source of radiation. Electronics used to control and operate the plant are continuously subjected to radiation. A thorough discussion of the radiation environment within a nuclear reactor is provided by Gover [7]. The containment building of a nuclear reactor houses most of the devices that must be radiation hard. Therefore, the radiation environment of interest is within the containment building. The radiation present within the containment building is primarily composed of gamma rays; however, neutrons are also present. In a possible accident the radiation environment can change drastically and therefore must be considered when designing control devices.

These two radiation environments have ionizing radiation and high energy ions present (Table 2.1). This commonality steered this research toward exploring the effects of ionizing radiation and displacement damage on MEMS. Cumulative effects of ionizing and non-ionizing radiation will alter the electrical and mechanical properties of the constituent materials and alter device operation and long-term reliability. The operating principles of many of these devices may provide inherent tolerance to single-event transient radiation effects (SEE). The supporting circuitry will be the consideration for SEE and is not the primary interest of the proposed research.

Table 2.1 Radiation sources in space and nuclear reactors and their possible damage mechanisms to MEMS.

Environment Sources	Space Radiation			Nuclear Reactors
	Earth's Radiation Belts	Galactic Cosmic Rays	Solar Heavy Ions	
Protons	✔	✔	✔	
Electrons	✔			✔
Heavy Ions		✔	✔	
Neutrons				✔
Gamma Rays				✔

	TID, DD, SEE		DD, SEE		TID

2.2   Microelectromechanical Systems

MEMS are among the fastest growing technology areas. With an average annual growth rate of more than 20%, the MEMS industry is expected to reach over $29 billion by the year 2024 [8]. They not only provide better substitute solutions for many conventional technologies, but also have been proven to be key enabling solutions for new applications in consumer products, health care, military, transportation, telecommunication and space industries. Medical/biomedical instrumentation, automotive industry, and consumer products applications will continue to dominate the MEMS market in the near future. As they continue to expand, the applications of MEMS technology can be virtually everywhere.

MEMS are promising devices for space systems because of their small size, low mass, possible integration with integrated circuits, low power consumption and the ability to perform non-electronic functions: e.g., sensing and actuation [9]. In general, typical MEMS include mechanical components, such as cantilevers and membranes; electrical components, such as control circuits; and energy conversion components, such as piezoelectric materials that are used for sensing and actuation (Figure 2.2). The idea behind the application of electro-mechanical devices is a correlated energy conversion between the mechanical and electrical (sensors) or electrical and mechanical (actuators) components. These relationships can be accomplished in

various manners. The characteristics of these parts may be affected in the space radiation environment [10].
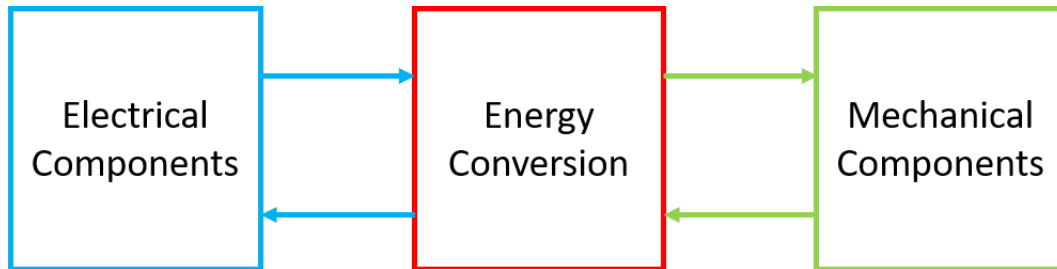
Figure 2.2 The MEMS lumped model.

MEMS can be operated using a wide variety of physical energy conversion principles. The most common principles are electrostatic, thermal, electromagnetic and piezoelectric. The degradation of MEMS devices due to radiation is a complex interplay of changes to the sensing and actuation physical principle [3]. MEMS operating on electrostatic principles can be highly sensitive to charge accumulation in dielectric layers, especially for designs with dielectrics located between moving parts [11]. In contrast, thermally and electromagnetically actuated MEMS are typically much more radiation tolerant [12], [13]. Piezoelectric MEMS were thought to be tolerant to radiation, especially to total-ionization-dose (TID) effects [3]. But recent work discovered that TID effects can significantly affect piezoelectric materials [14]. In this research, we will focus on radiation effects on piezoelectric and electrothermal MEMS.

How can radiation effects influence MEMS? Normally, TID causes dielectric layer charging. These charges change the properties of electrical components. The changes of electrical properties can lead to changes in mechanical components through energy conversion mechanisms. DD can introduce damage to materials and changes properties of mechanical components. These changes can also be reflected in electrical components (Figure 2.3).

The study of radiation effects on electronic components has a decades-long history, while the study of radiation effects in mechanical parts is more limited. The mechanical components

are usually thought to be radiation hard [10]. But as MEMS device dimensions continue to shrink and new materials are added, the mechanical components are more easily affected by the irradiation. In this research, how radiation interacts with the ultra-thin membrane and 2D materials and how defects change their mechanical properties are investigated.
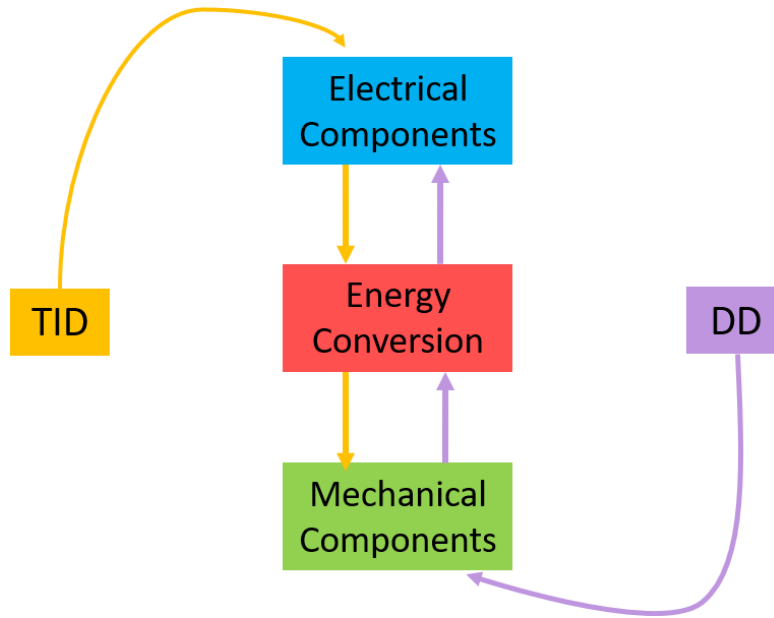
Figure 2.3 Effects of TID and DD on MEMS.

2.3   Radiation Effects on Electrostatic MEMS

For electrostatic MEMS devices, the main failure mode at high radiation doses is the accumulation of charge in dielectric layers, which can move the mechanical structure and change the resonant frequency of the device essentially by applying an electrostatic force. The failure may appear mechanical, e.g., a stuck comb-drive, but the root cause is electrical [3]. For a given device, TID is the main radiation parameter that leads to charging.

Photons, electrons, and protons create electron-hole pairs in dielectrics through ionization. The carriers that survive the initial recombination move in response to the local electric field, with electrons typically being much more mobile than holes. Carriers that become trapped have a decay time of hours or days. Details of charging depend on the geometry, secondary electrons emitted from nearby surfaces, and vary significantly with the applied bias.

8

Figure 2.4 shows the charging effects on electrostatic MEMS. The left part is the simplified MEMS model with electrode and dielectric layer. The right part is the equivalent dielectric layer in electrical MEMS. The thickness of these dielectric layers are t_d and the distance between these two dielectric layers is g. ρ_1 and ρ_2 are uniform surface charge sheets assumed to be present at the oxide-air interface of each dielectric layer. ε_d and ε_o are the dielectric constants of the dielectric layer and the air. The extra electrostatic force F_{ex} caused by the accumulated charge is [15]:

$$F_{ex} = \frac{A\varepsilon_0\left(t_d\left(\rho_1 - \rho_2\right)\right)^2 + 2AV_{bias}\varepsilon_d\varepsilon_0 t_d\left(\rho_1 - \rho_2\right)}{2\left(2t_d\varepsilon_0 + g\varepsilon_d\right)^2} \tag{2-1}$$
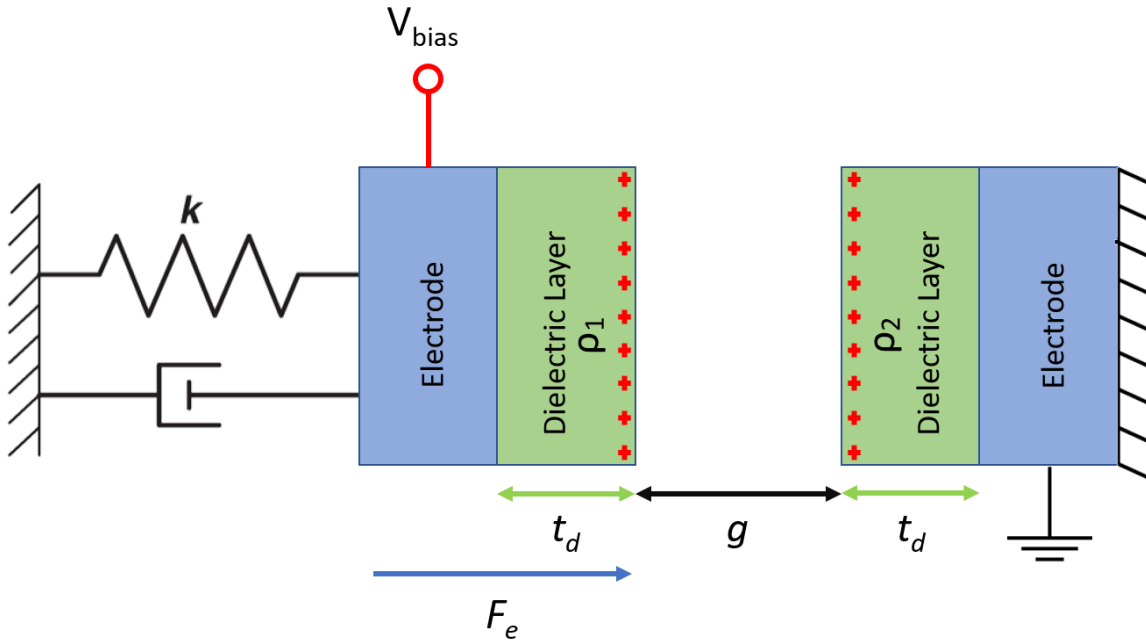
Figure 2.4 Charging effects on electrostatic MEMS.

From equation 2-1, we can get some important conclusions:

(1) The extra electrostatic force F_{ex} depends strongly on the electrical potential difference V_{bias}. Since dielectric layers might be floating in MEMS with no certain V_{bias}, the accumulated charges bring more uncertainty to the electrostatic MEMS application in

radiation environments.

(2) F_{ex} is proportional to the difference of surface charge densities $\rho_1 - \rho_2$.

(3) The MEMS equivalent displacement d_m caused by F_{ex} can be expressed as:

$$d_m = \frac{F_{ex}}{k} = \frac{F_{ex}(d_m)}{k} \tag{2-2}$$

k is the equivalent elastic constant of the MEMS. This equation shows the accumulated charges can cause static displacement of MEMS. F_{ex} is inversely proportional to the distance g between MEMS and equivalent dielectric layer and is a function of d_m.

Most electrostatically operated MEMS devices degrade between 10 and 100 krad(Si) [3]. Failures are often caused by electrostatic forces introduced by trapped charge in dielectric films. Those electrostatic forces can move the mechanical parts of MEMS and cause a stuck comb drive [16], and/or lead to snapped-down parallel plates [17] or change in calibration of capacitive sensors [16],[18].

Analog Devices and Motorola have both produced commercially available comb drive-based accelerometers. Accelerometers from both companies have been subjected to radiation testing by the Naval Research Lab [19]. A comb drive used as a microengine was also subjected to radiation testing at Sandia National Laboratories [20]. All the tests conducted have demonstrated that the operation of MEMS comb-drives is affected by radiation. A brief discussion on the relationship between dielectric charges and electrostatic forces will be undertaken prior to presenting the results of the radiation testing.

The "spring softening" is the change in the natural frequency f_0 of a MEMS structure due to presence of the electric field in surrounding the MEMS structure. The MEMS resonant frequency tuned by the electric field in Figure 2.4 can be expressed as

$$f_0' = \frac{1}{2\pi}\sqrt{\frac{k_{eff}}{m}} = \frac{1}{2\pi}\sqrt{\frac{k - \dfrac{\varepsilon A V(t)^2}{g^3}}{m}} \approx f_0\left(1 - \frac{\varepsilon A V(t)^2}{2kg^3}\right) \tag{2-3}$$

$V(t)$ can be expressed as:

$$V(t) = V_{DC} + V_{ac}\cos(\omega t)$$

Then the resonant frequency can be expressed as:

$$f_0' = f_0 \left(1 - \frac{\varepsilon A V(t)^2}{2kg^3} \right) = f_0 \left(1 - \frac{\varepsilon A}{2kg^3} \left(V_{DC}^2 + \frac{1}{2} V_{ac}^2 + 2 V_{DC} V_{ac} \cos(\omega t) - \frac{1}{2} V_{ac}^2 \cos(2\omega t) \right) \right) \qquad (2\text{-}4)$$

From this equation, we can see the MEMS resonant frequency is closely related to the static component V_{DC} and dynamic component V_{ac}. The TID effects can lead to fixed trapped charges in dielectric layer and change the static component V_{DC}, which can cause long-term resonant frequency shifts and then degrade MEMS performance. On the other hand, the real time radiation and electromagnetic interference in radiation environment can lead to an additional dynamic component V_{ac} to the MEMS and tune the resonant frequency.

2.4 Radiation Effects on Piezoelectric MEMS

Piezoelectric MEMS devices simultaneously achieve large force, high working frequency, high energy density, low power consumption, and no electromagnetic interference, which makes them suitable for applications in space or nuclear reactors. Furthermore, the extremely large piezoelectric and dielectric response of PZT presents an opportunity for integrating multiple functionalities at the micron and nanometer scale, including sensing and actuation capabilities, energy harvesting for self-powered devices, miniaturized multilayer capacitors, and logic control mechanical relays. For example, piezoelectric micro-mirror-based mass spectrometers can be used in space for materials analysis [21], and piezoelectric accelerometers can be used in small satellite systems for motion detection [22]. Radiation effects on lead zirconate titanate (PZT) have been reported [23], [24], but very little is known about piezoelectrically-actuated MEMS performance in radiation environments.

2.4.1 Piezoelectric Effects and Piezoelectric Micromachined Acoustic Sensor

Piezoelectric effects reflect the ability of certain materials to generate an electric charge in response to applied mechanical stress. In other words, the piezoelectric materials can sense the vibration and transfer it to charges on the surface. Piezoelectric sensors utilize this property to sense movements and transfer it to electric signals.

One of the unique characteristics of the piezoelectric effect is that it is reversible. When

11

piezoelectric material is placed under mechanical stress, a shifting of the positive and negative charge centers in the material takes place, which then results in an external electrical field. The generation of stress when an electric field is applied is called the inverse piezoelectric effect. Piezoelectric actuators utilized this property to transfer electric signals to movements.

Ultrasound can be excited by many different methods, including the piezoelectric effect, magnetostriction, and the photoacoustic effect. Of these, the piezoelectric effect is the most common. A typical structure of a conventional piezoelectric ultrasonic transducer usually has a layer of piezoelectric material sandwiched by thin high conductivity electrode layers, of e.g., Au or Pt, often with an underlying adhesion layer e.g., of Cr or Ti, and connected with electrical wires.

The effective piezoelectric response of PZT thin films is usually very different from that of bulk PZT, particularly because of the in-plane clamping of the film by the substrate, as well as from the residual stress in the film. By releasing the substrate beneath the thin film PZT, the mechanical constraints near the bottom interface of the PZT are reduced and the piezoelectric domain walls can more freely respond to the electric field and contribute more to the dielectric and piezoelectric properties, leading to better performance of the pMUTs. Partially unclamping diaphragm edges, optimizing electrode configurations and even adding DC bias have also been used to increase the coupling coefficients and acoustic output of pMUTs [25].

Intrinsic stress in the membrane generated during fabrication can affect the resonant frequency dramatically. In the case of an edge-clamped circular diaphragm with low intrinsic stress, the membrane behaves as a plate with the resonant frequencies, f, given as [26]

$$f = \frac{\alpha}{2\pi\gamma^2}\sqrt{\frac{D_E}{\rho h}}$$ (2-5)

$$D_E = \frac{Eh^3}{12(1-v^2)}$$

where α is the resonance mode constant, γ is the radius of the diaphragm, D_E is the flexural rigidity, ρ is the effective density of the diaphragm, h is the diaphragm thickness, E is the effective Young's modulus, and v is Poisson's ratio. With high intrinsic stress, T, the stress can

dominate over the flexural rigidity, hence the membrane behaves as a membrane with no bending stiffness with the resonant frequencies given as [27]

$$f = \frac{\alpha}{2\pi\gamma} \sqrt{\frac{T}{\rho h}} \qquad (2\text{-}6)$$

The high sensitivity of the resonant frequency to the residual stress of the membrane may cause difficulties during the design process.

In lumped element models, the coupling between the various energy domains is realized by using equivalent two-port models of the physical system. An equivalent circuit model is constructed by lumping the distributed energy storage and dissipation into ideal generalized one-port circuit elements. An impedance analogy is employed, in which elements that share a common effort are connected in parallel, whereas those sharing a common flow are connected in series. For a pMUT, three different energy domains are involved: electrical, mechanical, and acoustic. The electromechanical sensor consists of a clamped PZT composite diaphragm. The composite diaphragm senses motion and outputs an applied ac voltage. The primary purpose of the piezoelectric diaphragm is to sense volume displacements causing by the air into and out of the cavity, which represents a conversion from the mechanical to the acoustic energy domain. Consequently, the frequency range of the analysis is limited from dc to somewhat beyond the fundamental vibration mode of the composite diaphragm, but less than the natural frequency of any higher-order modes [28]. Linear composite plate theory is used to obtain the characteristics. Then, the diaphragm is lumped into an equivalent acoustic mass and acoustic compliance. The former represents stored kinetic energy and the latter models stored potential energy. Similarly, the electromechanical transduction characteristics are determined by the unloaded or "free" voltage-detection characteristics [29]. The piezoelectric electromechanical coupling is lumped into an effective acoustic piezoelectric coefficient. In general, the cavity contains a compressible gas that stores potential energy and is, therefore, modeled as an acoustic compliance.

Lumped Elements Model
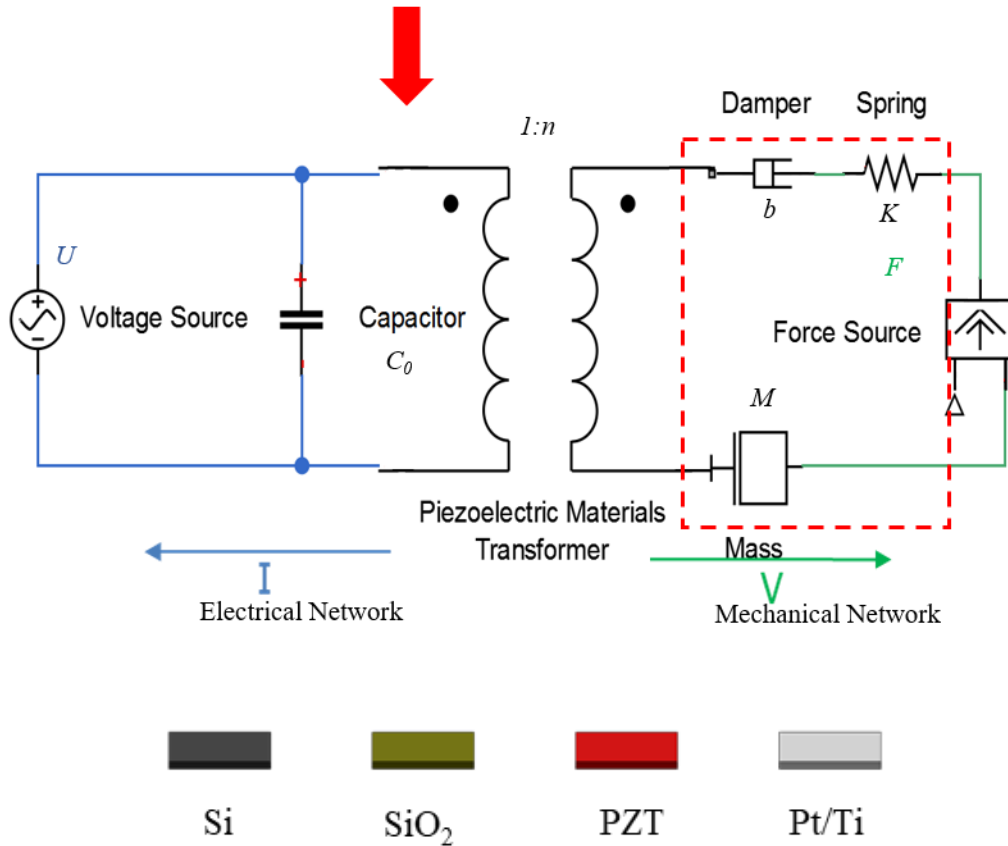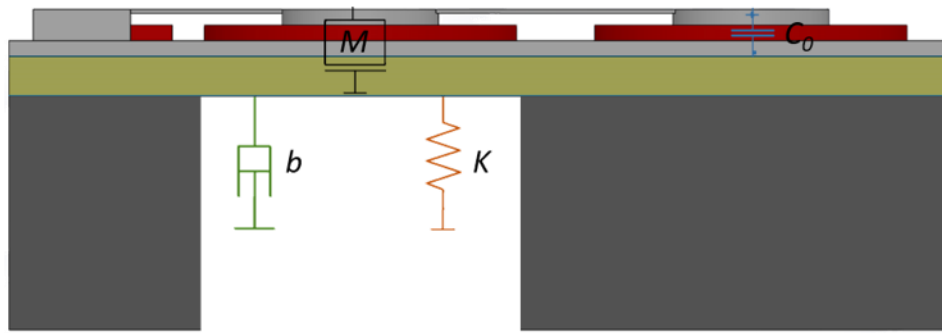
Figure 2.5 Side view of a piezoelectric micromachined acoustic sensor and the transition to its lumped elements model.

    The equivalent circuit representation for the pMUT is shown in Figure 2.5. The compliance, mass, and damping of the piezoelectric diaphragm are normally represented in the mechanical domain. C_0 is the blocked electrical capacitance of the piezoelectric diaphragm driven by an ac voltage. The term blocked is used because it is the impedance seen by the source

when the diaphragm motion is prevented. Although not shown here, a resistor can be introduced in series or in parallel with C_0 to represent the dielectric loss in the PZT.

The lumped element model of pMUT provides a compact analytical model and valuable physical insight into the dependence of the device behavior on geometry and material properties. The physical insight of energy transformation between electrical and mechanical domain provide us an effective way to analyze the radiation effects on piezoelectric MEMS, which can be seen in the following chapters.

2.4.2   Previous Investigation of Radiation Effects on Piezoelectric MEMS

Figure 2.6 provides a summary of the many potential radiation vulnerabilities associated with three different functional locations within a piezoelectric MEMS structure [1]; the complexity of the analysis may also be inferred from the figure. Based on prior work, the ultimate failure of the device likely results from accumulated damage in the piezoelectric active layer, through defect-domain wall interactions, which diminish its electromechanical response.

Previous knowledge of radiation effects on piezoelectric MEMS mainly focuses on the properties of thin film ferroelectric materials. In the 1990s, the radiation response of the ferroelectric properties of PZT were studied extensively. Both [24] and [23] examined the impact of high TIDs using x-ray sources and found very little degradation of the polarization or leakage current up to a total dose of 5 Mrad(Si). In [30], the material was subjected to neutrons and was found to have a 10% reduction in switching charge at a neutron fluence of 10^{15} /cm^2. Despite the intensive ferroelectric property studies, the piezoelectric properties were not examined at that time. More recently, researchers have started to investigate the piezoelectric properties of thin-films of the material. In [31], Pb(Zr$_{0.52}$Ti$_{0.48}$)O$_3$ films were irradiated in the neutron spectrum of a nuclear reactor at a 1 MeV equivalent neutron flux of $(7.17\pm0.04)\times10^{11}$ cm^{-2}s^{-1}. Following exposure, a decrease in reversible and irreversible contributions to extrinsic permittivity were observed. The changes were attributed to the formation of defect dipoles and other charged defects within the material that impede domain wall mobility. In [32], both X-rays and proton irradiation were used to examine thin-film PZT piezoelectric stability. Again, a decrease in the piezoelectric properties was observed and was attributed to point defects generated within the material. Oxygen vacancies are also known to exist in PZT thin films making a similar

mechanism possible. The primary defect formation mechanism is ionizing dose related, not through direct displacement damage. The researchers from Georgia Institute of Technology and Naval Research Laboratory have investigated the effects of gamma radiation on the dielectric and piezoelectric response of $Pb[Zr_{0.52}Ti_{0.48}]O_3$ (PZT) thin films as a function of metallic (Pt) or conductive oxide (IrO_2) top electrodes [33]. All samples showed a general degradation of dielectric, polarization, and electromechanical responses when exposed to 2.5 Mrad(Si) ^{60}Co gamma radiation.
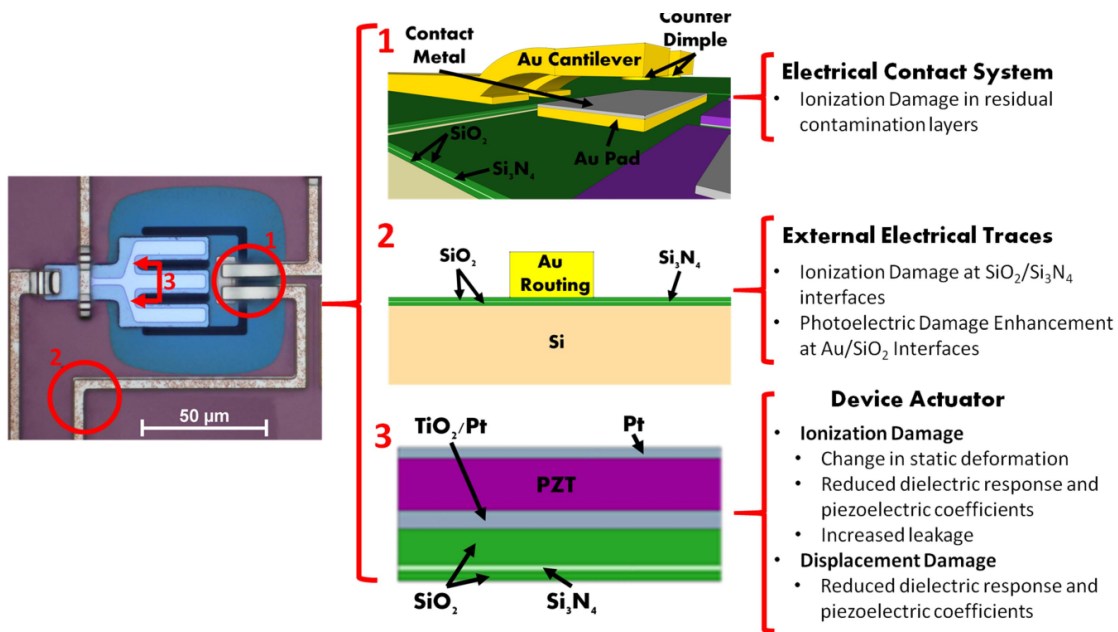
Figure 2.6 Schematic representation of a piezoelectric MEMS mechanical logic architecture and impact of radiation on various functional locations. (Arutt etc. [1])

However, only a small amount of work shows how radiation affects piezoelectric MEMS device performance, including deformation, resonant frequency and quality factor. A bridge is needed between piezoelectric materials variation and MEMS performance in radiation environments.

2.5 Radiation Effects on Electrothermal MEMS

2.5.1 Stress, Strain and Electrothermal Bimorph Actuator

An electrothermal bimorph structure consists of a stack of two layers of thin-film materials with different coefficients of thermal expansion (CTEs). The simplest bimorph actuator is a single cantilevered bimorph beam, shown in Figure 2.7. The cantilevered bimorph beams can be intelligently connected to form more complicated bimorph actuators. But the basic principle of electrothermal bimorph actuation can be drawn from this basic building block. As the thin films in a bimorph undergo internal or external changes, *e.g.*, thermal expansion, phase transformation or other physical effects, the strain generated in each thin film is different if the two thin films are freed of the constraint imposed by each other. This difference in their strain development is referred to as the strain incompatibility or strain mismatch within the bimorph when it is considered as a unity [34]. Thermal bimorph actuation uses intrinsic stress to determine the initial rest position of the object of interest and use Joule-heating induced extrinsic stress to realize the actuation.
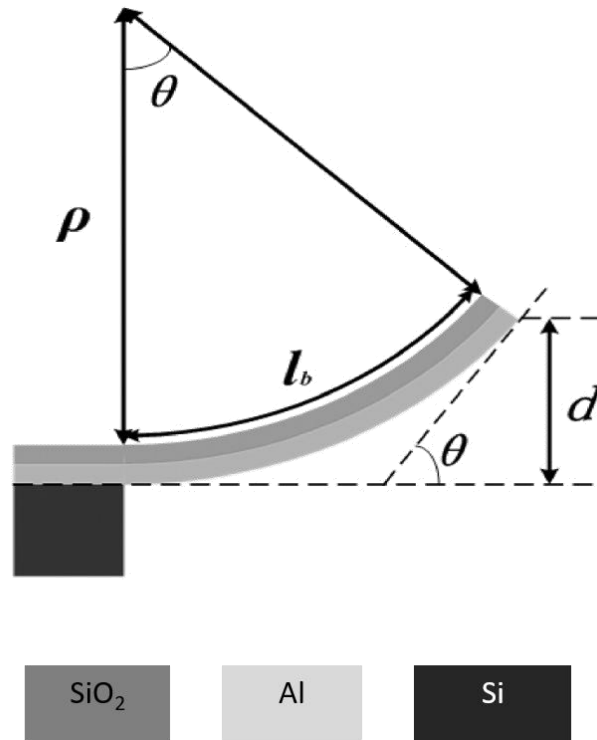
Figure 2.7 Cross sectional view of the curvature.

2.5.2   Previous Investigation of Radiation Effects on Electrothermal MEMS

Two groups of researchers have tested horizontally deflecting electrothermal actuators within a radiation environment. Taylor et al. [35] irradiated the actuator with protons and gamma rays and Johnstone et al. [36] irradiated the device with protons. Taylor et al. used an ion microbeam to irradiate specific sections of the actuator believed to be high tensile stress areas. They explored degradation in operability directly due to dielectric charging, a common consequence of radiation exposure. Their testing revealed that no ion induced degradation occurred. Furthermore, they found no cracking or degradation in deflection in the device because of the irradiation. The researchers pointed out that high fluences or different conditions can result in adverse charge build-up which can lead to system failure as a result of stiction. Johnstone et al. [36] irradiated their devices with 50 MeV protons at total doses ranging from 10^9 to 10^{13} p /cm^2. There were no noticeable changes in the current versus voltage (IV) characteristics before or after irradiation. However, some changes were noted concerning the deflection between the un-irradiated and irradiated devices. This change was attributed to stiction. The researchers were unsure if the stiction was a result of the irradiation or just environmental contamination.
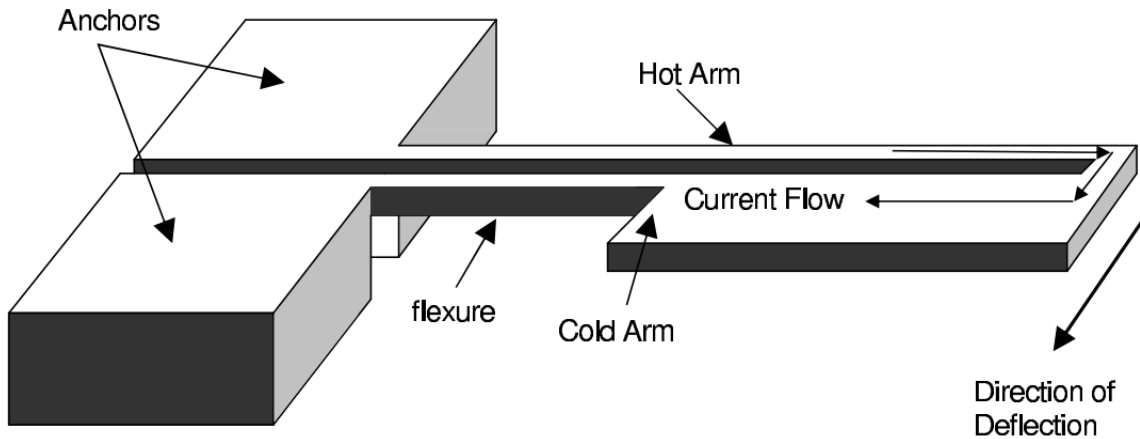
Figure 2.8 Isometric drawing of horizontally deflection electrothermal actuator. (Caffey [37])

Figure 2.8 is an illustration of a horizontally-deflecting electrothermal actuator used for radiation tests by Jared R. Caffey [37]. The electrothermal actuator is typically characterized by the relationship between the amount of tip deflection and applied voltage. The measurement procedures consisted of applying a DC voltage and monitoring the tip deflection using the video capture software. A total of eight die containing electrothermal actuators were irradiated with 50

keV X-rays. The die was irradiated to total ionizing doses of 250, 500, 750 and 1000 krad(Si). The deflection-voltage response for electrothermal actuators irradiated with 50 keV X-rays using the low energy X-Ray source. The plots in Figure 2.9 represent the average measured tip deflection plus and minus the standard error in the measurements. The measured tip deflection for all the irradiated actuators shows a decrease. The change in tip deflection seems to extend to lower voltage levels as the total ionizing dose is increased.

The author also did the "control" experiment on electrothermal actuators not subjected to any radiation. The actuator was cycled through a voltage sweep from 0 to 20 V for approximately 34 minutes. The same procedures used to characterize the actuators before and after irradiation were followed. Figure 2.10 illustrates the measured tip deflection before and after the actuator was broken-in. The amount of tip deflection associated with a given voltage decreases after break-in. This is the same phenomenon noted for the irradiated actuators. Based on this experiment, the author concluded that the radiation has no effects on electrothermal MEMS and all the observed variations are due to device break in.

The actuators were swept with positive voltage for long times. This process is similar to the stress test in the radiation researches. Long time application of an electric field can lead to charge accumulation in dielectric layers of MEMS. The "control" experiment verified that the obvious radiation effects on electrothermal MEMS are closely related to charge accumulation. The "break in" process is the process in which charges move and are trapped in pre-existing defects.
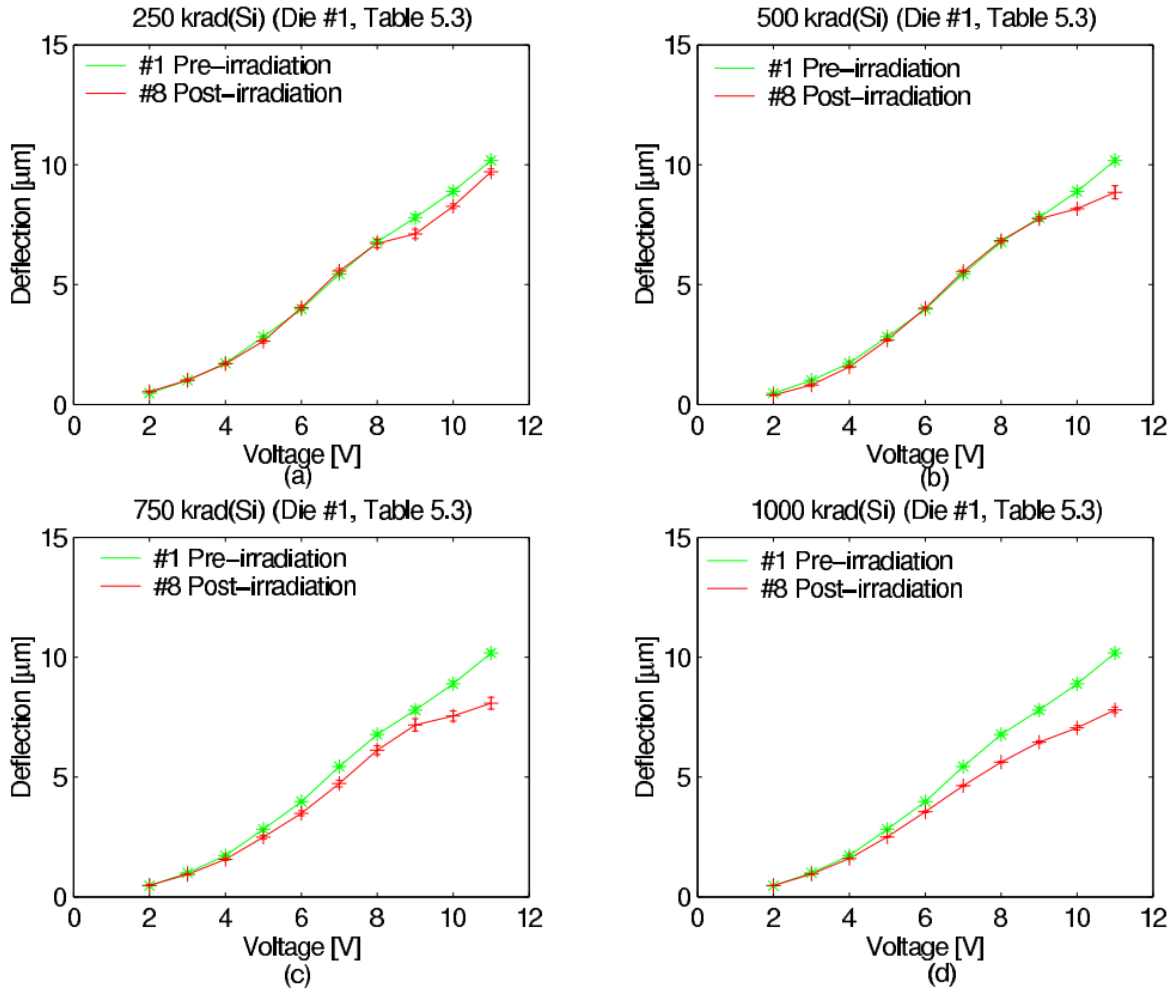
Figure 2.9 Pre- and post-irradiation deflection measurements for 250 µm long electrothermal actuators subjected to total ionizing doses of (a) 250 krad(Si), (b) 500 krad(Si), (c) 750 krad(Si), and (d) 1000 krad(Si) in low energy X-Ray source. (Caffey [37]).

20
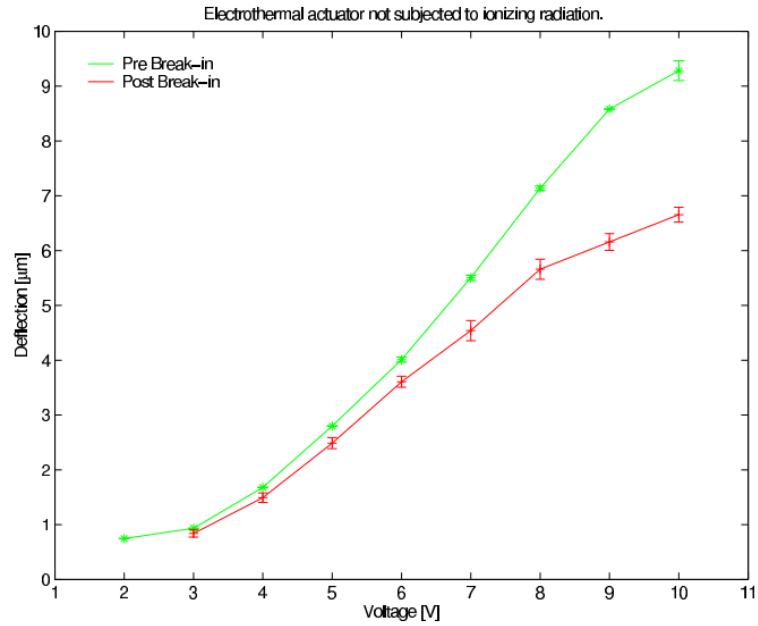
Figure 2.10 Measured tip deflection after 34 mins 0 to 20 V voltage sweeping. (Caffey [37]).

In conclusion, the deflection changes between the un-irradiated and irradiated electrothermal MEMS. This change was attributed to stiction, break in or stress annealing. Recent research shows the deflections are closely related to charge accumulation and radiation may cause the deflection variations.

2.6   Radiation Effects on 2D MEMS

Two-dimensional materials have attracted great research interest in recent years for various potential applications. Specifically, the large surface area to volume ratio of these carbon-based material make them prime candidates for sensing applications in MEMS [38]. The atomic thickness leads to very low volume for interaction with radiation. However, the response of micromechanical properties to radiation damage is virtually unstudied.
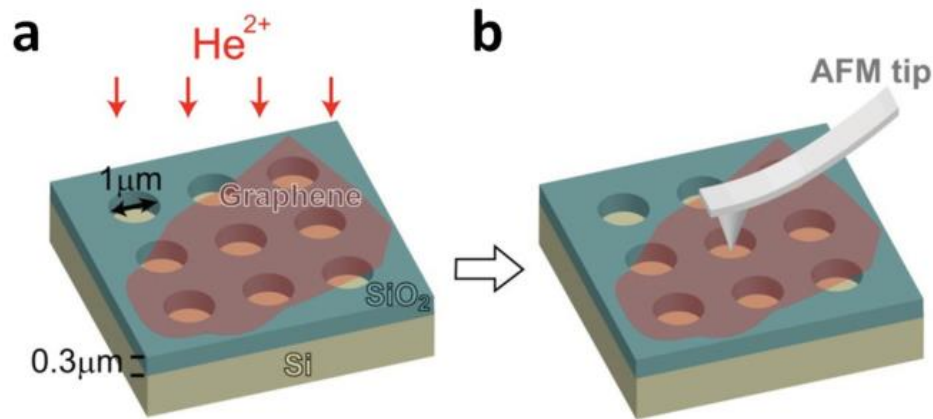
Figure 2.11 Schematic diagram of the (a) the suspended graphene flake and radiation experiments. (b) AFM experiment for measuring Young's modulus. (K. Liu etc. [39]).

Several irradiations on 2D MEMS are done with different kinds of ions. AFM and Raman spectroscopy are normally used for investigating relationships between radiation dose and Young's modulus. Figure 2.11 (a) shows a schematic diagram of a graphene flake transferred onto a porous substrate and irradiated by 3 MeV He^{2+} ions [39]. Their 2D elastic modulus (E_{2D}) is measured by indenting the center of these circular, free-standing graphene membranes with an atomic force microscope (AFM) tip.

Figure 2.12 (c) plots normalized E_{2D} as a function of cumulative irradiation dose. In the low-dose regime, E_{2D} remains nearly a constant, insensitive to the defects. When the dose is higher than 10^{13} ions cm^{-2}, E_{2D} starts to decrease, as the high density of point defects weakens the average atomic bonds in the graphene. In contrast, the measured values of tension fluctuate and do not show a clear trend over the range of irradiation dose, revealing that the irradiation does not loosen the membrane that can result in the modulus softening. However, the E_{2D} curves show a clear dip at the dose of 3×10^{14} ions cm^{-2} because of a residual contamination layer. Under

such high doses, the contamination layer tends to form a continuous film and becomes difficult to clean thoroughly.
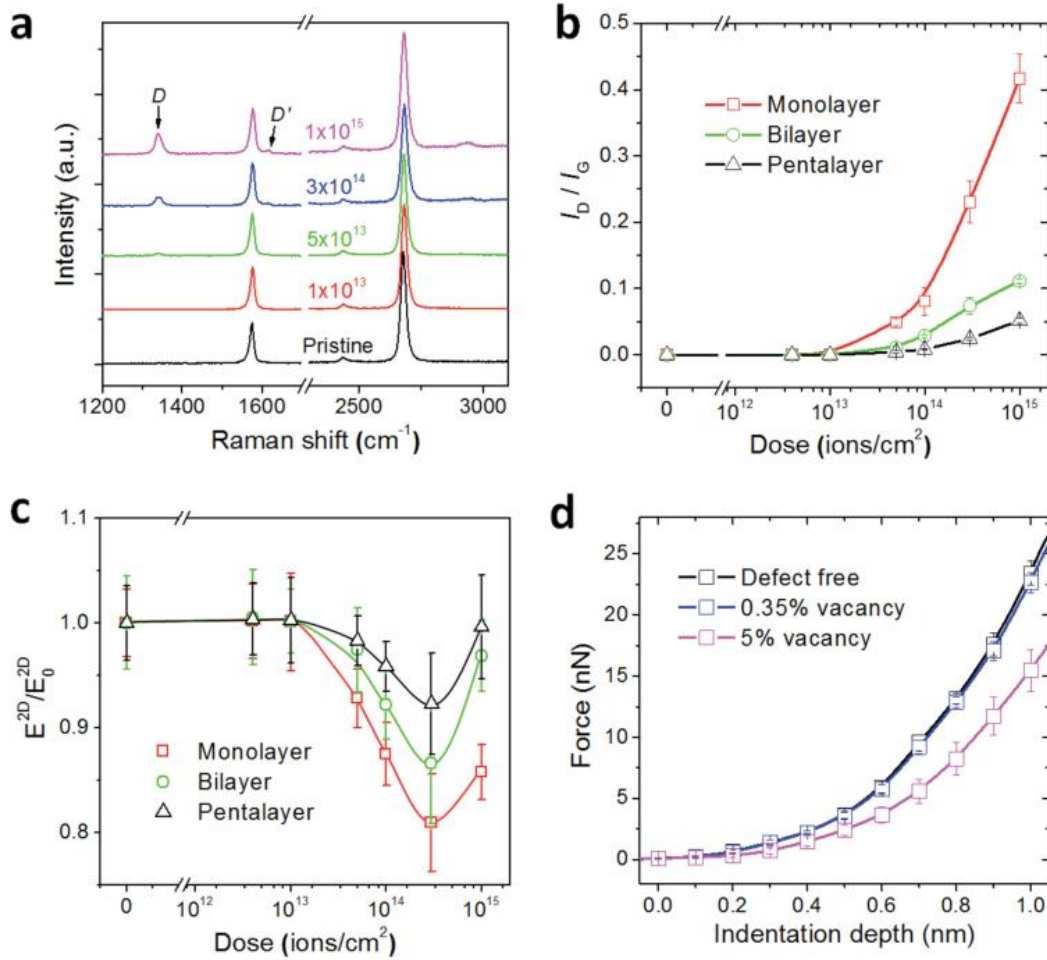
Figure 2.12 (a) Raman spectra of monolayer graphene after various doses of ion irradiation. (b) Intensity ratio of the D and G peaks (I_D/I_G) of the three flakes as a function of irradiation dose. The difference of I_D/I_G for flakes with different number of layers may result from different scaling rules between I_D/I_G and defect density, owing to different band structures. (c) Normalized E_{2D} of the three flakes as a function of irradiation dose. (d) Simulated force curves of indentation processes under different defect densities (K. Liu etc. [39]).

The AFM is good for measuring elastic modulus of 2D materials with high defect density.

It is still unknown how elastic modulus varies at low radiation dose. The relationship between radiation dose and defect density is unknown. An effective method is needed for evaluating defects generated by radiation.

Researchers from Case Western Reserve University have examined 662 keV gamma ray radiation effects from a ^{137}Cs source upon 2D MoS$_2$ nanomechanical resonators [40]. The results show that all the MoS$_2$ resonators exhibit 0.5–2.1% resonance frequency upshifts due to the ionizing gamma ray induced charges and their interactions. The gamma ray radiation generates trapped charges in the device structure across the SiO$_2$ layer and cause electrostatic forces between the charged MoS$_2$ drumhead and the Si substrate, resulting in electrostatic tension and deflection of the MoS$_2$ drumheads, and the resonance frequency upshifts.

More and more new materials are being incorporated into MEMS. To create high frequency (~MHz) resonators, some 2D membranes are utilized in MEMS. How radiation impacts the ultra-thin 2D membranes properties is not clear. In this research, we need to figure out how energetic ions interact with 2D membrane.

Figure 2.13 shows a model for high energy ion bombardments on an ultra-thin target 2D membrane. The number of created defect N_{events} can be expressed as [41]:

$$N_{events} = kN_{incident}nx\sigma \tag{2-5}$$

in which k is a constant, $N_{incident}$ is number of incident particles, σ is the cross section, n is target atoms per unit volume and x is the thickness of the target material.

For Coulomb scattering, the cross section σ can be calculated through:

$$\frac{d\sigma}{d\Omega} = \left(\frac{zZ\alpha}{4E_k}\right)^2 \frac{1}{\sin^4\left(\frac{\theta}{2}\right)} \tag{2-6}$$

in which $d\Omega$ is an element of solid angle, z is the beam particle charge, Z is the target particle charge, ions kinetic energy is E_k and α is Coulomb's constant.
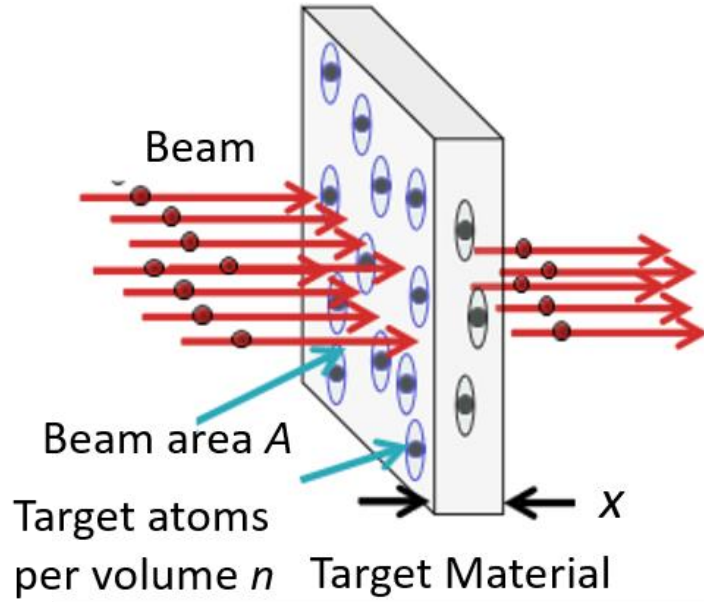
Figure 2.13 Schematic illustration of cross section of target material.

So, the defects generated during the ion bombardment is proportional to the target thickness x. For ultra-thin 2D membranes, the displacement damage is very low. These equations indicate that (1) 2D materials membranes are resistant to the energetic ion bombardment and (2) it is difficult to create high defect density in the 2D membrane experimentally (instrument limitations).

To investigate the defect influence on the 2D membrane mechanical properties experimentally, we need to introduce different defect density into the membrane by irradiation. In the Pelletron system, the parameters we can adjust are beam flux ψ and ion kinetic energy E_k. Normally, the beam fluence increases with ion kinetic energy. Since cross section σ is inversely proportional to the ion kinetic energy and then the beam flux, it is very challenging to create high defect density in 2D membranes by using the Pelletron system. Simulation methods are normally used to analyze defects generated in 2D materials by radiation.

2.7   Summary

The key question for this research is: *How does radiation damage to constituent materials impact the mechanical and electrical basis of operation of MEMS?* Cumulative

damage by non-ionizing energy loss can, in principle, alter the mechanical properties of structures such as cantilevers and 2D membranes, and trapped charge in insulators can impact electrical operating conditions. Presently, the extent to which such effects impact the operation of advanced MEMS is unclear.

There are limited studies of radiation effects on MEMS, and most of them focus on radiation influence on MEMS mechanical or electrical properties. Since MEMS is an electrical/mechanical to mechanical/electrical energy transforming system, any variations in the mechanical parts should lead to corresponding variations in the electrical part of the system and vice versa. A complete investigation on radiation effects on MEMS should include both electrical and mechanical variation caused by radiation.

Table 2.2 Previous Radiation Tests and Main Degradation Mechanisms of MEMS

MEMS Types	Radiation Tests	Typical Devices	Degradation Mechanisms	Test Times
Electrostatic	TID + Proton	Analog ADXL 50	Dielectric Charging; Displacement Damage in Circuits	17
Piezoelectric	TID	Mirrors	Displacement Shift Due to Dielectric Charging	6
Electrothermal	TID + Proton	Bimorph Actuators	No failure	1
Electromagnetic	TID	NASA GSFC	No failure	1
Piezoresistive	TID + Proton	Cantilevers	Charge Trapping; Carrier Concentration Variations	5

There are four main energy transforming mechanisms: electrostatic, piezoelectric, electrothermal and electromagnetic. Most radiation studies are focused on electrostatic MEMS, while fewer studies are conducted on piezoelectric, electrothermal and electromagnetic MEMS (Table 2.2). This is because the electrostatic MEMS are the most mature MEMS, commercialized and widely used in space system. The advances in fabrication process, namely the ability to create nanoscale structures, and the introduction of new materials have made it possible to commercialize many newly developed piezoelectric, electrothermal and electromagnetic MEMS in the very near future. The successful application of these MEMS in

radiation environments requires that reliability issues be thoroughly explored and understood. This research evaluates radiation effects on piezoelectric MEMS and electrothermal MEMS through investigating one typical piezoelectric MEMS (pMUT) and one typical electrothermal MEMS (electrothermal microscanner).

There are a number of radiation experiments on 2DAC, especially energetic ions bombardment on graphene. The elastic constant of graphene changes with radiation dose. But there is no effective way to evaluate the defect density generated during these processes. It can be very challenging to compare radiation results from experiments using different energetic ions. Also, it is difficult to understand the reliability of 2D MEMS in radiation environments without these data. In this research, a Monte Carlo approach is developed for analyzing the defects generated in monolayer graphene during energetic ions irradiation. This approach can be used in other 2DAC with a few modifications.

CHAPTER III

3.   RADIATION EFFECTS ON PIEZOELECTRIC MEMS

3.1   Overview and Objectives

Radiation effects on lead zirconate titanate (PZT) have been reported, but very little is known about piezoelectrically-actuated MEMS performance in radiation environments. The most prevalent piezoelectric MEMS are pMUTs. pMUT-based resonators can be used to generate signals of a precise frequency for electrical circuits, with potential applications in space. In this chapter we summarize a study of radiation effects on pMUTs that was reported in [14].

3.2   Device Structure and Sample Preparation

A PZT-based pMUT array is fabricated using a combination of thin film and bulk micromachining processes on a 4-inch silicon-on-insulator (SOI) wafer with a 1 μm thick buried oxide layer, 50 μm thick Si device layer, and a 400 μm thick Si substrate [42]. First, a 1 μm silicon dioxide layer is thermally grown, followed by a sputtered Pt/Ti (200 nm / 20 nm) conductive layer for the bottom electrodes. Eight layers of $Pb(Zr_{0.53} Ti_{0.47})O_3$ (PZT) are consecutively deposited using a sol-gel process in which a colloidal solution is spun at 3,000 rpm and the resultant film is annealed at 650-700 ℃ by rapid thermal processing (RTP). The film thickness for each sol-gel layer is ~ 120 nm. The PZT material can sense applied force and transfer it to electrical charge (piezoelectric effect) or transfer applied electrical field to strain (inverse piezoelectric effect), which makes it a desirable material for MEMS applications. The top electrode pattern is then formed by lift-off of a sputtered Pt/Ti (150 nm / 7 nm) conductive layer. Backside deep reactive ion etching (DRIE) is used to create resonant cavities in the pMUTs.

A schematic diagram of a circular pMUT array is shown in Figure 3.1. A pMUT with the diaphragms clamped on all edges has been chosen as the enabling microarray element. The acoustic sensor is composed of a $Pt/Ti/PZT/Pt/Ti/SiO_2/Si$ multilayer membrane, which works in a flexure mode to sense acoustic energy. Three types of 2×2 pMUT arrays with different shapes have been used for the radiation tests. The parameters of the test samples are listed in Table 3.1.

Initial resonant frequencies and quality factors differed by less than ± 5%. Data shown in this work were selected as representative from multiple samples for each experimental condition.
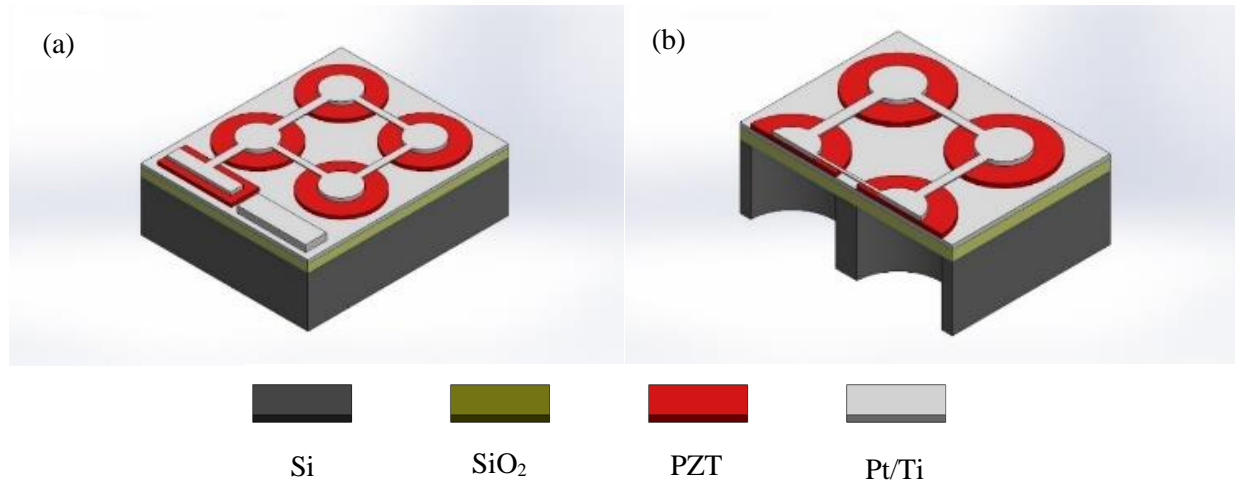
Figure 3.1 3D (a) and cross-sectional view (b) of the pMUT array.

Table 3.1 The pMUT array samples for radiation.

Samples	Shapes	Size (µm)
A	Square	L=360
B	Rectangle	W×L=260×360
C	Circular	R=180

3.3 Piezoelectric MEMS Lumped Model

The piezoelectric MEMS electro-mechanical lumped model shown in Figure 3.2(a) consists of two parallel networks: a mechanical network and an electrical network [43]. The equivalent capacitor, C_0, in the electrical network represents the parallel plate capacitor formed by the metal electrodes and the sandwiched PZT membrane. In the mechanical domain, the

piezoelectric MEMS can be treated as a rigid body and all interactions on the rigid body can be represented using a mass-spring-damper model.
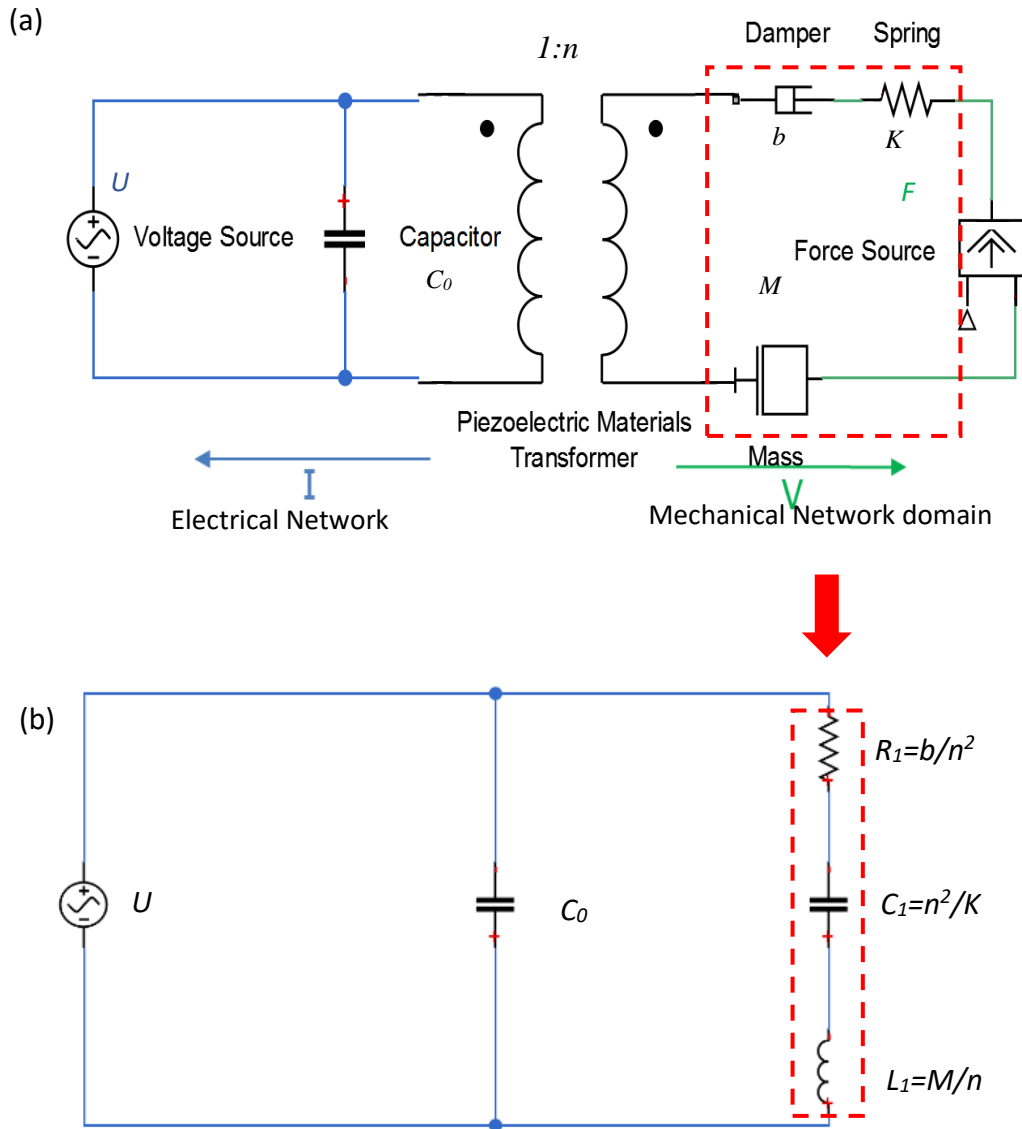
Figure 3.2 Piezoelectric MEMS lumped parameter model.

By considering the velocity and the exciting force as the analogs of the electric current and the electric potential, respectively, these mechanical lumped elements can be expressed as a capacitor, an inductor, and a resistor. The effective mass, M, is represented by an inductor, the spring with spring constant K is represented as a capacitor, and the damper with damping

coefficient b is represented by a resistor. Piezoelectric materials, such as PZT, can transfer energy between the electrical and mechanical domains. These transfers can be modeled as an ideal transformer with a factor n that can transform the damper, spring, and mass constants from the mechanical regime to the electrical analogs R_1, L_1, and C_1 in the equivalent electrical-mechanical circuit shown in Figure 3.2(b). The impedance of the electrical-mechanical circuit in Figure 3.2 is:

$$Z = \frac{j\omega C_1 R_1 - \omega^2 C_1 L_1 + 1}{j\omega C_0 + j\omega C_1 - j\omega^3 C_0 C_1 L_1 - \omega^2 C_0 C_1 R_1}$$

(3-1)

Device characterization was performed in air with an Agilent 4284A precision LCR meter. An idealized impedance curve is shown in Figure 3.3. Curve fitting is used to derive the corresponding electrical parameters C_0, R_1, L_1, and C_1 from the impedance curve. After that, these "electrical components" R_1, L_1, and C_1 are transformed back to the mechanical domain to obtain the mechanical properties of the piezoelectric MEMS, as described in Section 3.4.
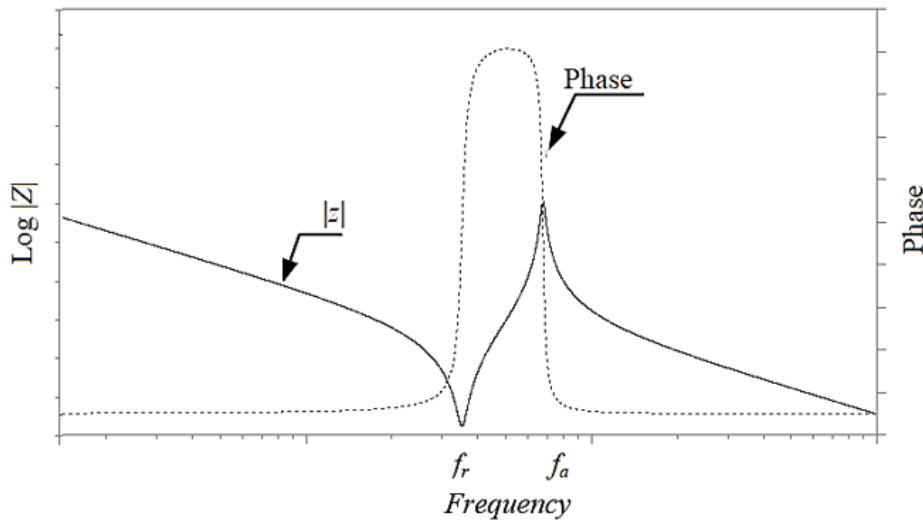
Figure 3.3 Idealized impedance vs. frequency curve of piezoelectric MEMS.

3.4   X Ray Irradiation Experiments

pMUTs were irradiated with a 10 keV X-ray system at biases of -1 V to 1 V to doses up to 3 Mrad(SiO_2). The dose rate was 31.5 krad(SiO_2)/min. All impedance measurements were performed in-situ without any applied bias. The response of more than 20 pMUTs were

evaluated; representative results are shown. Figure 3.4 shows a typical set of impedance vs. frequency curves under x-ray irradiation with 1V DC bias voltage applied to sample B (the rectangular device). The five different color curves represent the impedance responses of sample B at different doses. The resonant frequency increases by up to 5% with increasing dose. Because MEMS resonator output frequency stability requirements are often near 100 ppm (0.01%), see [44] for example, these relatively large shifts can negatively affect system performance.
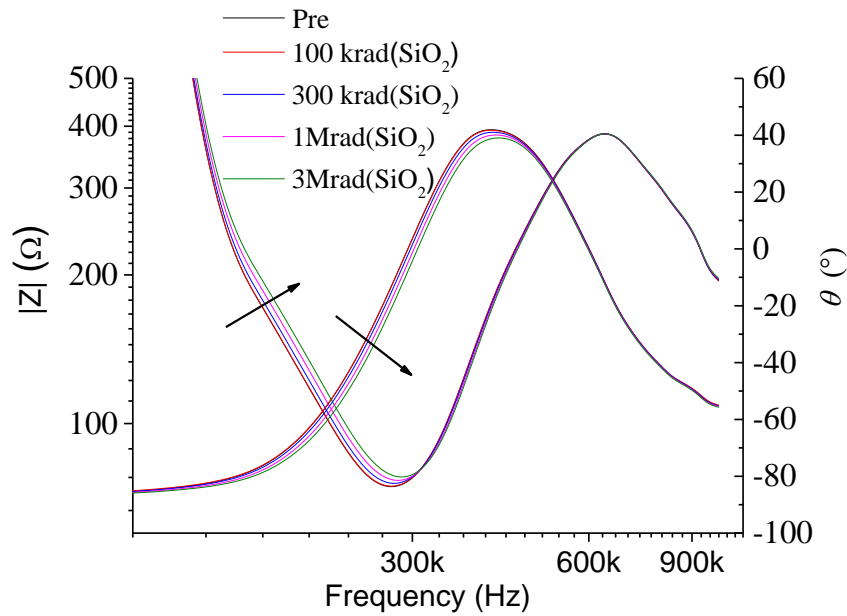
Figure 3.4 Impedance frequency response under x-ray radiation with 1 V bias for sample B.

Curve fitting was used to derive the corresponding electrical parameters C_0, R_1, L_1, and C_1 from each curve. The electrical inductor L_1 and capacitor C_1 are transferred back to the mechanical mass M and spring constant K. n is the turns ration of the transformer, which represents the coupling of electric and mechanic domain in piezoelectric materials. Then the mechanical resonant frequency f_0 can be derived from:

$$f_0 = \frac{1}{2\pi} \cdot \frac{1}{\sqrt{L_1 C_1}} = \frac{1}{2\pi} \cdot \frac{1}{\sqrt{\frac{M}{n^2} \cdot \frac{n^2}{K}}} = \frac{1}{2\pi} \cdot \sqrt{\frac{K}{M}} \tag{3-2}$$

The mechanical resonant frequency is equal to the electrical resonant frequency of the series

LRC circuit. The resonant frequency and quality factor together determine the characteristic MEMS frequency response. The mechanical quality factor Q is defined as:

$$Q = \frac{1}{R_1}\sqrt{\frac{L_1}{C_1}} = \left(\frac{b}{n^2}\right)^{-1} \cdot \sqrt{\frac{M/n^2}{n^2/K}} = \frac{\sqrt{MK}}{b} \qquad (3\text{-}3)$$

The corresponding frequency resolution, and thus the system's sensitivity and stability, are directly linked to Q. A decrease in quality factor can degrade system sensitivity. On the other hand, an excessive quality factor can introduce unwanted noise and signal overshoot, resulting in instability [45].

3.5   Experimental Results and Discussion

Figure 3.5 summarizes pMUT array resonant frequency shifts and corresponding changes in quality factor with total ionizing dose for different biases. The resonant frequency increases with increasing dose for zero or positive bias and decreases for negative bias. Reasons for these shifts are now discussed.

Defects and charge trapping near the electrode regions have direct impacts on PZT thin-film properties, such as coercive voltage, polarity switching and domain morphology [46], [47], [48], [49], [50], [51]. Previous work shows that a large concentration of defects exists in a typical as-processed PZT film, usually associated with acceptor oxygen vacancy and oxygen vacancy complexes [24], as illustrated in Figure 3.6. X-rays generate electrons and holes that can become trapped in pre-existing defects near the PZT/electrode interfaces, with both electron and hole trapping commonly observed [46], [47], [48], [49], [50]. These trapped charges change the strain and stress in the PZT membrane due to the reverse piezoelectric effect, and therefore shift the resonant frequency.

Since defects in these kinds of MEMS devices are mainly distributed on the surface [46], [47], [48], [49], [50], [51], most radiation-induced electrons or holes are trapped near the electrodes. Hence, we model the trapped charges as a thin sheet near the PZT surface. The surface charge density can be evaluated from the static capacitance of the device C_0. Trapped charges cause vertical strain in the pMUT due to the reverse piezoelectric effect.

33
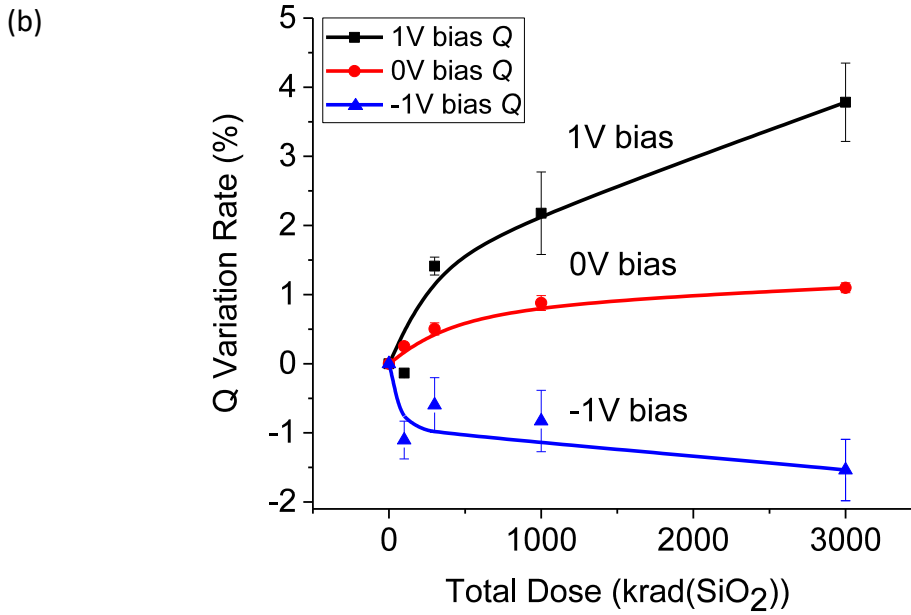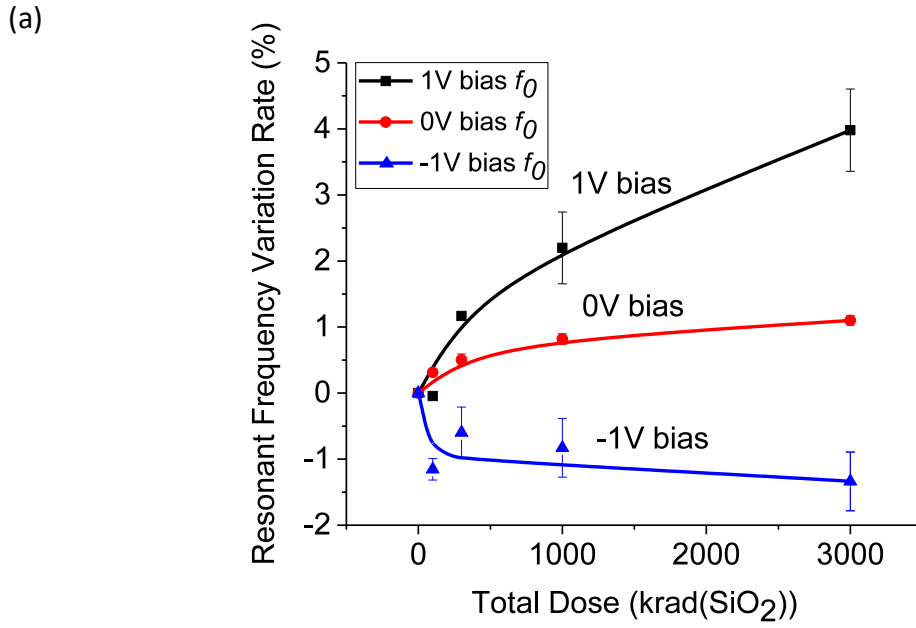
Figure 3.5 (a) Resonant frequency f_0 and (b) quality factor Q for x ray irradiation. Three devices were tested in each bias condition; error bars represent the standard deviation of these test results.

The static capacitance after irradiation C_0^{rad} can be calculated from:

$$C_0^{rad} = \varepsilon \frac{S}{d_0(1+d_{33}E_3)} \qquad (3\text{-}4)$$

Here d_0 is the thickness of the PZT, ε is the permittivity, S is the area of the PZT membrane, d_{33} is the strain coefficient of PZT, and E_3 is the equivalent radiation-induced electric field between the electrodes. Hence:

$$\frac{C_0}{C_0^{rad}} = 1 + d_{33}E_3 = 1 + d_{33}\frac{\sigma S}{d_0 \cdot C_0} \tag{3-5}$$

The equivalent radiation-induced surface charge density, σ, after irradiation can be derived from the change in measured static capacitance via:

$$\sigma = \frac{C_0}{C_0^{rad}} \cdot \frac{d_0\left(C_0 - C_0^{rad}\right)}{d_{33}\cdot S} \tag{3-6}$$

If, for simplicity, we assume that one dominant type of charge is trapped in these pMUTs, the positive value of σ observed for positive bias irradiation likely reflects hole trapping at the lower interface or electron trapping at the upper interface, which reinforces the polarization field, while the negative value of σ observed for negative bias irradiation likely reflects hole trapping at the upper interface or electron trapping at the lower interface, which opposes the polarization field [51].

We note that for positive bias irradiation in Figure 3.5 there is an initial negative shift in device resonant frequency that is small relative to the observed radiation-induced shifts at higher doses, but larger than experimental error and part-to-part variation. This initial negative shift may result from the radiation-induced neutralization [52] of a small amount of remanent charge in these devices. In this regard, PZT has been shown to have both shallow hole traps and deep electron traps that can be activated during processing and/or pre-irradiation testing [46], [47], [48], [49]. Thus, it is quite possible that the initial negative shift under +1 V irradiation may result from the passivation of this small amount of remanent charge by the capture of radiation-induced carriers [52]. This is followed by a positive shift caused by the buildup of radiation-induced trapped charge at higher doses. For -1 V irradiation, each of these effects leads to a negative shift. From these results, it is clear that (1) biased irradiation leads to both positive and negative shifts in resonant frequency in these devices, depending on applied bias during the irradiation, and (2) that, at higher doses, the radiation-induced shifts are much larger than the potential effects of remanent trapped charge in these pMUT devices.

Finally, we note that the resonant frequency variation of a piezoelectric resonator is

proportional to the vertical electrical field, and can be expressed as [53]:

$$f_0 = f_0(0)\left[1 + \left(\frac{d_{33}}{2} - \frac{d_{311}}{2S_{11}^E}\right)E_3\right]$$

(3-7)

Here $f_0(0)$ is the resonant frequency at 0 V, S_{11}^E is the elastic compliance under constant electric field, d_{311} is the nonlinear piezoelectric coefficient, and $E_3 = \sigma/\varepsilon$ is the vertical electrical field. Hence, the resonant frequency is related to σ via:

$$\Delta f_0 = f_0 - f_0(0) = \left(\frac{d_{33}}{2} - \frac{d_{311}}{2S_{11}^E}\right) \cdot \frac{f_0(0)}{\varepsilon} \cdot \sigma$$

(3-8)

This shows that changes in resonant frequency are linear with changes in radiation-induced charge density. Figure 3.7 summarizes the values of σ inferred for the devices of Figure 3.5. The bandwidth is defined as f_0/Q. Because both f_0 and Q change linearly with σ, radiation induced charge trapping does not significantly affect the bandwidth.
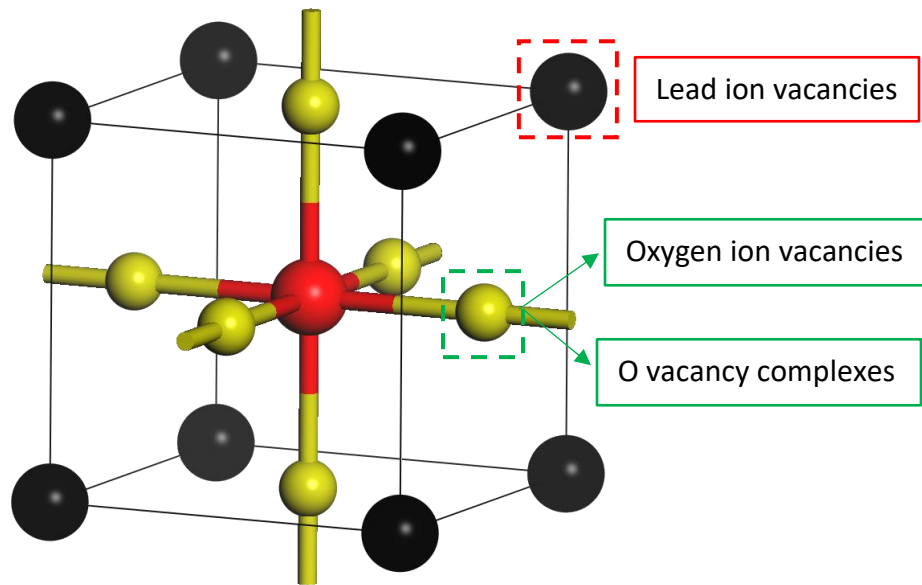
Figure 3.6 Defects in sol-gel based PZT material.

36
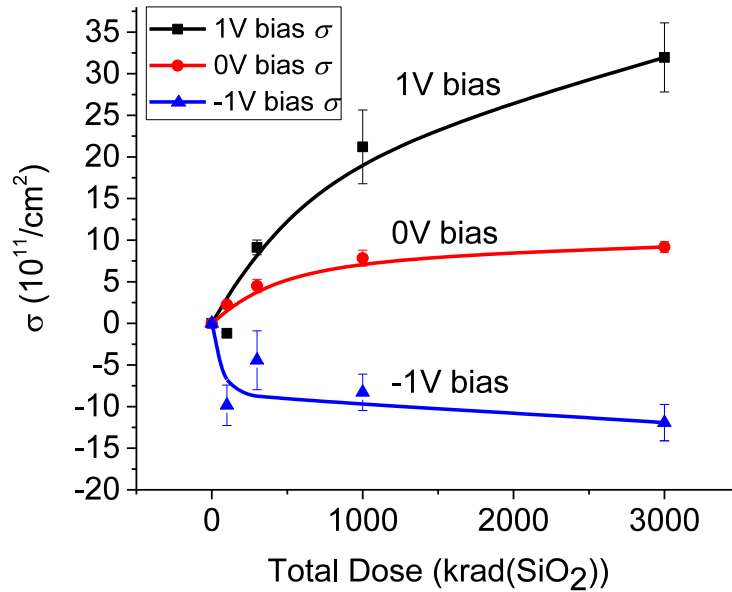
Figure 3.7 Surface charge density σ under x ray irradiation.
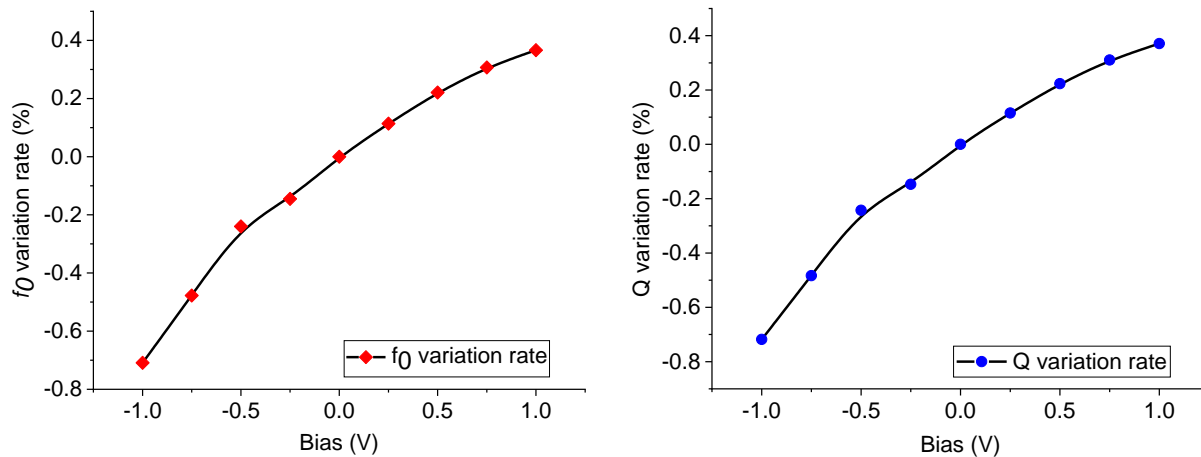
Figure 3.8 (a) Resonant frequency f0 and (b) quality factor Q under different DC biases.

To further investigate the effects of charge trapping and applied voltage on piezoelectric MEMS, DC biases ranging from -1 V to 1 V were applied on the top electrodes of unirradiated pMUT capacitors. An Agilent 4284A precision LCR meter was used to apply biases and measure the impedance of the pMUT. Curve fitting is again used to derive corresponding electrical

37

parameters, and mechanical properties are calculated with the same approach as that illustrated above. Figure 3.8 shows the resulting resonant frequency and quality factor variation as a function of applied DC bias.

In terms of voltage, according to Eq. (3-7), the resonant frequency can be expressed as:

$$f_0 = f_0(0)\left[1 + \left(\frac{d_{33}}{2} - \frac{d_{311}}{2S_{11}^E}\right) \cdot \frac{V}{d_0 + d_{33}V}\right] \tag{3-11}$$

The DC bias test results of Fig. 8 are consistent with the x ray radiation results, which confirm the strong effect of radiation induced charge on resonant frequency and quality factor.

Figure 3.9 shows a COMSOL simulation model of the pMUT used in the radiation tests. Different surface charge densities ranging from 0 to 5×10^{11}/cm^2 were simulated on the top surface of the PZT layer. The first order resonant frequency was calculated. The mesh size in the simulation should be fine enough to obtain the small size deviations. The resulting close agreement of the COMSOL simulations and the 0 V bias test results is shown in Figure 3.10, confirming the strong effect of accumulated charge on resonant frequency.
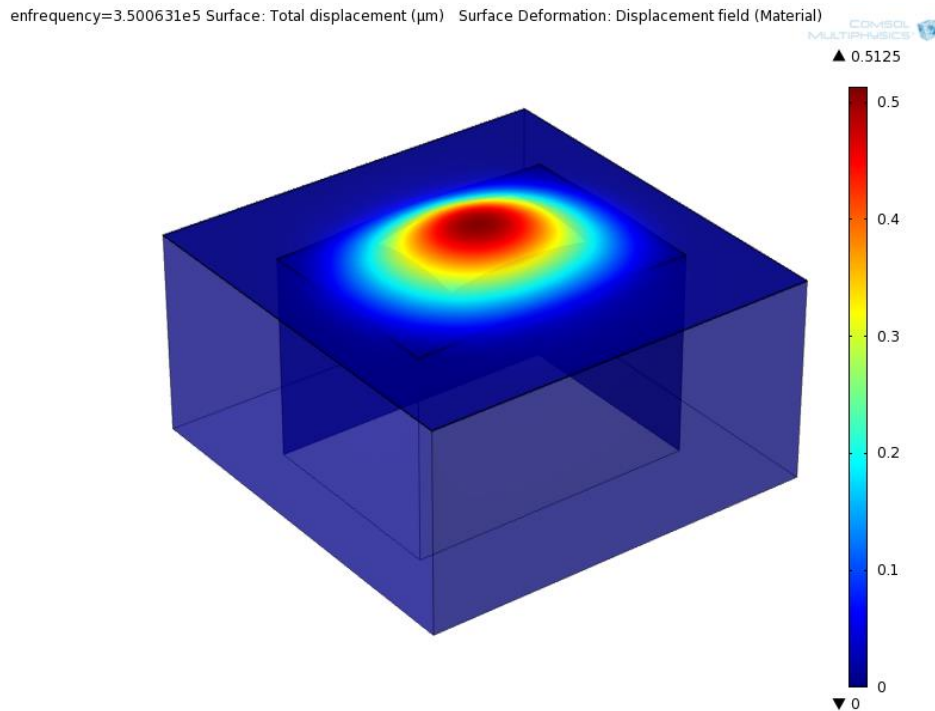
Figure 3.9 COMSOL model of pMUT with a simulated charge density of 5 x 10^{11}/ cm^2.

The above results clearly demonstrate that piezoelectric materials with low defect density are needed for applications in harsh radiation environments. Recently, it was shown that bulk single crystal piezoelectric AlN is able to survive for extended periods in reactor cores [54]. Hence, in future work, it would be useful to compare the responses of these PZT devices with those of AlN and other types of piezoelectric materials.
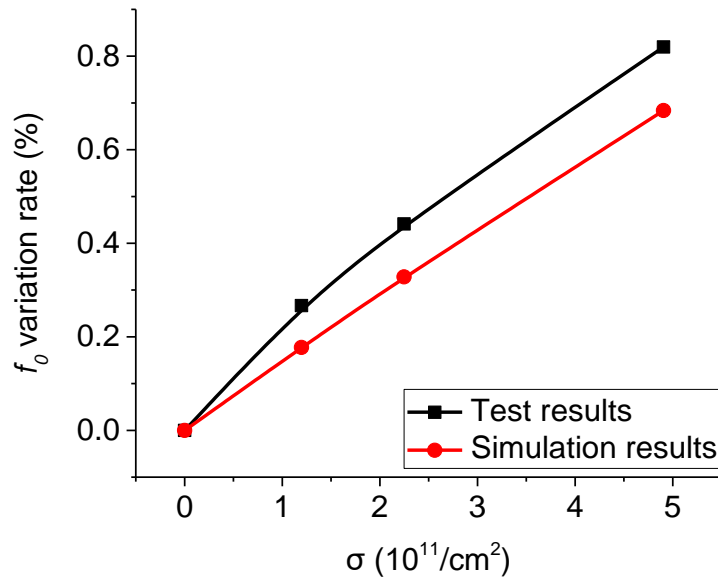
Figure 3.10 Resonant frequency vs surface charge density. The squares are irradiations under 0 V bias. The circles are COMSOL simulations. The curves are aids to the eye.

3.5   Conclusions

The pMUT resonant frequency and quality factor response to 10 keV X-ray irradiation are investigated in this chapter. The impedances of pMUTs under irradiation were measured and corresponding equivalent electrical parameters were derived though curve fitting. The mechanical resonant frequency and quality factor of pMUTs were derived from equivalent LRC circuits. The resonant frequency and quality factor change with the irradiation dose. The worst case for TID effects in these pMUTs is positive bias during the radiation. The bias-dependent transport and trapping of radiation-induced charge near the electrodes and the resulting changes in stress and strain of the PZT are responsible for these changes. These results illustrate the

strong dependence of piezoelectric MEMS resonant frequency and quality factor on trapped charge buildup, and hence the defect density of piezoelectric materials. In summary, radiation effects on piezoelectric MEMS must be considered for applications that need high resolution and long-term reliability.

CHAPTER IV

4. RADIATION EFFECTS ON ELETROTHERMAL MEMS

4.1   Overview and Objectives

Total-ionizing-dose (TID) effects on Al/SiO$_2$ bimorph electrothermal microscanners are investigated using 10-keV X-rays and 14.3 MeV oxygen ions under different bias conditions. The corresponding changes in mechanical displacement are measured using an optical microscope. Applied DC voltage and/or radiation-induced charging change the stress and strain in the materials, resulting in mirror plate shifts and thermal resistance variation, due to the interplay between radiation-induced charging and bias-induced heating effects. The radiation response of the electrothermal microscanners depends strongly on applied DC voltage, as well as bias during irradiation. The results in this chapter were presented at the 2017 IEEE Nuclear and Space Radiation Effects Conference and published in the *IEEE Trans. Nucl. Sci.* [55].

4.2   Device Structure and Samples Preparing

Electrothermally actuated MEMS have the potential to simultaneously achieve large force and high displacements, which makes them potentially well suited for space actuation applications, such as electrothermal valves used in MEMS thrusters for nano- and pico-satellites [56] and microswitches [57]. Al/SiO$_2$ bimorph actuators are widely used in electrothermal MEMS because of their large differences in coefficients of thermal expansion, desirable mechanical properties, and ease of fabrication [58]. Optical MEMS have extensive application prospects in space. For example, micromirrors are required for inter-satellite and Earth/satellite laser communications and micro-electromechanical louvers for satellite thermal control [59], [60]. Microlenses are used to cool the focus panel of visible/infrared imager radiometer suites [61]. Microscanners are used as drivers for micromirror/microlens elements.

An electrothermal bimorph structure consists of a stack of two layers of thin-film materials with different coefficients of thermal expansion (CTEs). When this structure is heated, the different thermal expansion of the two materials induces mismatch strain, which leads to vertical displacement [62]. A SEM image of an electrothermal microscanner is shown in Figure 4.1(b). The square microlens holder is supported by four groups of electrothermal bimorph

actuators symmetrically located on the four sides of the center holder. Each group consists of two S-shaped inverted-series-connected (ISC) bimorph actuators, as shown in Figure 4.1(a). The ISC bimorph actuator consists of four S-shape bimorph sections attached end-to-end such that both S-shape sections point in opposite directions, as shown in Figure 4.1(c). An individual S-shape section consists of two single bimorph sections attached in series, where one section has a high-CTE metal (Al) top layer and a low-CTE dielectric (SiO$_2$) bottom layer, and the adjacent section has opposite layer composition. This alternating construction of the material layers and the double S-shape construction allows each adjacent single bimorph section to have equal and opposite curvature upon actuation so that the entire beam deforms with no rotation angle and displaces purely in one direction at the tip.

The design depicted in Figure 4.1 overcomes both holder-plate shift and rotation-axis shift problems that exist in single cantilever actuators [63]. The double ISC actuator structure amplifies the small strain mismatch between bimorph materials, leading to large lateral shifts of the mirror plate. The layer structure parameters of each S-shaped bimorph series are shown in Figure 4.1(d). A Pt resistor is embedded between the bottom SiO$_2$ and Al layer and shares the same path as the Al beam for thermal uniformity. Each pair of ISC actuators shares a single Pt resistor.

The device is fabricated by a combined surface and bulk micromachining technology in the nanoscale research facility at the University of Florida [62]. This microfabrication process starts from a bare SOI wafer. First, a 1.2 μm thick layer of PECVD SiO$_2$ (labeled as SiO$_2$-B) is deposited and patterned to form the bimorphs that require SiO$_2$ as the bottom layer. For better step coverage, the patterning of this SiO$_2$ layer uses wet etching to form an acceptable slope of the step. Then, a thin (~ 0.1 μm) protective layer of SiO$_2$ is deposited, followed by a 0.25 μm thick Cr–Pt–Cr sputtering and liftoff. Another thin insulating SiO$_2$ layer (~ 0.1 µm, labeled as SiO$_2$-C in Figure 4.1(d)) is deposited and patterned to prevent electrical shorts between Al and Pt on the bimorph beams, exposing pad and wiring areas for wire bonding purposes and reducing parasitic resistance. After this, a 1.1 µm aluminum liftoff is performed to define the bimorphs and the mirror plate. Next, a second SiO$_2$ layer of 1.2 μm (labeled as SiO$_2$-A in Figure 4.1 (d)) is deposited and patterned to form the bimorphs that require SiO$_2$ to be the top layer. A back-side silicon etch is then performed, followed by the buried SiO$_2$ etching step with RIE to form the

42

cavity under the mirror plate and actuators, leaving a controllable thickness ($\sim 40\,\mu m$) of silicon to support the mirror plate. Finally, a front side silicon etch-through, followed by an isotropic undercut, is performed to release the entire microstructure. The presence of the three SiO_2 layers makes the structure of Figure 4.1 potentially sensitive to ionizing radiation exposure, owing to the high probability of radiation-induced charging effects due to charge trapping in insulating layers, as well as potential changes in the sensitivity of the structure to DC voltage-induced
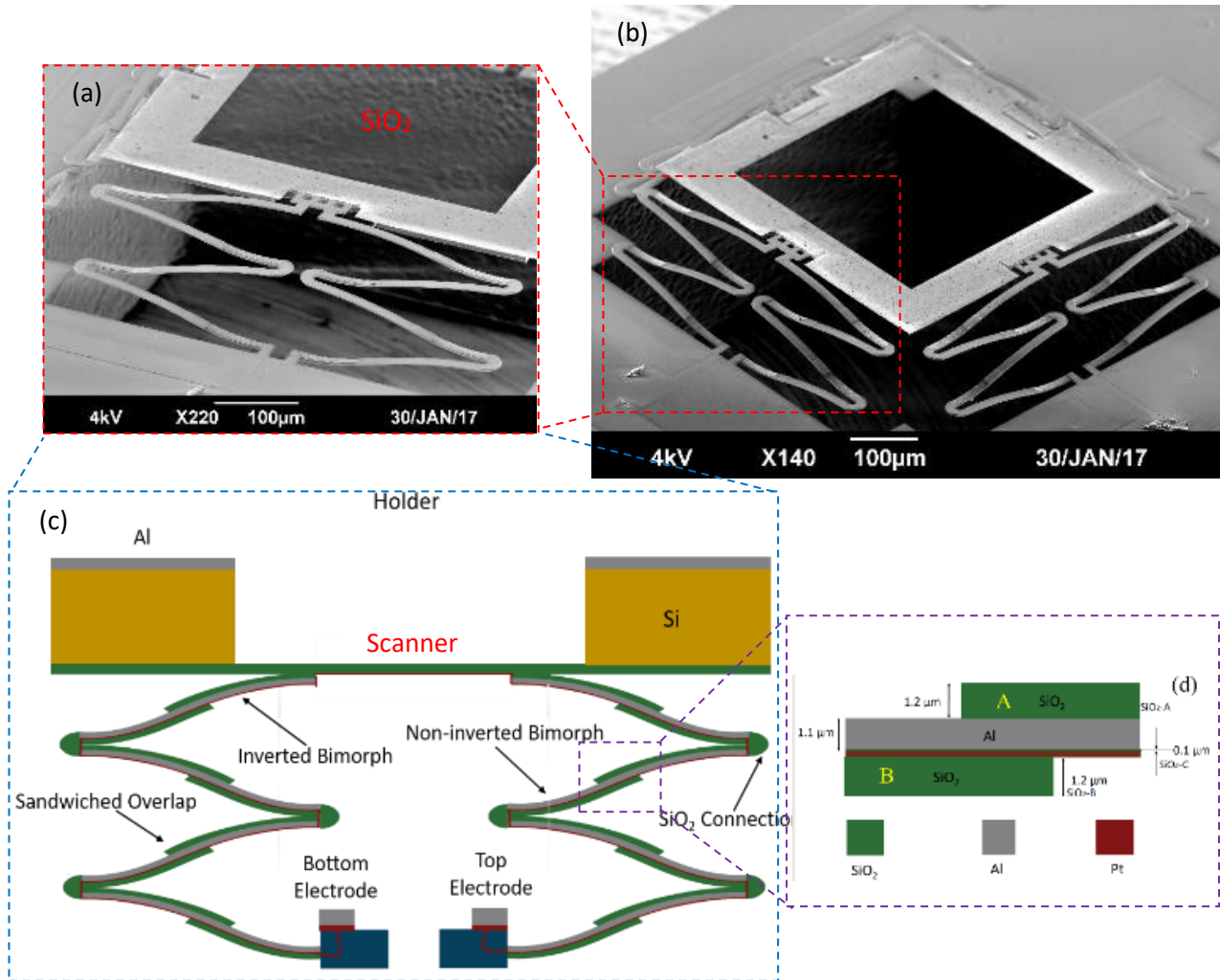
heating, leading to significant strain as a result of differential rates of thermal expansion.

Figure 4.1 (a) Bimorph series and connections. (b) Side View. (c) ISC actuators. (d) Layer structures of a microscanner.

4.3   Bias Stress and X ray Irradiation

The microscanner can function in piston-mode and rotation-mode actuation. Piston-mode actuation is achieved by applying equal voltage to all resistors. In piston-mode actuation all resistors create an equal temperature change, which results in equal displacement of all actuators, and pure downward displacement of the scanner plate. Static rotation measurements were taken by applying similar DC voltages to all four actuators and, at the same time, superimposing two differentially varying voltages to one opposing actuator pair. Mechanical piston motion characterization was performed in air with a Signatone CM210 microscope with 1 μm resolution in the z-direction.

Test voltages of 1 to 6 V_{DC} were applied to all actuators to evaluate piston movements. *I-V* curves were measured using an HP 4156 semiconductor parameter analyzer. After each test voltage, 15 s was allowed for actuators to reach thermal balance. Then the image was refocused, and the z-position reading of the scanner plate was recorded. The anchor plane was set as the zero plane. The image was refocused at each voltage and the corresponding z-position reading of the scanner plate was recorded. The stressing and measurement process takes ~ 60 s for each data point. Data points for multiple locations on the scanner plate were taken to verify piston motion, and average results are shown below. Typical variations in measurements are less than ± 10%. Figure 4.2 shows COMSOL finite element simulations of resistance temperature increases during a typical DC biasing sequence [64]. The maximum increase during testing is 230 K, which occurs when actuators are biased at 6 V.

To characterize the radiation response, electrothermal microscanners were irradiated at room temperature with 10-keV x-rays or 14.3 MeV oxygen ions with top electrode bias of 0 or +1 V and other terminals grounded at a dose rate of 31.5 krad(SiO_2)/min. We measured z-position vs. voltage at each dose using a procedure similar to that illustrated above. The displacement of the plane of the scanner plate at each test voltage is derived from the z-position curve. More than three microscanners were evaluated for each bias condition, with similar results. Typical results are shown below.
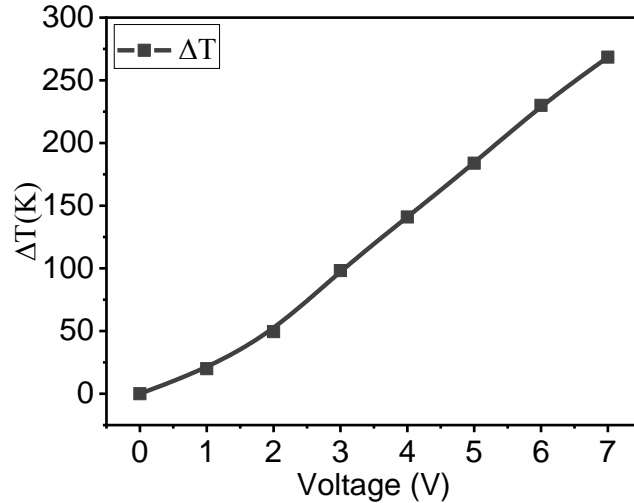
Figure 4.2 Micro-scanner resistor temperature increases as a function of applied DC voltage as determined by COMSOL simulation.

4.4   X Ray and Bias Test Results

To evaluate the stability of the structure, first all Pt resistors were grounded, and the z-position and resistance were monitored every two hours. No variations were found after 24 h of room temperature storage. The effects of repeated voltage cycling were then evaluated. Figure 4.3 shows the z-position and Pt resistance vs. test voltage before and after 2 hours of continuous *I-V* sweeping from 0 V to 6 V at a rate of ~ 4.5 V/s. As the scanner plate moves downward due to heating-induced strain and the resulting material-dependent differences in rates of thermal expansion during each cycle, the length of the Pt resistor increases, and the cross-sectional area decreases, leading to an increase of the resistance. These results show that cyclical, ramped voltage sweeps do not cause permanent changes in device response.
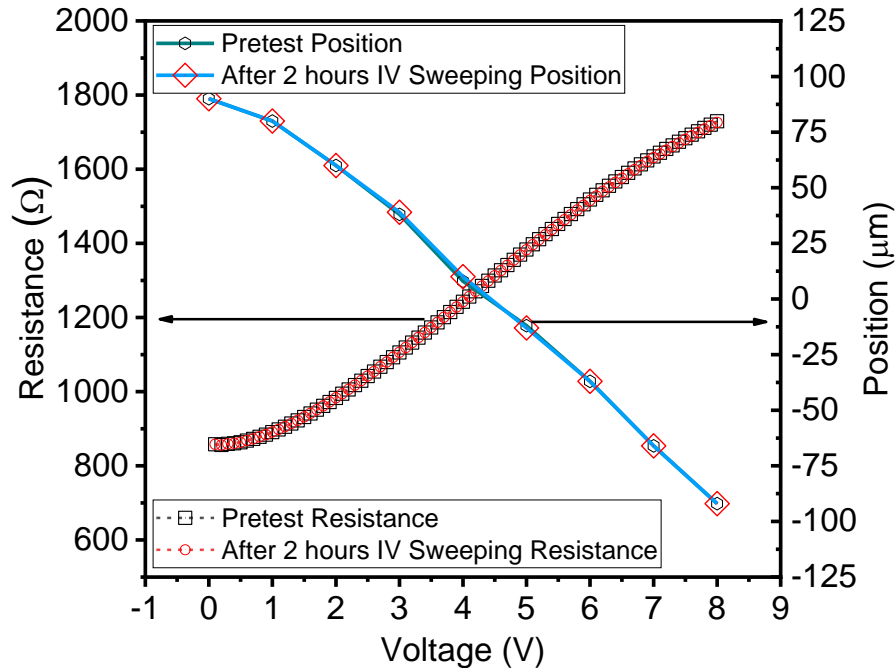
Figure 4.3 Characterization of micro-scanners after cycling 2025 times: (left y axis) displacement position as a function of sweep voltage, and (right y axis) resistance as function of sweep voltage. The I-V sweep rate is ~ 4.5 V/s.

Figure 4.4 shows the z-position and resistance variation after DC bias of 7 V, 1 V, or -1 V was applied to all top electrodes (connected to Pt resistors) for bias times of 5 to 900 minutes. The maximum temperature increases during stress is ~ 275 K for the long-term 7 V stress (Figure 4.2). These measurements were performed after removal of DC bias, with 0 V applied to the top electrodes, after the device was allowed to equilibrate to room temperature. The resistance increases by ~ 15% during the 900 minutes stressing period, and the z-position drops by ~ 25%. In contrast to the results of Figures 4.2 and 4.3, in which the resistance and z-position changed reversibly with cycling, these changes were stable for times of at least several hours, in the absence of reapplication of bias. Hence, these micro-scanners can exhibit two kinds of voltage-induced changes: (1) reversible changes in resistance and z-position with application of bias for short periods of time (Figure 4.3), and (2) relatively stable, long lasting changes in equilibrium position that can result from the application of DC bias for long periods of time (Figure 4.4).

(a)

(b)
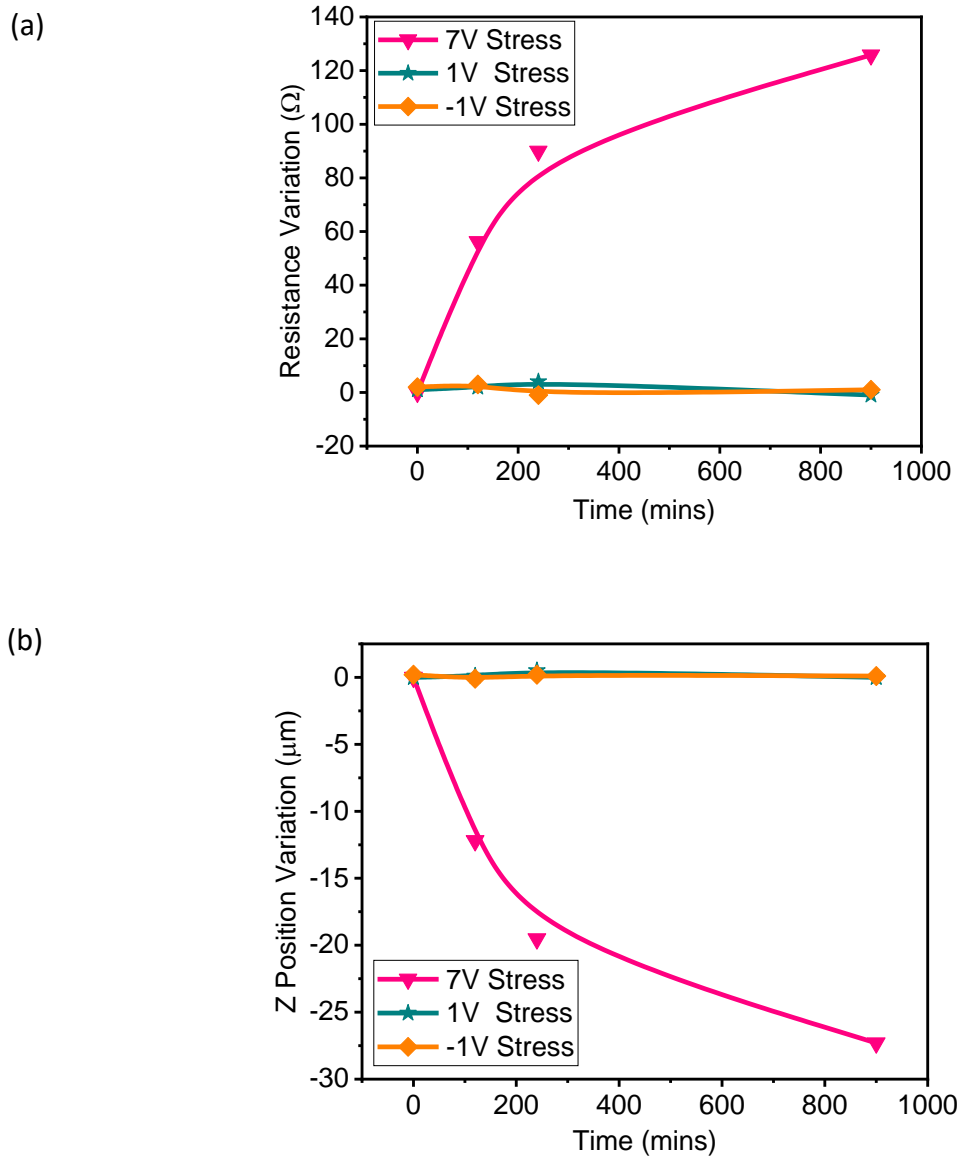
Figure 4.4 Change in (a) Pt resistance and (b) displacement (z-position) as a function of DC stress time. These measurements were performed after removal of DC bias, with 0 V applied to the top electrodes, after the device was allowed to equilibrate to room temperature.

Figure 4.5 shows the z-position and resistance variation after devices were irradiated with 10-keV X-rays to doses up to 2 Mrad(SiO_2). For grounded bias irradiation at the highest doses, the resistance increases by ~ 10% and the z-position decreases by 25%. For devices irradiated with 1 V on the top electrodes, the resistance and z-position are nearly unchanged, with

responses indistinguishable from those of control devices. Changes in responses of irradiated devices were stable for at least several hours, in the absence of application of bias. Hence, radiation-induced charges induce long term changes in the equilibrium position and resistance of the microscanner. Post-irradiation charge densities are evidently approximately balanced for 1 V bias irradiation (no net displacement), but not grounded bias irradiation (net downward displacement).

Because these changes are similar in magnitude and direction to those caused by the application of 7 V DC bias voltage for long times in Figure 4.4, these results suggest that longer-term changes due to the application of DC stress may also be due to dielectric charging, as opposed to other potential factors, e.g., mechanical slip, or other inelastic relaxation processes. Note also in Figure 4.5 that irradiation under grounded bias leads to significant changes in microscanner equilibrium position, but irradiation with 1 V bias does not.

Figure 4.6 shows the responses of irradiated microscanners to test voltages of 1 to 6 V_{DC}, applied to all actuators, after devices were irradiated with (a) all electrodes grounded, or (b) 1 V bias on the top electrodes. The microscanner still performed successfully after irradiation. Applying DC voltage to devices irradiated with all electrodes grounded (Figure 6(a)) leads to upward displacement of the irradiated device, and a return to a position close to original equilibrium values. Applying DC voltage to devices irradiated with 1 V bias (Figure (6b)) leads to displacement above initial equilibrium values.

Taken together, the results of Figures 4.5 and 4.6 suggest that both positive and negative charge can be trapped in device dielectric layers or on their surfaces. The results of Fig. 6 are analogous to (a) post-irradiation recovery or (b) "super-recovery/rebound" often observed for irradiated MOS devices with relatively thick SiO_2 gate dielectric layers. Such recovery or super-recovery is typically caused by annealing of trapped positive charge in SiO_2, in conjunction with stable or increasing negative charge densities in interface (surface) traps [65], [66], [67], [68].

(a)
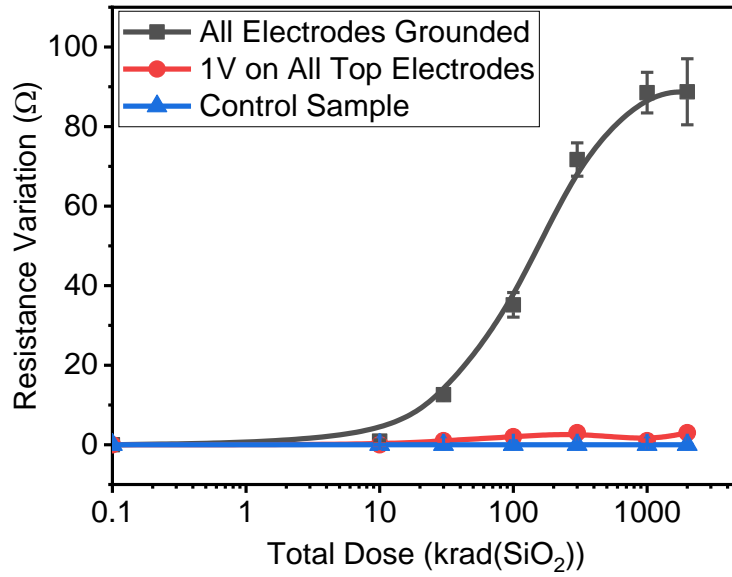
(b)
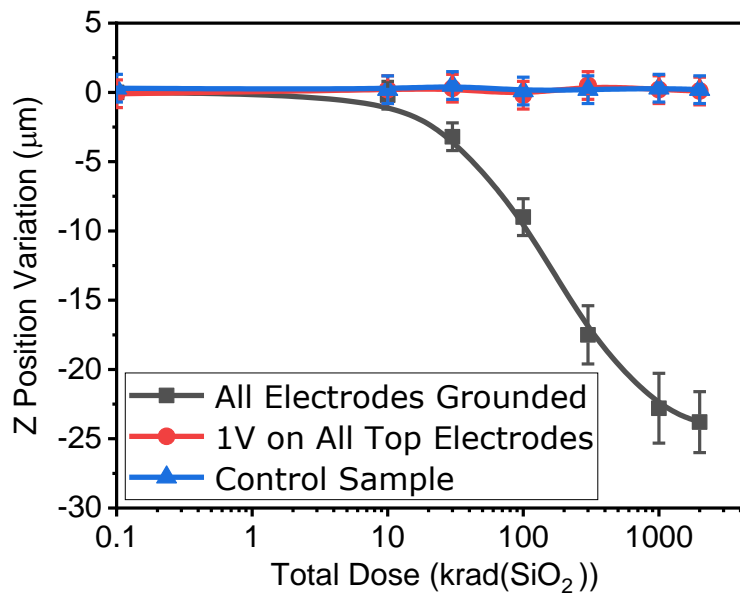
Figure 4.5 Change in (a) Pt resistance and (b) displacement (z-position) as a function of dose. Devices were irradiated with 10-keV X-rays at a dose rate of 31.5 krad(SiO_2)/min with top electrode bias of 0 V or +1 V and other terminals grounded. Measurements were performed after removal of DC bias, with 0 V applied to the top electrodes. Error bars represent the ranges of responses for two different devices. Control devices were unirradiated and not bias stressed.

(a)
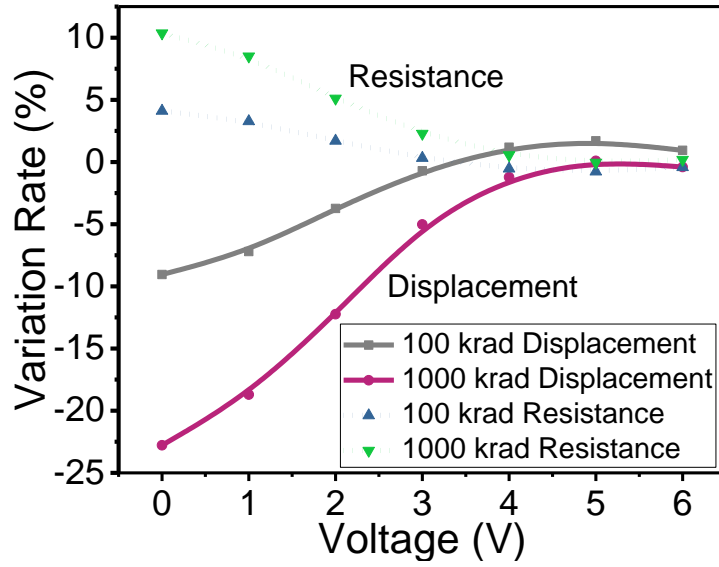
(b)
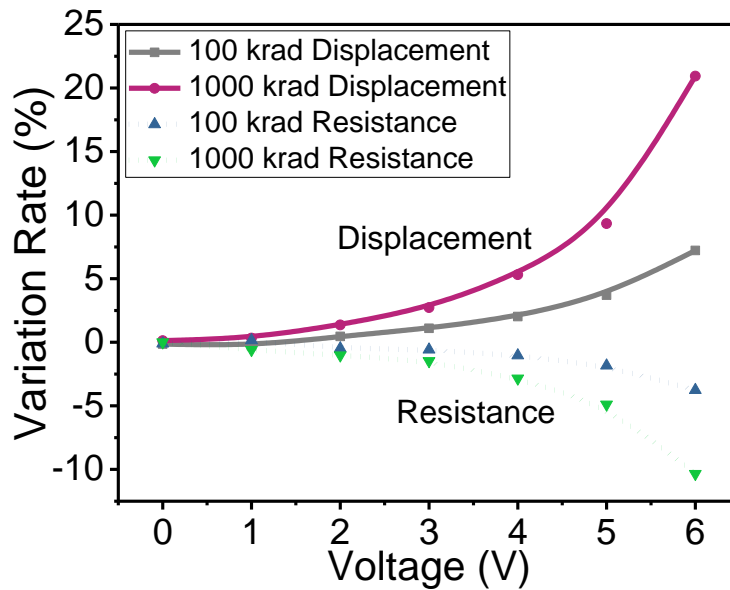
Figure 4.6 Relative changes in Pt resistance and displacement (z-position) of the microscanners of Figure 4.5 as functions of dose and post-irradiation DC bias. Devices in (a) were irradiated with all electrodes grounded. Devices in (b) were irradiated with top electrode bias of +1 V and other terminals grounded.

4.5   Oxygen Ion Irradiation Experiments

To evaluate potential heavy ion effects, a microscanner was irradiated with 14.3 MeV oxygen ions to a fluence of $5.6\times10^{13}/cm^2$, using the Vanderbilt Pelletron [69]. Results are shown in Fig. 7. The electrodes were all grounded during irradiation. The two curves in Fig. 7 represent the changes in z-position and resistance with different test voltages after irradiation. Results are qualitatively consistent with those observed following X-ray irradiation with all pins grounded. The resistance increases, the z-position decreases, and the application of post-irradiation DC voltage leads to recovery of the device toward its original position and resistance.

When oxygen ions interact with the microscanner, they transfer energy to materials via TID and displacement damage effects [3], [68], [19], [70], each of which may potentially affect the positioning of the microscanner. Ion irradiation can create new defects in either the large-area SiO_2 scanner plate at the top of the structure, or in the multiple oxide layers of the bimorph structures that support the scanner plate, potentially leading to increased oxide charging. Displacement damage can generate physical defects in microscanner materials. In this regard, Figure 4.8 shows the results of SRIM simulations [71] of ionizing energy loss in one of the bimorph cantilever structures. Most of the 14.3 MeV oxygen ions penetrate the top layers of the structure without creating defects. Hence, more than 99% of the energy loss in the top layers of the bimorph cantilever is due to ionizing radiation. Significant displacement damage is likely in the SiO_2 layer that underlies the Pt layer. However, the equivalent ionizing dose during the oxygen ion irradiation is more than 40 Grad(SiO_2), which is much higher than doses for X-ray irradiations. In Fig. 4.7, though, the observed z-position and resistance variations are similar to those produced by X-ray irradiation at ~ Mrad(SiO_2) doses. This similarity in responses suggests that (1) TID effects dominate the irradiation process in each case, consistent with results for other types of MEMS devices [3], [19], [70], [11], and (2) TID effects saturate at doses less than or on the order of 1 Mrad(SiO_2) under these bias conditions (all pins grounded). The observed saturation of the TID response is likely due to the high rate of electron-hole recombination that occurs when oxides are irradiated with 0 V applied bias [68], [72], which is the realistic steady-state condition for these devices in a potential space application.
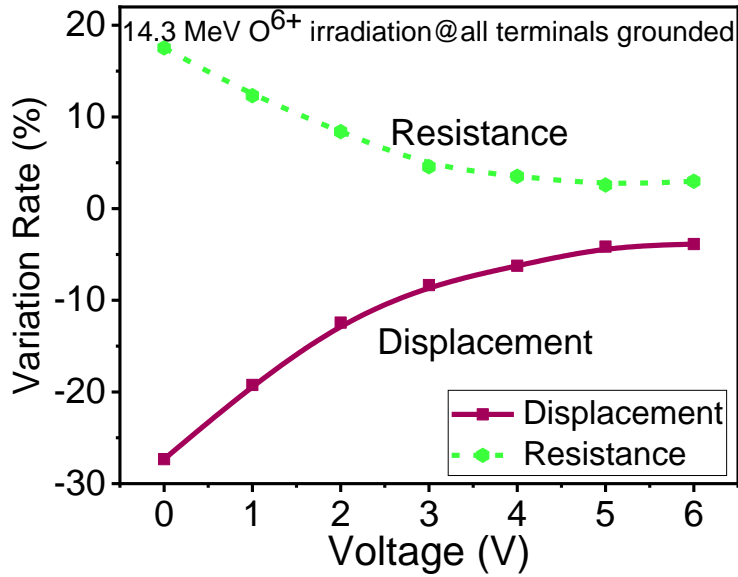
Figure 4.7 Relative changes in Pt resistance and displacement (z-position) as a function of post-irradiation DC bias for microscanners irradiated with 14.3-MeV oxygen ions at a flux of ~7×10^{12}/cm^2/h to a fluence of 5.6×10^{13}/cm^2. Devices were irradiated with all electrodes grounded.
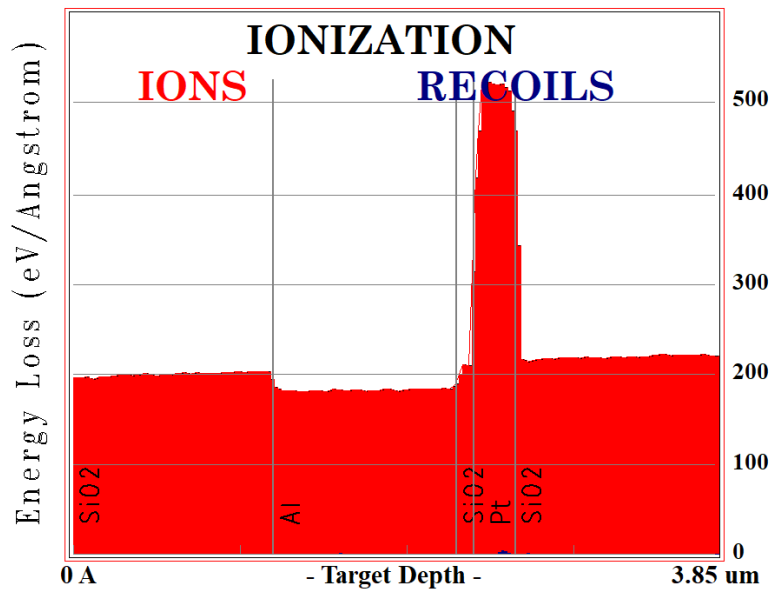
Figure 4.8 SRIM simulation results of ionizing energy loss in the microscanner bimorph structure of Figure 4.1.

4.6   Discussion

The structure in Figure 4.1 includes a number of dielectric layers and surfaces, some of which are in contact with other materials which may be grounded or biased, and others that are floating. These dielectric layers are deposited using CVD methods that are not optimized for electrical response; instead, mechanical performance and stability are the primary considerations. This makes it challenging to assess the potential effects of radiation- and/or bias induced charging on the positioning and resistance of the structure. Nevertheless, with plausible assumptions, some first-order estimates of potential effects can be made.

4.6.1   Scanner Plate Charging

We first consider the potential effects of charging of the 600 μm x 600 μm SiO_2 scanner plate, which is initially at equilibrium, supported by the four bimorph structures. For simplicity, the scanner plate and ground plane can be modeled as a parallel plate capacitor. The net radiation-induced trapped charge on the scanner plate, projected to its lower surface, induces an equal and opposite charge on the top surface of the ground plane. Elementary electrostatics suggests that the resulting downward (attractive) force F on the scanner plate that results from the resulting charge densities is approximately：

$$F = \frac{q^2 N_{sp}^2 A}{2\varepsilon_0}$$

(4-1)

Here q is the magnitude of the electron charge, N_{sp} is the net radiation-induced areal charge density on the scanner plate as projected to the lower surface, A is the scanner plate area, and ε_o is the permittivity of free space. If we assume a value for N_{sp} that is near the lower end of anticipated radiation-induced charge densities, e.g., 5 x $10^{10}/cm^2$, then $F \approx 130$ μN.

We now consider whether a force of ~ 130 μN is sufficient to move the scanner plate. The spring constant of the Al/SiO_2 bimorph cantilever may be estimated via [43]:

$$k_{cantilever} = \frac{EWH^3}{4L^3}$$

(4-2)

Here E is the elastic modulus of the cantilever (70 GPa [73]), W is its width (10 μm), H is its thickness (2 μm), and L is its length (300 μm). Four cantilevers are connected in series to form

the double ISC structure, and 8 double ISC structures support the scanner plate (Figure 4.1). Hence, the combined spring constant of the full structure is [74]:

$$k = \frac{k_{cantilever}}{4} \times 8 = 2k_{cantilever} \approx 0.1 N/m \tag{4-3}$$

The maximum displacement variation of the scanner plate during irradiation is ~ 30 μm from its equilibrium position. The force required to move the microscanner F_d corresponding to 30 μm displacement is therefore:

$$F_d = k\Delta d \approx 3\mu N \tag{4-4}$$

Although the above models include a number of simplifying assumptions, the results show at least qualitatively that scanner plate charging is a plausible mechanism for the observed radiation-induced changes in z-position and resistance.

4.6.2   Bimorph Cantilever Charging

In addition to scanner plate charging, bimorph cantilever beam structures (Figure 4.1) almost certainly contribute to radiation-induced changes in resistance and z-position of the microscanner. Figure 4.9 shows COMSOL simulation results for the bimorph cantilever. In Figure 4.9(a), the simulated surface charge density in the SiO$_2$ layer that overlies the cantilever beam is chosen to be at the upper end of the range of anticipated radiation-induced positive charge densities, $1\times10^{12}/cm^2$, for purposes of illustration. The resulting electrostatic force bends the beam upward. This direction is opposite to that observed in irradiation or DC voltage-stressing experiments.

On the other hand, if there is a negative surface charge density on the SiO$_2$ layer in the beam of $1\times10^{12}/cm^2$, the electrostatic force bends the beam downward, as shown in Figure 4.9(b). This movement is similar to that caused by X-ray irradiation under grounded bias conditions (Figures 5 and 7) or as a result of the application of 7 V DC bias stress (Figure 4). These results imply that trapping of electrons, e.g., in surface states, may contribute to the observed changes in resistance and z-position [75], [76]. Alternatively, trapping of positive charge in these oxide layers can oppose the forces of attraction created by charge trapping in the scanner plate. More work is required to determine the relative roles of these effects.
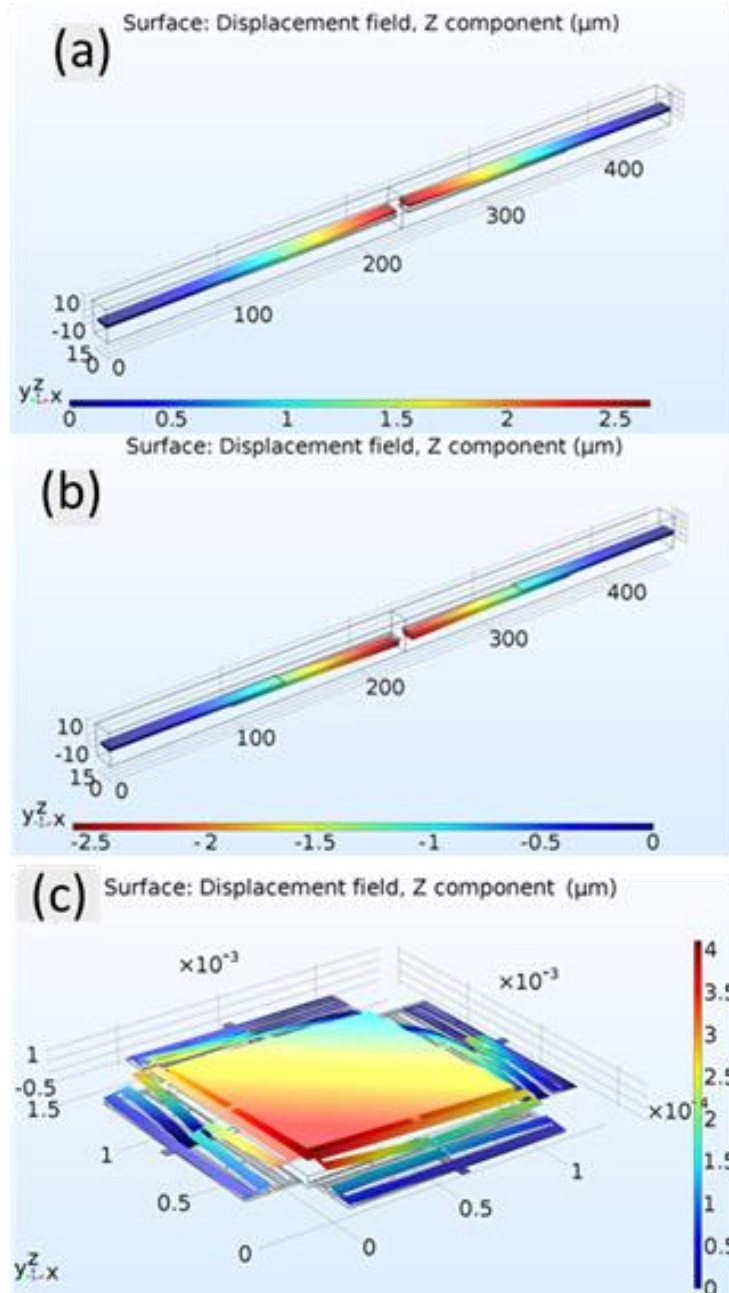
Figure 4.9 COMSOL simulation results of (a) upward and (b) downward displacements caused by (a) positive and (b) negative charge trapping in two s-shape electrothermal actuators that comprise the bimorph cantilever. (c) Disturbance in microscanner piston motion caused by charge accumulation in the elbow parts.

Figure 4.9(c) shows the results of simulating radiation-induced electrostatic force effects

on the elbow parts of the actuator (Figure 4.1). Again, the simulated surface charge density on the SiO_2 is $1\times10^{12}/cm^2$. The electrostatic force is larger in this case than for the anchor portion because of the short distances between the upper and lower portions of the elbow. In this case the electrostatic force causes the two adjacent parts to repel each other. The repulsion causes the scanner plate to both move upward and to exhibit a small tilt, as illustrated in Figure 9(c). Hence, there are not only changes in vertical position, but the microscanner can be rotated, leading to the possibility of signal distortion in device application [74].

We emphasize that, despite the observed changes in z-position and resistance caused by irradiation or bias-induced charging effects described here, the microscanners remained completely functional and controllable through the full series of tests performed in this study. This suggests that a suitable, sensor-based feedback and control system can be developed and applied to adjust biasing voltages to compensate for radiation or dielectric charging induced changes in resistance and z-position, much in the way that equilibrium was restored via the application of DC bias in Figure 6(a).

Finally, given that both the scanner plate and the bimorph cantilever beam structures contain a number of insulating layers, spacecraft charging is likely to also be a significant issue for the potential use of such structures in spacecraft systems [77]. This is an additional factor that must be considered before using such structures in the space environment.

4.7   Conclusions

Responses of Al/SiO_2 bimorph electrothermal microscanners to 10 keV X ray and 14.3 MeV oxygen ion irradiation have been investigated. Results demonstrate the dependence of microscanner displacement on total ionizing dose and/or applied-voltage induced charge trapping in dielectric layers. The resulting electrostatic forces lead to changes in resistance, position, and orientation of the microscanner. These results emphasize that radiation effects on electrothermal MEMS with dielectric layers can be both significant and complex and must be considered and mitigated for potential space applications that require high resolution and long-term reliability.

CHAPTER V

5.   MONTE CARLO SIMULATION OF RADIATION EFFECTS ON GRAPHENE

5.1   Overview and Objectives

Graphene is a single atomic layer of an allotrope of carbon in the form of very tightly bonded carbon atoms organized into a hexagonal lattice [78]. It is the basic structural element of graphite, charcoal, carbon nanotubes and other allotropes. Graphene has attracted widespread interest due to its exceptional electrical, mechanical and optical properties. Carbon atoms in graphene can be substituted by doping, which fundamentally changes the electrical properties of the graphene, enabling its semiconducting capability and a wide range of applications [79]. Potential applications of graphene mechanical properties include flexible electronics [80], nanomechanical resonators [81] and DNA sequencing [82].

The graphene properties are very sensitive to atomic scale defects [83], [84]. For example, decreases in electron mobility [85] or drop in mechanical characteristics [86] have been reported with an increase in defect concentration. However, defects can be useful in some applications, as they make it possible to tailor the local properties of graphene and to achieve new functionalities. Defects can be deliberately introduced into graphene, for example, by irradiation or chemical treatments [87]. On the other hand, inadvertently introduced defects can severely deteriorate the useful properties of graphene in hostile radiation environments, such as outer space. Hence, for the proper use of graphene-based devices, it is important to control defect density and understand the effect on device operation.

Various ions with energies range from keV to MeV have been used to introduce defects in graphene. Compagini et al. demonstrated 500 keV C^+ interaction with graphene [88]. Mathew et al. investigated 2 MeV proton irradiation effects in graphene [89]. Kumar et al. showed the defects in graphene introduced by 100 MeV Ag^{7+} ion irradiation [90].

Molecular dynamics combined with the analytical potential and density functional theory methods are utilized to simulate impacts of energetic ions onto suspended graphene [91]. However, the molecular dynamics simulations should be long enough to be relevant to the time scales of the collision processes being studied. Several CPU-days to CPU-years are needed for one simulation. It is time-consuming and costly to investigate various ions with different energy

irradiation effects on graphene. SRIM, a Monte Carlo computer code to calculate how a moving ion transfers its energy to the target atoms in bulk materials, may not directly be applicable to two dimensional (2D) systems; the sample is treated as an amorphous matrix with a homogeneous mass density in SRIM while the explicit account for the atomic structure is very important in assessing the effects of irradiation on graphene.

In this chapter, the objectives include: (1) Investigate ions bombardment on graphene, (2) New Monte Carlo method programming. (3) Monte Carlo calculation for multilayer graphene and other 2D materials.

5.2 Different Types of Defects in Graphene

The simplest defect in any material is one missing lattice atom. Single vacancies in graphene as shown in Figure 5.1 (a) have been experimentally observed by TEM [92]. Double vacancies can be created either by the coalescence of two single vacancies or by removing two neighboring atoms. The removal of more than two atoms may be expected to result in larger and more complex defect configurations as Figure 5.1 (b) shows. The interstitials shown in Figure 5.1 (c) refers to a disorder of carbon in the plane of the graphene. Two or more carbon atoms may share one lattice site. Substitution indicated in Figure 5.1 (d) appears when a carbon atom is replaced by the incident ion.

The proposed Monte Carlo approach is described in detail in this section. First, different defect types generated under energetic ion irradiation and binary collision model are described. Then the impact parameter is calculated according to the atomic structure of graphene. Furthermore, the defect yield in graphene depends strongly on the scattering angle of the incident energetic ions. Cascade collisions in graphene plane are taken into account in small angle scattering.
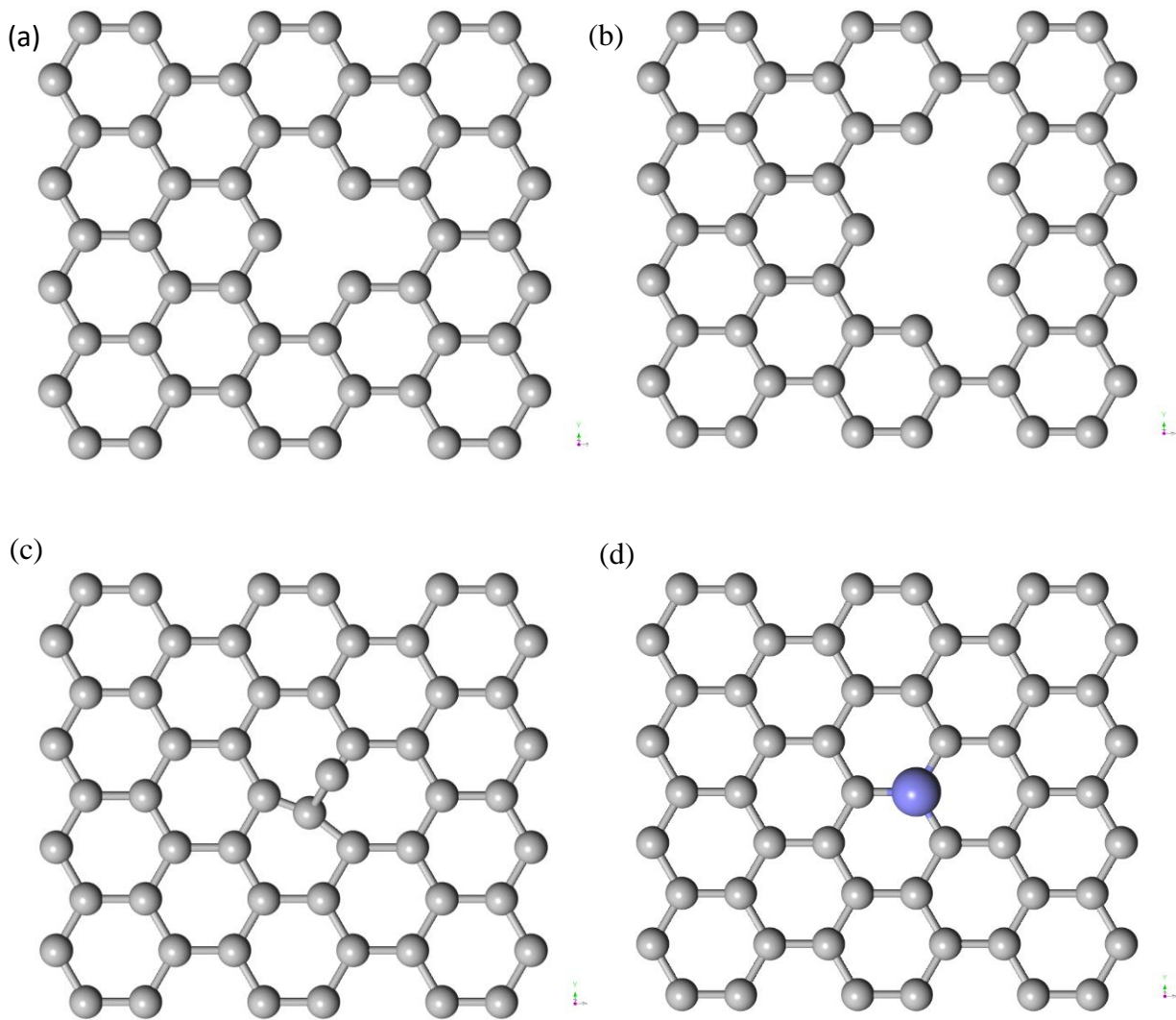
Figure 5.1 Defect patterns in graphene: (a) single vacancy; (b) multiple vacancies; (c) interstitials; (d) substitution.

5.3 Binary Collision Model

As illustrated in Figure 5.2, the simulation system consists of incident ions and a monolayer graphene sheet. Ions (yellow) perpendicularly bombard the graphene sheet. Normally, the incident ion beam size is assumed to be larger than the size of the graphene sheet so that the incident ions are uniformly distributed over surface of the graphene. Each carbon atom position in the graphene sheet is identical, so, the irradiation damage can be derived from the results of binary collisions between one ion and one carbon atom.
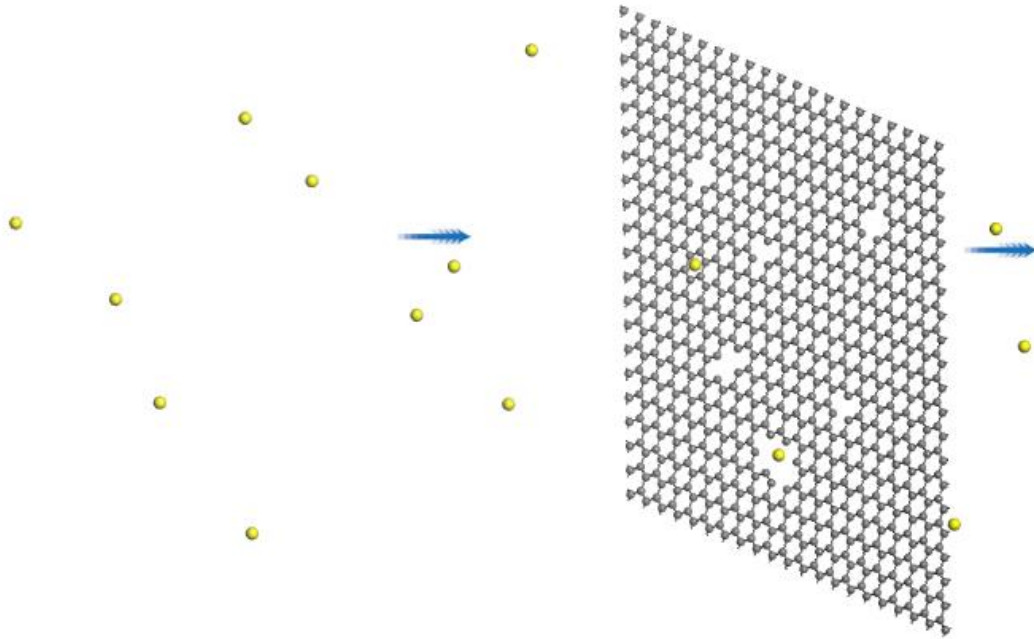
Figure 5.2 Energetic ions bombardment on graphene sheet.

Atomistic simulation models based on the binary collision approximation (BCA) are much faster than MD models. The BCA is a high-energy approximation, especially appropriate when high-energy encounters dominate the phenomena being studied. At low energies, where recoil trajectories are less easily represented in terms of discrete collisions, the BCA becomes less useful. On the other hand, relativistic effects should be taken into account at ultra-high energy. In general, the BCA approximation should be appropriate for ion energies in the range of ~ 100 keV to ~ 100 MeV [93].

Figure 5.3 shows an elastic collision between a projectile atom (yellow) of mass m_1, charge q_1 and initial kinetic energy E, and an initially stationary carbon atom (gray) of mass m_2 and charge q_2. The impact parameter b shown in the figure is defined as the perpendicular distance between the path of a projectile and the center of a potential field created by a carbon atom that the projectile is approaching. The collision of an electron or ion with a carbon nucleus can be treated by using a simple Coulomb potential since the screening effect of the surrounding electrons can be neglected [94].

Figure 5.3 Classical elastic scattering.

The scattering angle of the projectile θ, the scattering angle ϕ of carbon atom and the kinetic energy E_1 of carbon atom after collision can be derived using the following formula [94]:

$$b = \frac{k \cdot q_1 \cdot q_2}{2 \cdot E} \cdot \sqrt{\frac{1+\cos\theta}{1-\cos\theta}} \qquad (5\text{-}1)$$

$$\phi = \frac{\pi}{2} - \frac{\theta}{2} \qquad (5\text{-}2)$$

$$E_1 = \frac{4Em_1m_2}{\left(m_1+m_2\right)^2}\sin^2\frac{\theta}{2} \qquad (5\text{-}3)$$

in which k is Coulomb's constant.

The minimum energy transferred to the atom required to produce a vacancy-interstitial (Frenkel) pair that does not spontaneously recombine is called the displacement energy E_d. In graphene, the displacement energy of a carbon atom is 22 eV [95]. A Frenkel pair is created in the collision process if $E_1 > E_d$.

5.4   Atomic Structure and Impact Parameter

Impact parameter is a very important factor, affecting not only the scattering angle, but also the scattering energy. The atomic structure of graphene must be taken into account in determining the impact parameter. In graphene, each carbon atom is densely packed in a regular atomic-scale hexagonal pattern. The atoms are about 1.42 Å apart. Each carbon atom in the graphene plane is identical.
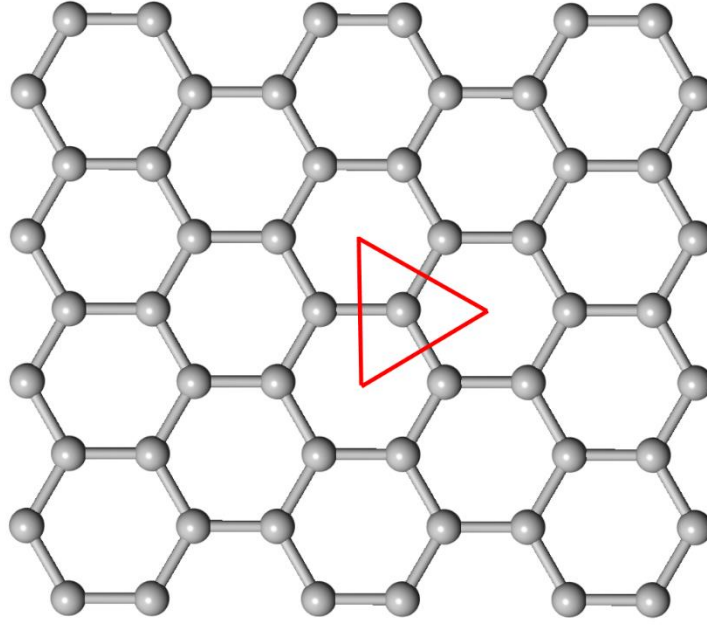
Figure 5.4 Impact parameter distribution.

The impact parameter distribution depends on the relative position of the incident ion to the target carbon atom. The carbon atom collision probability relies on the area it occupies (sensitive area) on the graphene plane since the incident ions are uniformly distributed in space. The impact parameter does not have a fixed value, but is described by a statistical distribution. This distribution depends on the relative position of the incident ion to the target carbon atom. Besides, the carbon atom collision probability relies on the area it occupies (sensitive area) on the graphene plane since the incident ions are uniformly distributed in space. For a target atom in graphene, an equilateral triangle sensitive area shown in Figure 5.4, with the target carbon nucleus in its center, is formed by connecting the centers of three adjacent hexagonal cells which share the target carbon atom. The incident ions that fall into this equilateral triangle area will make elastic collisions with the target carbon nuclei. Each target carbon atom in the graphene

sheet has the same equilateral triangle sensitive area. The impact parameter's distribution can be derived from incident ions' distribution in the sensitive area.

As Figure 5.5 shows, the target carbon nucleus located in the center of the equilateral triangle with coordinates (0, L/2). L is the length of the C-C bond in graphene. The incident ions distribute uniformly in the equilateral triangle area. The horizontal coordinate of the incident ion is an equally distributed random variable between points A point and B. The vertical coordinate of the incident ion is also an equally distributed random variable and its equally distributed range can be derived by its corresponding horizontal coordinate. The incident ions coordinates can be expressed as:

$$x = random\left(-\frac{\sqrt{3}}{2}L, \frac{\sqrt{3}}{2}L\right)$$

$$y = random\left(0, tan\frac{\pi}{3} \times \left(\frac{\sqrt{3}}{2}L - |x|\right)\right)$$

With these coordinates, the distribution of impact parameter b can be obtained by using the distance formula.
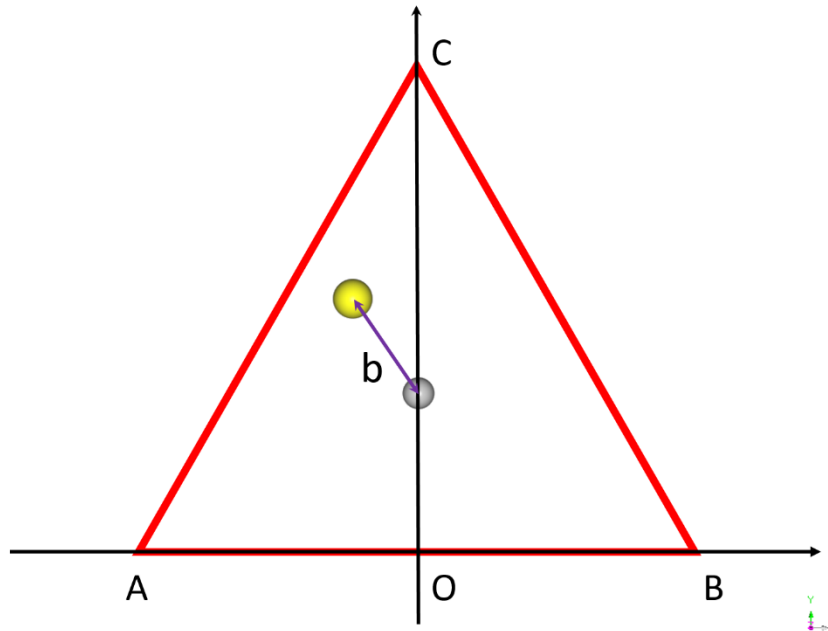
Figure 5.5 Impact parameter calculation.

Another random variable that needs to be considered is the incident ions' kinetic energy. Normally, the incident ions come out from a particle accelerator and the kinetic energy E follows a normal distribution. The distribution of E can be expressed as:

$$f(E)=\frac{1}{\sigma\sqrt{2\pi}}e^{-\frac{(E-E_0)^2}{2\sigma^2}} \tag{5-4}$$

in which E_0 is the user preset ion kinetic energy, σ is the standard deviation which determined by the accelerator.

The Monte Carlo approach is based on the above discussion. First, the kinetic energy and impact parameter of one incident ion are sampled according to their distr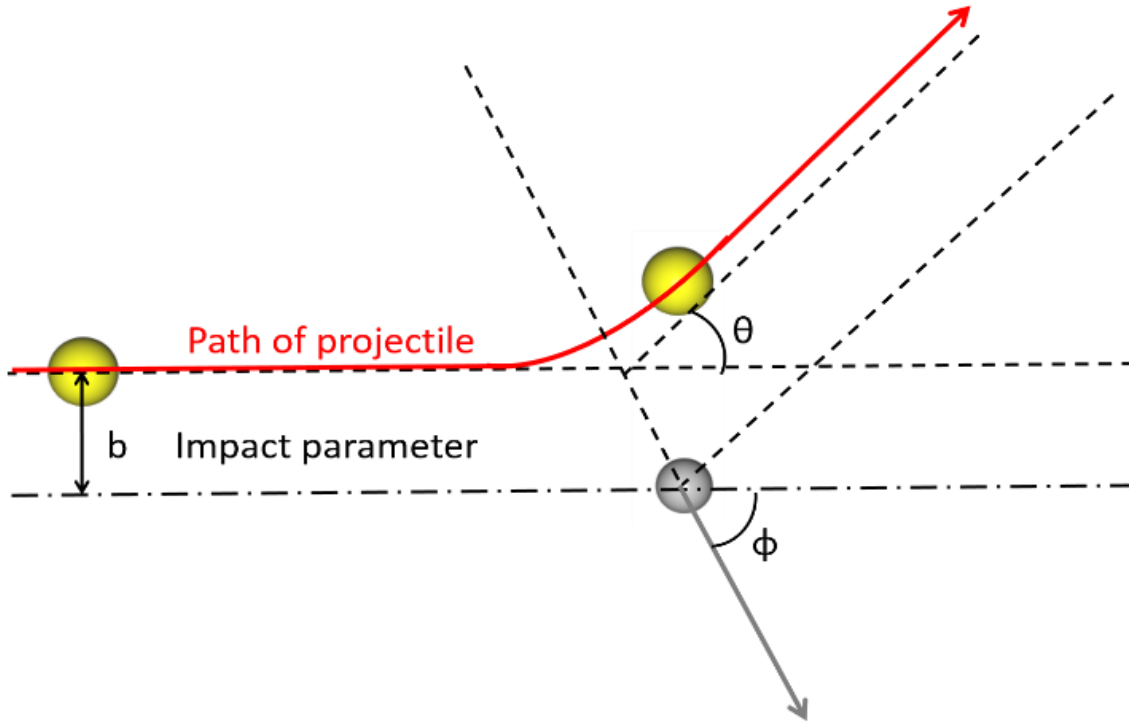ibution. Then, the scattering angle of the projectile θ, the scattering angle ϕ of carbon atom and the kinetic energy E_1 of carbon atom after collision are calculated using formula (5-1) to (5-3). The whole process is repeated N times since collision results of one incident ion cannot reflect the randomness and statistical features in the collision process. At last, the carbon atoms movements after collision are analyzed based on the statistical results of the Monte Carlo simulation.

The Monte Carlo simulation flowchart is shown in Figure 5.6. We use $N = 10^6$ in this chapter. The program simulates 10^6 ions incident onto one target carbon atom in graphene one by one. A complete execution of the proposed Monte Carlo simulation (written with MATLAB code; see appendix) on Intel i5-4670 and Windows 10 Pro takes less than 1 min.
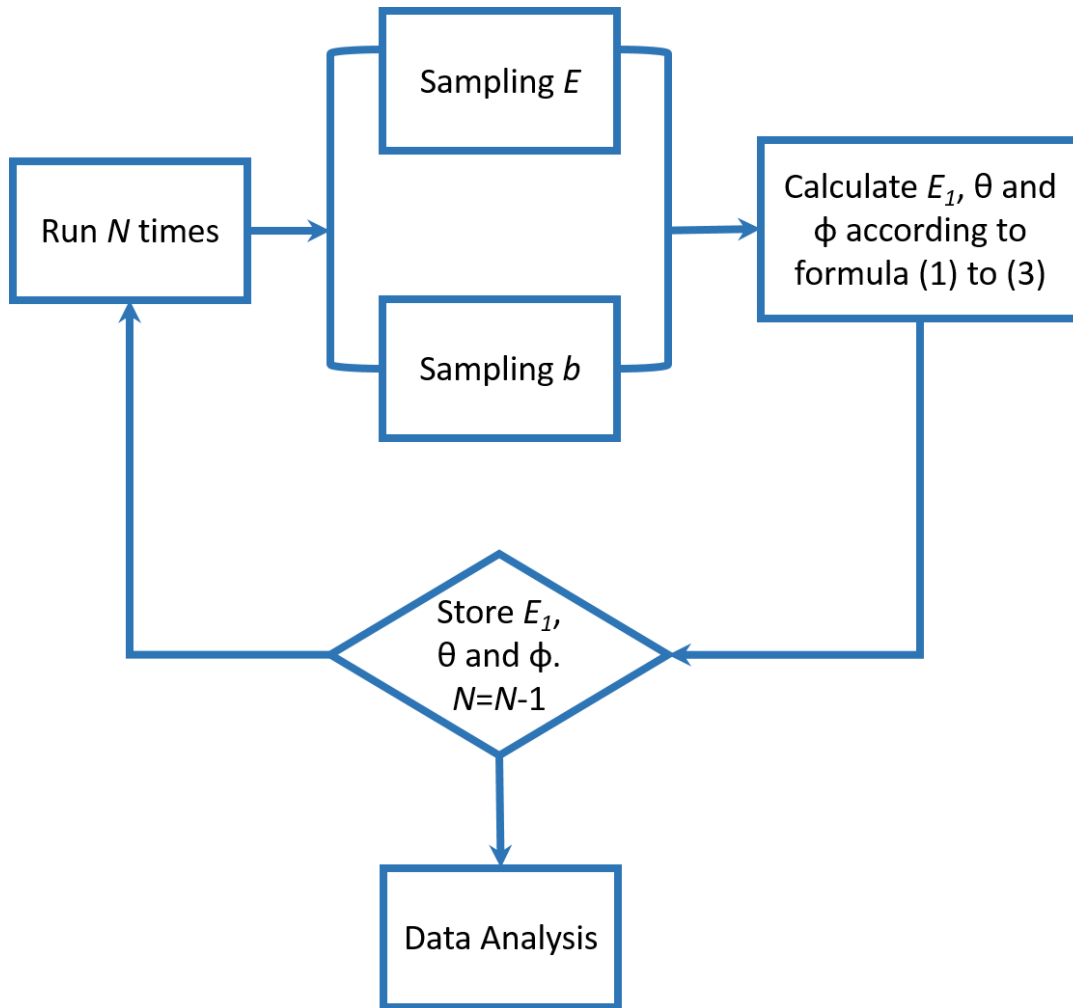
Figure 5.6 Monte Carlo simulation flowchart.

5.5   Small Angle Scattering and in Plane Cascade Collision.

The carbon atom's movements after collision and defect generation strongly depend on its scattering angle. The scattering angle of the incident ion is inversely proportional to E and b according to formula (5-1). Hence the scattering angle of incident ions with high energy E is usually small (0.1-10˚) and the scattering angle of the corresponding target carbon atom is close to 90˚. That means the incident ion "passes through" the graphene sheet without changing its direction while the impacted carbon atom continues to move in the graphene plane.
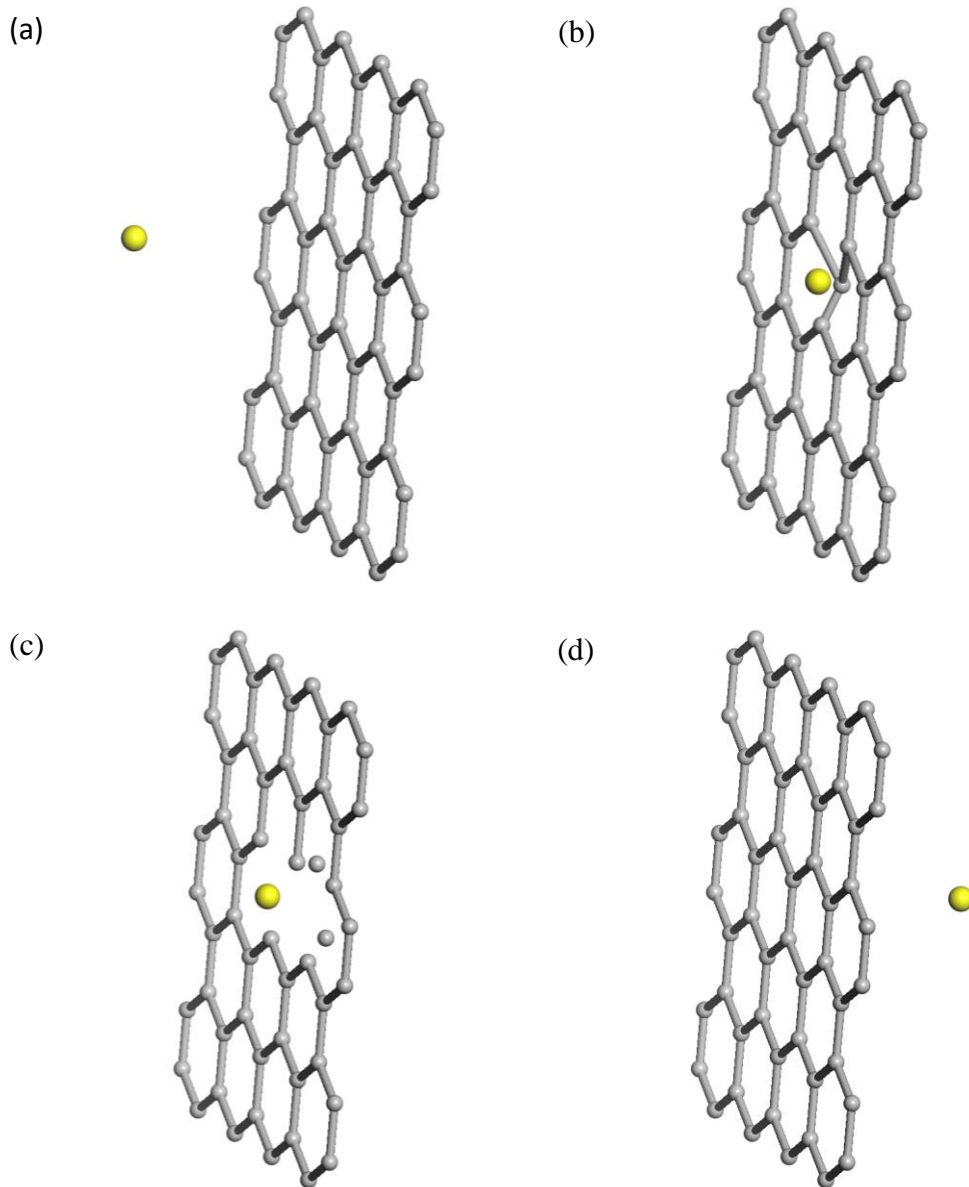
Figure 5.7 The collision between high energy incident ion and target carbon nucleus and their movements after collision.

The collision between a high energy incident ion and target carbon nucleus and their movements after collision are described in Figure 5.7. Figure 5.7(a) shows an ion bombardment perpendicular to the graphene sheet. When the ion approaches the graphene sheet, the corresponding target carbon atom gains kinetic energy E_1 through the elastic collision and moves aside from its original position to allow the ion pass through, as shown in Figure 7(b). When E_1 is less than the displacement threshold, the carbon target atom oscillates in the graphene plane

around its original position, and finally returns to its original place as Figure 5.7(d) shows. When E_1 is larger than the displacement energy, the target carbon atom is knocked out from its original position and a single vacancy and interstitial defects are created in the collision process. The knocked out energetic target carbon atom continues to move in the graphene plane and make cascade collisions with other carbon atoms in the graphene sheet as Figure 5.7(c) shows. Multiple Frenkel pairs (Multiple vacancies and interstitials defects) are created in this cascade collision process.

There are many physical models of calculating the cascade collision damage generated by primary knock-on atom (PKA). Kinchin and Pease estimate the number of Frenkel pairs generated by a PKA with energy T [94]:

$$N_d = 0 \qquad \text{if } T < E_d$$

$$N_d = 1 \qquad \text{if } E_d \leq T \leq 2E_d$$

$$N_d = T/2E_d \qquad \text{if } 2E_d \leq T \leq E_a$$

$$N_d = E_a/2E_d \qquad \text{if } T > E_a$$

At energy E_a (~ keV, we use $E_a = 5$ keV in the Monte Carlo simulation for simplicity), most energy is lost by transfer to electrons. Below E_a, the recoils lose energy entirely by hard-core elastic scattering. Hence, the knocked-out target atom in graphene can be treated as a PKA with energy $E_1 - E_d$ and the number of Frenkel pairs generated by this PKA is $(E_1 - E_d)/2E_d$ when $(E_1 - E_d) < 5$ keV.

When E is larger than 1 MeV, most of the scattering angles ϕ are close to 90˚. The defects in the graphene sheet are generated by primary ion collisions and the subsequent carbon atom's cascade collisions in the graphene plane.
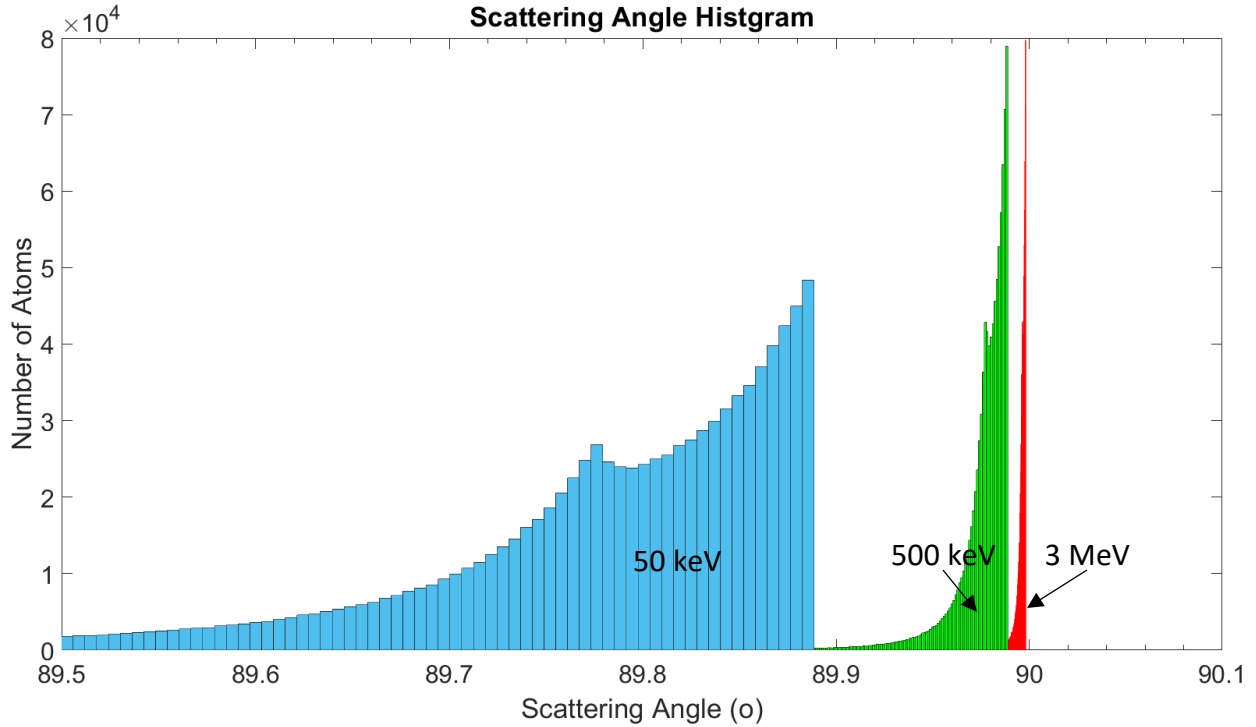
Figure 5.8 The distribution of carbon scattering angle ϕ after collisions with 3 MeV, 500 keV and 50 keV He$^+$ ions.

Figure 5.8 shows the distribution of carbon scattering angle ϕ after collisions with 3 MeV, 500 keV and 50 keV He$^+$ ions calculated by the proposed Monte Carlo approach. 10^6 He$^+$ ions impinge on the target carbon atom in graphene one by one, and the scattering energy E_1 and angle ϕ after collisions are recorded. Most scattering angles are very close to 90˚ and almost no energy is lost by transfer to electrons in the collision when E is 3 MeV. When E is smaller than 1 MeV but larger than 500 keV, a small portion of the scattering angle ϕ deviates from 90˚ and energy transferred to electrons in the collision is small. For example, the 500 keV He$^+$ (green) histogram in Figure 5.8 shows this trend. The cascade collision in the graphene plane still dominates the carbon atoms movements after the collision. The defects in the graphene sheet can be calculated by adding the Frenkel pairs generated in the primary ion collision and following the carbon atom's cascade collisions in the graphene plane.

As the energy E decreases from hundreds to tens of keV, more and more impacted carbon atoms are displaced from the graphene plane. The cascade collisions are not limited in the graphene plane. For example, the blue circles (50 keV He$^+$ bombardment) in Figure 5.8 show

68

this situation. Since the number of cascade collisions that happen before the knocked-out carbon atoms leave the graphene plane is unknown, the defect generation in the collision process is difficult to evaluate. But the proposed Monte Carlo approach can be used to estimate the upper bound and lower bound of the defect numbers in the graphene. First, we assume that there are no carbon atom cascade collisions in the graphene plane. The defects are only created by primary collision of incident ions. This is the lower bound of the number of defects. Then we suppose that all the knocked-out atoms move in the graphene plane. The defects are created by the primary collision of incident ions and the following carbon atoms cascade collisions. This is the upper bound of the number of defects.

5.5   Simulation Results of C Ions with Different Energy

The proposed Monte Carlo simulation is used to investigate different ion irradiation effects on graphene sheets. First, we explore the influence of incident ion energy E on defect generation in a graphene sheet. Then, different types of ions with the same energy are used to explore the effects of incident ion nuclei mass and charge. After that, published irradiation results are evaluated using the Monte Carlo simulation.

Carbon ions with different incident energies have been widely used for introducing defects to graphene. In this section, 6 MeV, 3 MeV and 1 MeV C ions irradiation effects are studied and dependence of defect generation on incident ion energy is revealed by Monte Carlo simulation. Defect yield (defects generated by one ion) can be obtained by Frenkel pairs / N. The number of single vacancy and multiple vacancies depend on the target carbon atoms scattering energy E_1. If $E_d < E_1 < 3E_d$, one single vacancy is created by the PKA collision. If $E_1 > 3E_d$, multiple vacancies are created by the PKA collision and cascade collisions in the graphene plane. The yield can be obtained by dividing the number of single vacancy and multiple vacancies by N. For each incident energy, we run 10 Monte Carlo simulations and the results are shown in Figure 5.9.

(a)

(b)
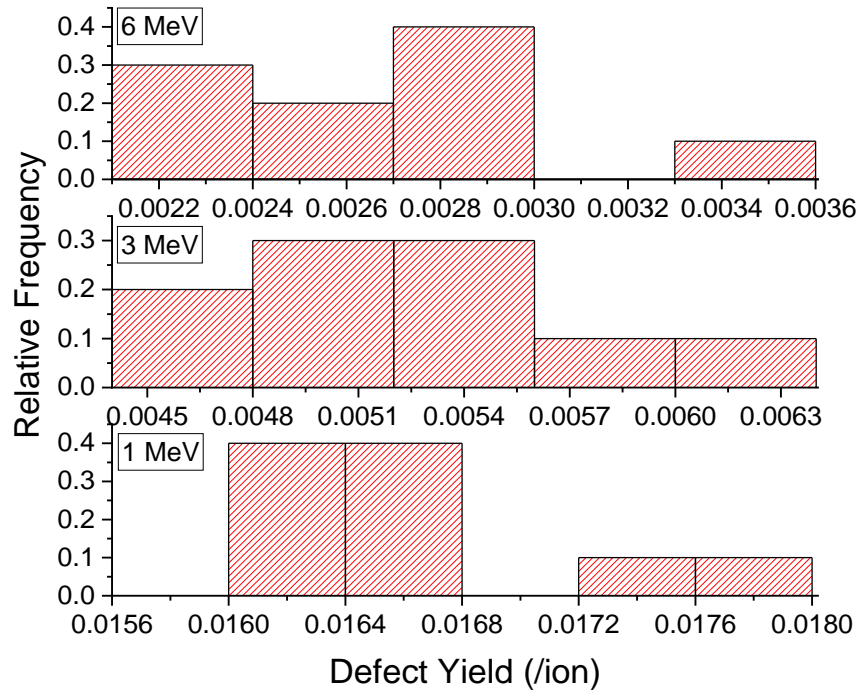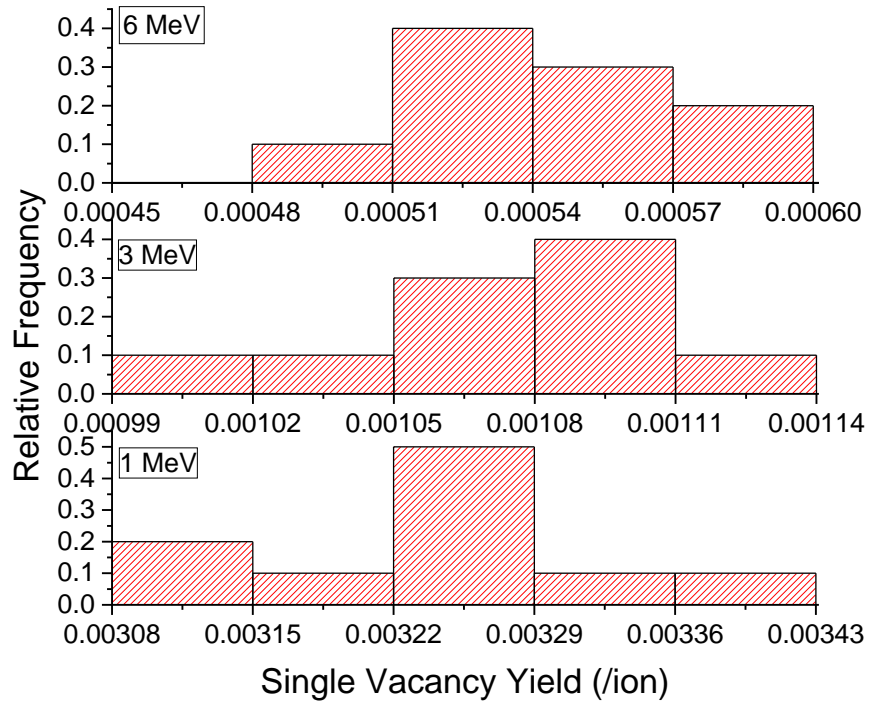
Figure 5.9 The distribution of (a) defect yield, (b) single vacancy yield and (c) multiple vacancies yield in graphene sheet after collisions with 6 MeV, 3 MeV and 1 MeV C ions.
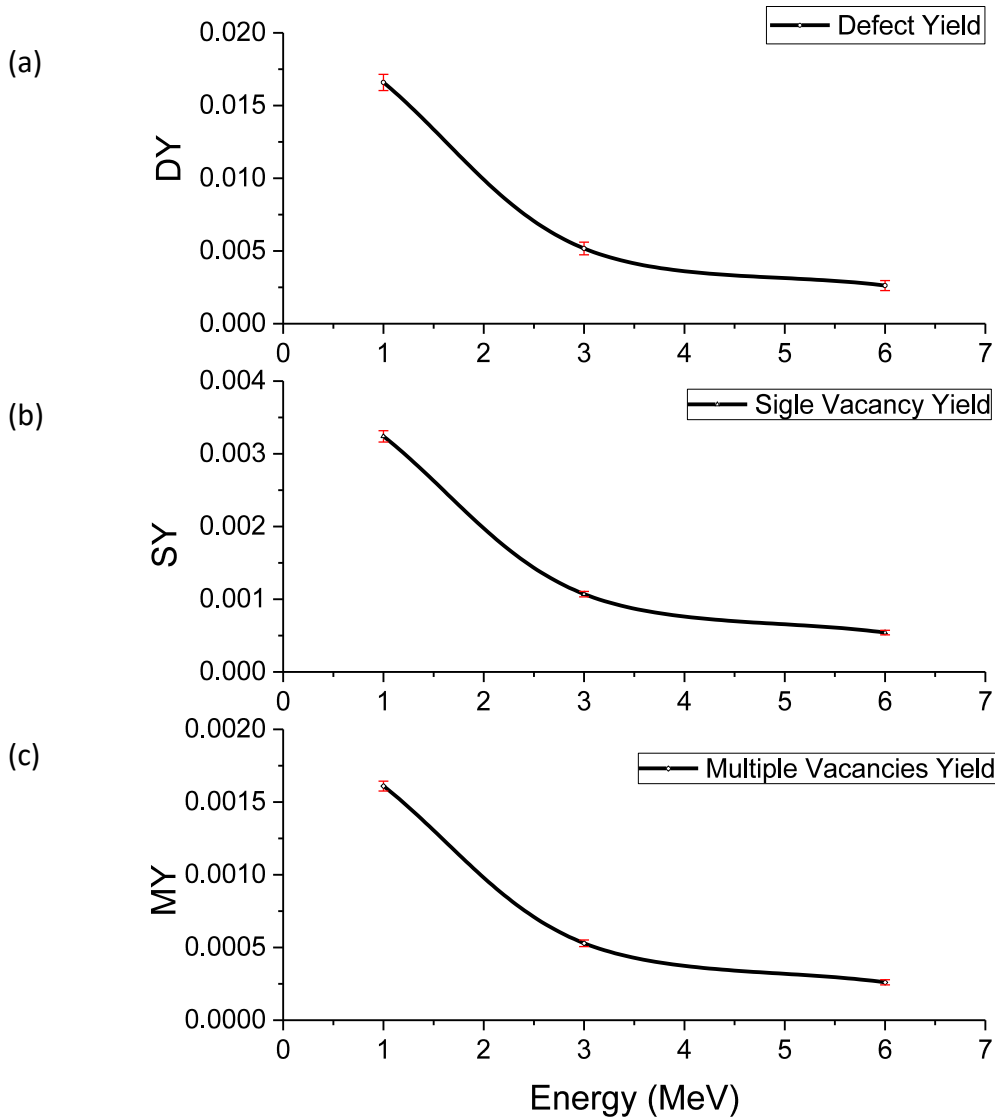
Figure 5.10 The relationship between (a) defect yield (DY), (b) single vacancy yield (SY) and (c) multiple vacancies yield (MY) and incident energy.

The simulated defect yield is very close to the published defect yield test results of C ion bombardments on SiO_2-supported graphene [96]. Since the number of sputtered ions from the SiO_2 surface is 0 (calculated by SRIM), the substrate should have little effect on defect generation in the graphene. Figure 5.10 shows that the defect yield, single vacancy yield and multiple vacancies yield decrease as the incident energy increase. These three curves have the same trends. These results can be explained by considering the impact parameter distribution.

From formula (5-1) and (5-3), we can get the relationship between impact parameter b and the incident energy E, target carbon atom scattering energy E_1:

$$b^2 = \frac{k^2 q_1^2 q_2^2 m_1 m_2}{E E_1 (m_1 + m_2)^2} - \left(\frac{k q_1 q_2}{2E} \right)^2$$

(5-4)

As Figure 5.11 shows, the impact parameter distributes uniformly inside the red equilateral triangle. We suppose $b = b_1$ when $E_1 = 3E_d$ and $b = b_2$ when $E_1 = E_d$ and $b_1,\ b_2$ are in the equilateral for high incident energy E. The probability of scattering target carbon atoms with energy $E_d < E_1 < 3E_d$ is:

$$P(E_d < E_1 < 3E_d) = P(b_1 < b < b_2)$$
$$= C \cdot \pi (b_2^2 - b_1^2) = C \cdot \pi \cdot \frac{k^2 q_1^2 q_2^2 m_1 m_2}{E(m_1 + m_2)^2} \left(\frac{1}{E_d} - \frac{1}{3E_d} \right)$$

(5-5)

in which C is a constant. This probability is equal to the single vacancy yield. Similarly, the multiple vacancies yield can be expressed as:

$$P(E_1 > 3E_d) = P(b < b_1)$$
$$= C \cdot \pi \cdot b_1^2 = C \cdot \pi \cdot \frac{k^2 q_1^2 q_2^2 m_1 m_2}{E(m_1 + m_2)^2} \left(\frac{1}{3E_d} \right)$$

(5-6)

From formula (5-5) and (5-6), we can get two important conclusions:

1. The defect yield, single vacancy yield and multiple vacancies yield are inversely proportional to the ion incident energy.

2. The single vacancy yield $= 2 \times$ multiple vacancies yield.

As the incident energy E increases, the b_1 and b_2 decrease and the area outside the green ring increase. That means the probability $P\ (E_1 < E_d)$ increases. Hence the phonon yield in the collision process increases.

Production of defects in graphene under ion irradiation with different incident energy has been simulated by the analytical potential molecular dynamics [97]. The reported defect yield, single vacancy yield, double vacancies yield decreases as the incident energy increase within the high energy range, which shows good agreement with our analysis results.
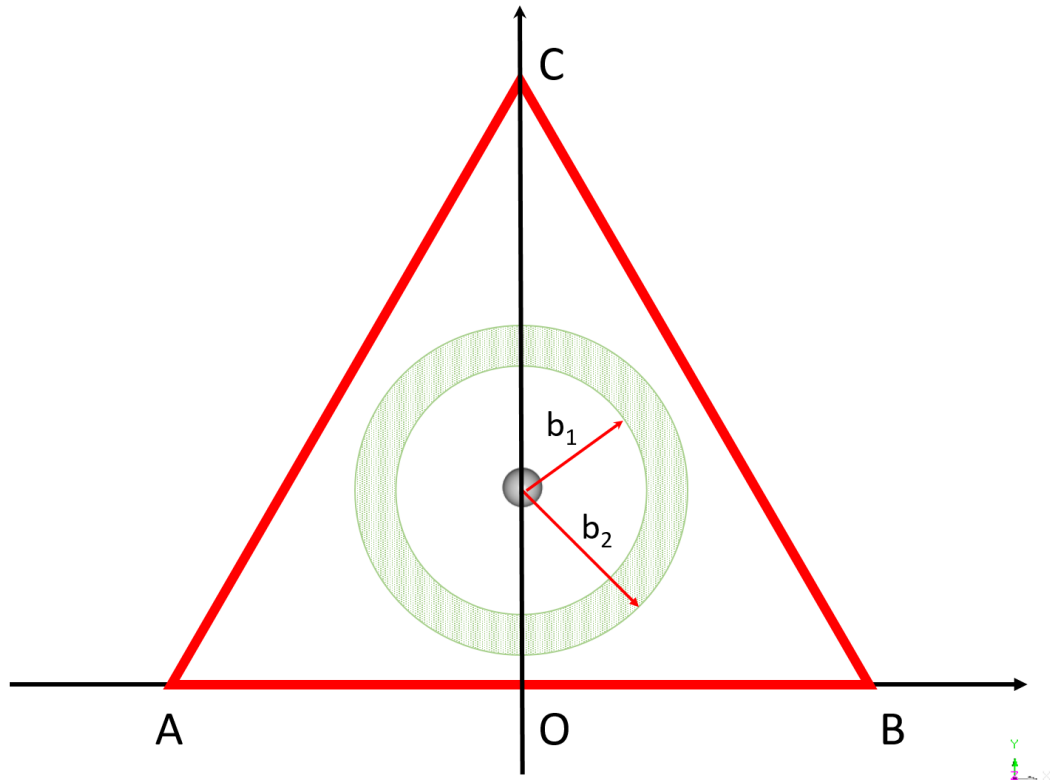
Figure 5.11 The relationship between impact parameter and energy

5.6   Simulation results of Various Ions with 1 MeV Incident Energy

The incident ion's mass m_1 and nuclear charge q_1 play important roles in defect calculations. From formulas (5-5) and (5-6), the defect yield, single vacancy and multiple vacancies yield should increase with increasing atomic number. 1 MeV He, Ar and Xe ions are used to present this trend. For each incident energy, we run 10 Monte Carlo simulations and the results are shown in Table 5.1 and Figure 5.12.
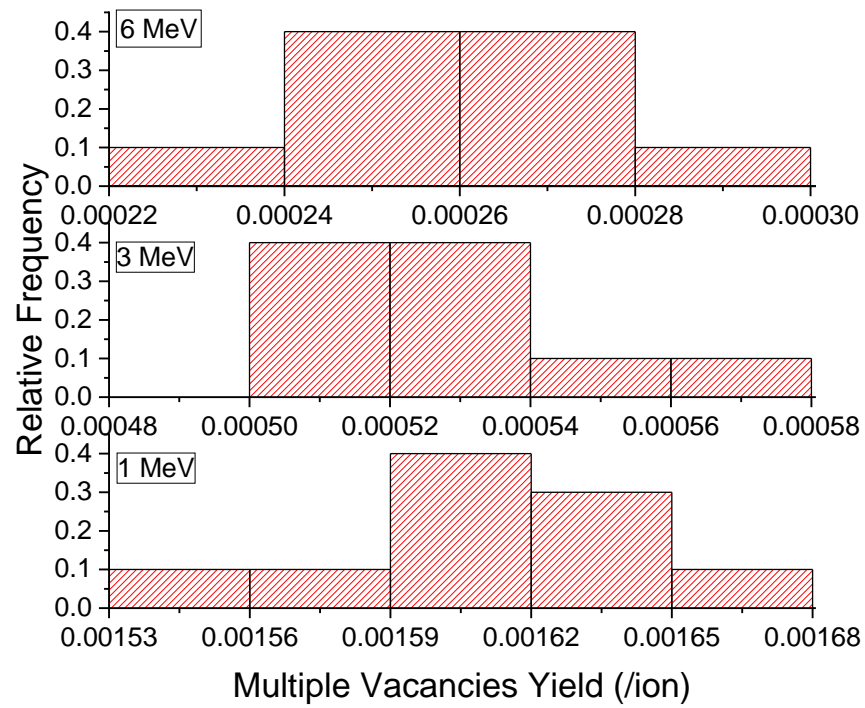
(a)

(b)

(c)
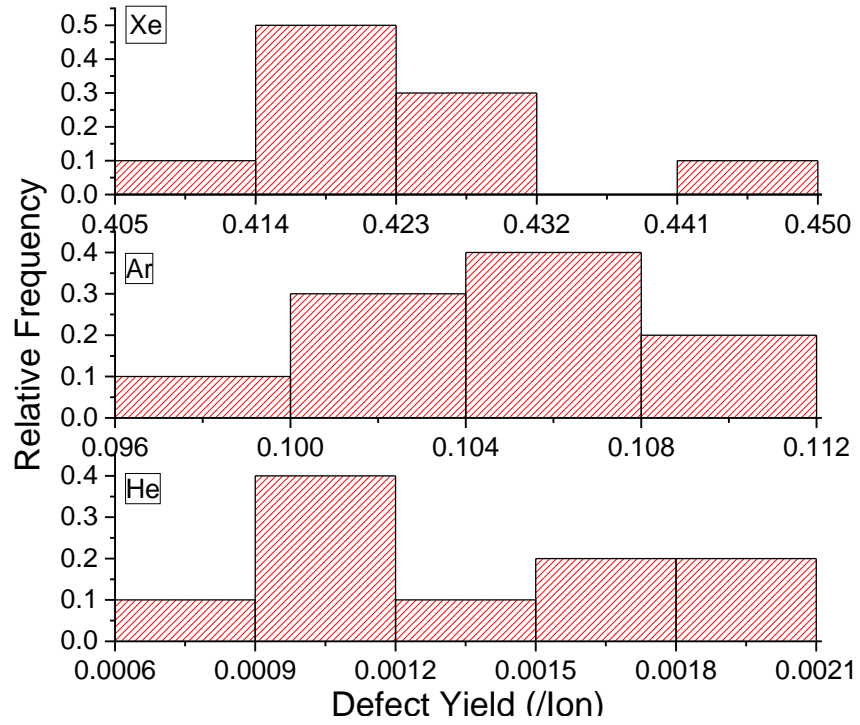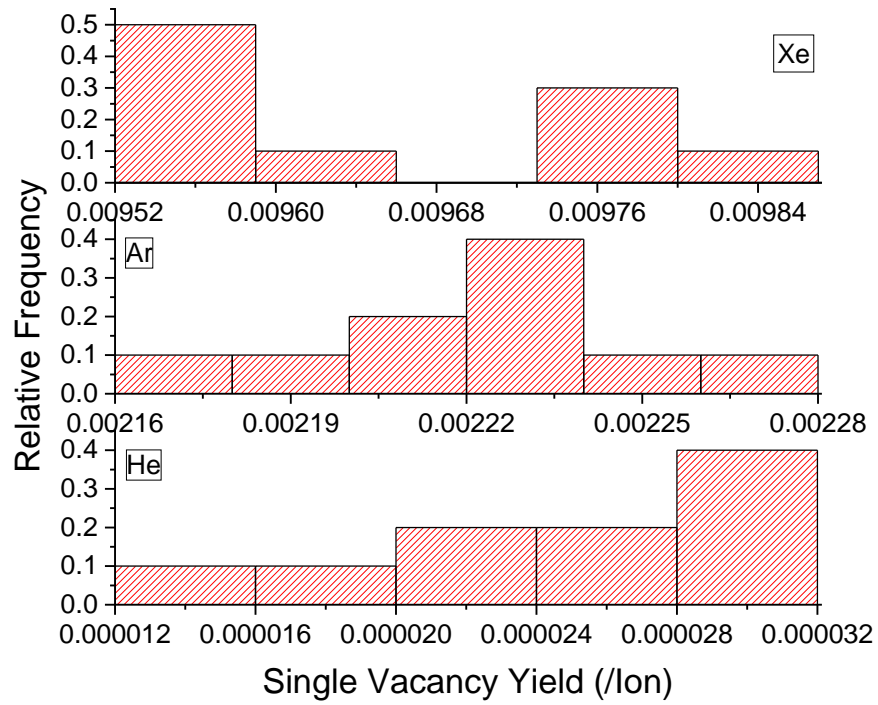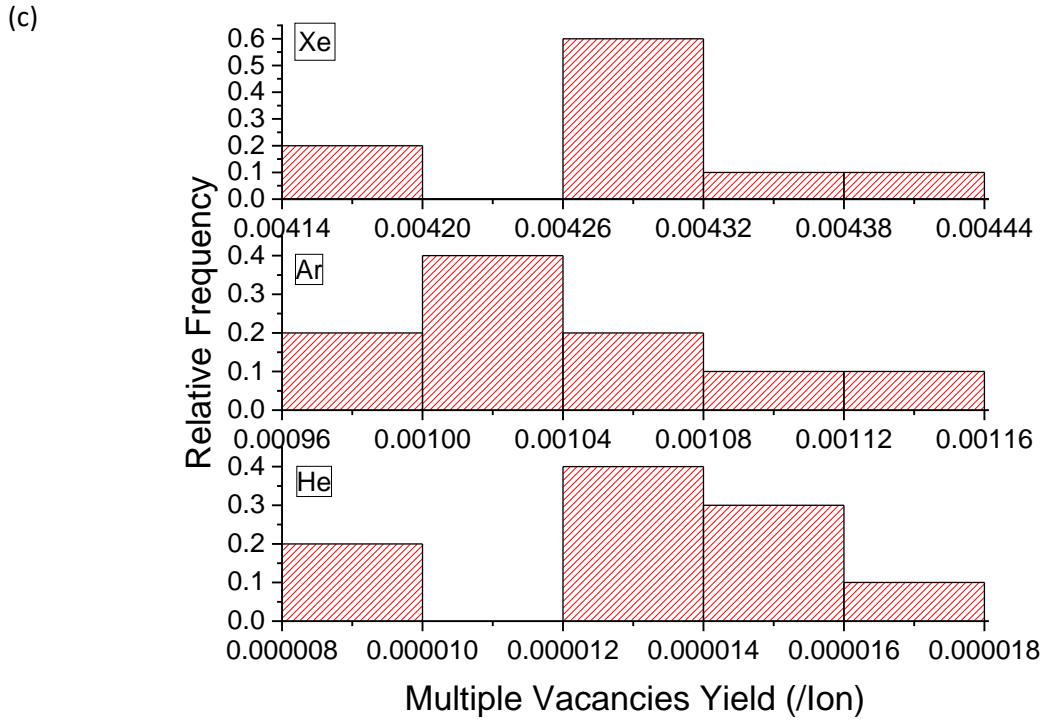
Figure 5.12 The distribution of (a) defect yield, (b) single vacancy yield and (c) multiple vacancies yield after collisions with 1 MeV Xe, Ar and He ions.

Table 5.1 The Monte Carlo Simulation Results (/ion):

Ion	Monte Carlo Defect Yield	Single Vacancy Yield	Multiple Vacancies Yield	Molecular Simulation Defect Yield [98]
Xe	0.427	0.00965	0.00428	0.32
Ar	0.105	0.00222	0.001	0.07
He	0.00128	2.46×10^{-5}	1.3×10^{-5}	<0.02

The Monte Carlo simulation results are compared with the published molecular dynamic simulation results in table 5.1. The molecular dynamic simulation cannot give the defect yield of

He$^+$ ions, since it only includes one ion with 1500 independent simulations and cannot give reliable results of low probability events.

5.7   Comparison with Experimental Irradiation Results

The defect yield in the graphene irradiation experiments can be directly extracted from the I_D/I_G ratio in Raman spectra at low defect density (less than 3.2×10^{11}/cm^2), avoiding the defect coalescence effect. The defect density n_D can be expressed as [99], [100]:

$$n_D \left(cm^{-2} \right) = \frac{(1.8 \pm 0.5) \times 10^{22}}{\lambda_L^4} \left(\frac{I_D}{I_G} \right)$$

(5-7)

In which λ_L is the laser excitation wavelength expressed in nm. The defect yield is equal to the defect density divided by the corresponding ion fluence. We use (1.8+0.5) in formula (5-7) to estimate the maximum defect yield.

Table 5.2 includes experimental data adapted from published work. These experimental defect yields are calculated from the low I_D/I_G (low fluence) results in Raman spectra.

Table 5.2 The Monte Carlo simulation and irradiation experiments results:

Ion	Energy	Mote Carlo Calculation Results	Experimental Results
C	500 keV	0.033/ion	0.032/ion [88]
He	3.04 MeV	3.6×10^{-4}/ion	2.6×10^{-4}/ion [101]
He	3 MeV	3.51×10^{-4}/ion	2.3×10^{-4}/ion [39]
Ag	100 MeV	3.5×10^{-3}/ion	2.3×10^{-3}/ion [90]
H	2 MeV	2.67×10^{-5}/ion	1.43×10^{-5}/ion [89]

The simulation results in Table 5.2 are the average of 10 independent Monte Carlo simulation results. For small defect yield, like 2 MeV H ions, $N = 10^7$ is used in the program to improve the precision of the simulation results.

The Monte Carlo simulation results are slightly larger than the experimental results. This is because we assume that all the scattered target carbon atoms collide with other carbon atoms in the graphene plane. A small percentage of carbon atoms with larger scattering angle leave the graphene plane after several collisions. On the other hand, the defect yield in experiments is by nature a random variable with its own distribution. The proposed Monte Carlo simulation can simulate this random process and give a satisfactory approximation of the experimental results in a short time.

In the Monte Carlo simulations, every ion is calculated with the assumption of no damage in the graphene. For example, the graphene is perfect and previous ions have no effect on subsequent ions. This assumption is rational when the defect density in the graphene is low. For instance, when the vacancy density in graphene increases, the average distance between two carbon atoms in the graphene increases. Hence the area of the red equilateral triangle shown in figure 11 increases. But the area of green rings is maintained constant. That means the probability P ($E_1 > E_d$) decreases and the defect yield is lower than what we get from the Monte Carlo simulation. It also means that the defect yield under irradiation decreases as the vacancy density in graphene increases.

The above discussion focuses on displacement damage defects in a beam environment. The space environment has ions and particles that are omnidirectional, as opposed to a beam environment where it is primarily the rare right-angle scattering events that lead to defects. This also involves: (1) knowledge of the relevant radiation environment (particle flux, energy, angular distribution, etc.), (2) translation of the external environment into the internal environment via the transport of the incident radiation through any materials or structures that surround the sensitive materials, and (3) energy deposition in the electronic materials by the impinging radiation [102]. These are now standard elements of error rate calculations due to single event effects caused by heavy ions and protons [102], [103]. It is relatively straightforward to extend the Monte Carlo approach described here, with suitable modifications to enable integration over

the full 4π environment, to obtain first-order estimates of defect densities in proton- and heavy-ion-irradiated graphene layers in realistic space environments.

This Monte Carlo simulation is used for monolayer graphene. It also can be used for estimating the defect yield in several layers of graphene since most of the ions with high incident energy "pass through" graphene layer with little energy loss. But as the number of graphene layer increases, the scattering angle of target carbon atom decrease and less cascade collisions occur in the graphene plane.

5.8   Conclusions

In this section, we used Monte Carlo simulations based on the molecular structure of graphene and in-plane cascade collision models to study the production of defects in graphene under energetic ion irradiation. We identified the types and concentrations of defects that appear in graphene under impacts of various ions with energies ranging from hundreds of eV to MeV and showed that all defects generated by ions with high incident energy are formed via head on collision and in-plane recoils, which is unique for two-dimensional materials. Finally, we compared the Monte Carlo simulation results with molecular dynamic simulation results and experimental results. The agreement between MC simulation results and experimental observations suggest that the Monte Carlo simulation is powerful and efficient analysis tool for defect evaluation and control in irradiated graphene.

CHAPTER VI

6. SUMMARY AND PERSPECTIVES FOR FUTURE WORK

6.1   Summary of Main Results

The present work yielded the following results for radiation effects on MEMS:

- The pMUT resonant frequency and quality factor response to 10 keV X-ray irradiation are investigated in this work. The impedances of pMUTs under irradiation were measured and corresponding equivalent electrical parameters were derived though curve fitting. The mechanical resonant frequency and quality factor of pMUTs were derived from equivalent LRC circuits. The resonant frequency and quality factor change with the irradiation dose. The worst case for TID effects in these pMUTs is positive bias during the radiation. The bias-dependent transport and trapping of radiation-induced charge near the electrodes and the resulting changes in stress and strain of the PZT are responsible for these changes.

- Responses of Al/SiO$_2$ bimorph electrothermal micros-canners to 10 keV X ray and 14.3 MeV oxygen ion irradiation have been investigated. Results demonstrate the dependence of microscanner displacement on total ionizing dose and/or applied-voltage induced charge trapping in dielectric layers. The resulting electrostatic forces lead to changes in resistance, position, and orientation of the microscanner. These results emphasize that radiation effects on electrothermal MEMS with dielectric layers must be considered for potential space applications that require high resolution and long-term reliability.

- A Monte Carlo simulation technique was developed based on molecular structure of graphene and in plane cascade collision model to study the defect production in graphene under energetic ion irradiation. We identified the types and concentrations of defects that appear in graphene under impacts of various ions with energies ranging from hundreds of electron volts to mega-electron volts and showed that all defects generated by ions with high incident energy are formed via head on collision and in-plane recoils, which is unique for two-dimensional materials. Finally, Monte Carlo simulation results were compared with molecular dynamic simulation results and experimental results. The agreement between Monte Carlo simulation results and experimental observations

suggest that the Monte Carlo simulation is powerful and efficient analysis tool for defect evaluation and control in graphene.

6.2   Perspectives for Future Work

The present work investigated radiation effects on piezoelectric, electrothermal and 2D materials. The present work provided fundamental knowledge about interaction mechanisms and the models. To fully understand radiation effects on MEMS, the following factors should be considered in future research:

- The PZT based pMUTs dynamic response has been investigated. There are multiple piezoelectric materials, such as crystalline and amorphous Al_2O_3. Radiation effects on different piezoelectric materials should be investigated. For piezoelectric MEMS, displacement is also important for its applications. A piezoelectric actuator is a good device for the static stability research.

- The static responses of an electrothermal microscanner have been investigated. The dynamic responses of the microscanner is also attractive. How electrothermal MEMS resonant frequency varies with radiation dose is still unknown. Also, there are many different combination of bimorph materials. More works are needed to understand the radiation effects on these combinations of bimorph materials.

- The Monte Carlo approach is applied on graphene. By considering the different molecular structures of other 2D materials, such as MoS_2, this approach can be used to calculate defects of 2D materials generated by energetic ions. Also, the defects generated in multiple 2D materials can be predicted by using this approach.

- There are many kinds of MEMS and few radiation experiments have been conducted on these MEMS. The radiation effects can degrade MEMS electrical and mechanical properties at the same time. Radiation effects on MEMS must be carefully investigated before applied in environments that need high resolution and long-term reliability.

REFERENCES

[1]   C. N. Arutt, M. L. Alles, W. Liao *et al.*, "The study of radiation effects in emerging micro and nano electro mechanical systems (M and NEMs)," *Semiconductor Science and Technology,* vol. 32, no. 1, pp. 013005, 2016.

[2]   R. Osiander, and A. Darrin, "MEMS enabling space exploration and exploitation," *MEMS for Automotive and Aerospace Applications*, pp. 311-330: Elsevier, 2013.

[3]   H. R. Shea, "Effects of radiation on MEMS," *Reliability, Packaging, Testing, and Characterization of MEMS/MOEMS and Nanodevices X,* vol. 7928, pp. 79280E, 2011.

[4]   T.-P. Ma, and P. V. Dressendorfer, *Ionizing radiation effects in MOS devices and circuits*: John Wiley & Sons, 1989.

[5]   H. L. Olesen, *Radiation effects on electronic systems*: Springer, 1966.

[6]   E. Stassinopoulos, and J. P. Raymond, "The space radiation environment for electronics," *Proceedings of the IEEE,* vol. 76, no. 11, pp. 1423-1442, 1988.

[7]   J. E. Gover, "Basic radiation effects in electronics technology. 1984 IEEE NSREC Short Course," *Colorado Springs, CO*, pp. 12-16, 1984.

[8]   H. Yanazawa, and K. Homma, "Growing market of MEMS and technology development in process and tools specialized to MEMS," *2017 IEEE Electron Devices Technology and Manufacturing Conference (EDTM)*, pp. 143-144, 2017.

[9]   B. Stark, "MEMS reliability assurance guidelines for space applications," *NASA Technical Reports*, no. 20000047448 pp. 1-312, 1999.

[10]   H. R. Shea, "Radiation sensitivity of microelectromechanical system devices," *Journal of Micro/Nanolithography, MEMS, and MOEMS,* vol. 8, no. 3, pp. 031303, 2009.

[11]   L. D. Edmonds, G. M. Swift, and C. I. Lee, "Radiation response of a MEMS accelerometer: an electrostatic force," *IEEE Transactions on Nuclear Science,* vol. 45, no. 6, pp. 2779-2788, 1998.

[12]   M. A. Beasley, S. L. Firebaugh, R. L. Edwards *et al.*, "MEMS thermal switch for spacecraft thermal control," *MEMS/MOEMS Components and Their Applications,* vol. 5344, pp. 98-106, 2004.

[13] S. Buchner, D. A. Rapchun, H. Moseley *et al.*, "Response of a MEMS microshutter operating at 60 K to ionizing radiation," *IEEE Transactions on Nuclear Science,* vol. 54, no. 6, pp. 2463-2467, 2007.

[14] W. Liao, E. X. Zhang, M. L. Alles *et al.*, "Total-ionizing-dose effects on piezoelectric micromachined ultrasonic transducers," *IEEE Transactions on Nuclear Science,* vol. 64, no. 1, pp. 233-238, 2017.

[15] G. Bahl, *Charge in Composite Micromechanical Resonators*: Stanford University, 2010.

[16] C. I. Lee, A. H. Johnston, W. C. Tang *et al.*, "Total dose effects on microelectromechanical systems (MEMS): Accelerometers," *IEEE Transactions on Nuclear Science,* vol. 43, no. 6, pp. 3127-3132, 1996.

[17] S. S. McClure, L. D. Edmonds, R. Mihailovich *et al.*, "Radiation effects in micro-electromechanical systems (MEMS): RF relays," *IEEE Transactions on Nuclear Science,* vol. 49, no. 6, pp. 3197-3202, 2002.

[18] O. Cournar, F. Miller, N. Buard *et al.*, "Total dose effects and SEE screening on MEMS COTS accelerometers," *Radiation Effects Data Workshop, 2004 IEEE*, pp. 125-129, 2004.

[19] A. R. Knudson, S. Buchner, P. McDonald *et al.*, "The effects of radiation on MEMS accelerometers," *IEEE Transactions on Nuclear Science,* vol. 43, no. 6, pp. 3122-3126, 1996.

[20] L. P. Schanwald, J. R. Schwank, J. J. Sniegowsi *et al.*, "Radiation effects on surface micromachined comb drives and microengines," *IEEE Transactions on Nuclear Science,* vol. 45, no. 6, pp. 2789-2798, 1998.

[21] R. R. Qian, Z. Y. Wen, and L. Chen, "A piezoelectrically actuated scaning micromirror integrated with angle sensors," *Key Engineering Materials,* vol. 483, pp. 437-442, 2011.

[22] P. Touboul, "Space accelerometers: present status," *Gyros, Clocks, Interferometers...: Testing Relativistic Graviy in Space*, pp. 273-291: Springer, 2001.

[23] S. C. Lee, G. Teowee, R. D. Schrimpf *et al.*, "Total-dose radiation effects on sol-gel derived PZT thin films," *IEEE Transactions on Nuclear Science,* vol. 39, no. 6, pp. 2036-2043, 1992.

[24] J. M. Benedetto, R. A. Moore, F. B. McLean *et al.*, "The effect of ionizing radiation on sol-gel ferroelectric PZT capacitors," *IEEE Transactions on Nuclear Science,* vol. 37, no. 6, pp. 1713-1717, 1990.

[25]   Y. Qiu, J. V. Gigliotti, M. Wallace *et al.*, "Piezoelectric micromachined ultrasound transducer (PMUT) arrays for integrated sensing, actuation and imaging," *Sensors,* vol. 15, no. 4, pp. 8020-8041, 2015.

[26]   S. P. Timoshenko, and S. Woinowsky-Krieger, "Theory of plates and shells," pp. 1-579, 1959.

[27]   P. M. Morse, and K. U. Ingard, "Theoretical acoustics," pp. 1-949, 1968.

[28]   S. Prasad, B. Sankar, L. Cattafesta *et al.*, "Two-port electroacoustic model of a piezoelectric circular composite plate," *43rd AIAA/ASME/ASCE/AHS/ASC Structures, Structural Dynamics, and Materials Conference*, pp. 1365, 2002.

[29]   Q. Gallas, R. Holman, T. Nishida *et al.*, "Lumped element modeling of piezoelectric-driven synthetic jet actuators," *AIAA journal,* vol. 41, no. 2, pp. 240-247, 2003.

[30]   R. A. Moore, J. M. Benedetto, J. M. McGarrity *et al.*, "Neutron irradiation effects on PZT thin films for nonvolatile-memory applications," *IEEE Transactions on Nuclear Science,* vol. 38, no. 6, pp. 1078-1082, 1991.

[31]   J. T. Graham, G. L. Brennecka, P. Ferreira *et al.*, "Neutron irradiation effects on domain wall mobility and reversibility in lead zirconate titanate thin films," *Journal of Applied Physics,* vol. 113, no. 12, pp. 124104, 2013.

[32]   Y. Bastani, A. Y. Cortes-Pena, A. D. Wilson *et al.*, "Effects of high energy x ray and proton irradiation on lead zirconate titanate thin films' dielectric and piezoelectric response," *Applied Physics Letters,* vol. 102, no. 19, pp. 192906, 2013.

[33]   S. J. Brewer, C. Z. Deng, C. P. Callaway *et al.*, "Effect of top electrode material on radiation-induced degradation of ferroelectric thin film structures," *Journal of Applied Physics,* vol. 120, no. 2, pp. 024101 1-9, 2016.

[34]   L. B. Freund, and S. Suresh, *Thin film materials: stress, defect formation and surface evolution*: Cambridge University Press, 2004.

[35]   E. W. Taylor, A. H. Paxton, H. Schone *et al.*, "Radiation-induced effects research in emerging photonic technologies: vertical cavity surface emitting lasers, GaN light-emitting diodes, and microelectromechanical devices," *Photonics for Space Environments V,* vol. 3124, pp. 9-22, 1997.

[36] M. Parameswaran, R. W. Johnstone, K. F. Ko *et al.*, "The effects of proton irradiation on electrothermal micro-actuators," *Canadian Journal of Electrical and Computer Engineering,* vol. 27, no. 1, pp. 3-5, 2002.

[37] J. R. Caffey, "The Effects of Ionizing Radiation on Microelectromechanical Systems (MEMS) Actuators: Electrostatic, Electrothermal, and Residual Stress," *Master dissertation, Defence Techinical Information Center, Air Force Institute of technology*, 2003.

[38] X. Zang, Q. Zhou, J. Chang *et al.*, "Graphene and carbon nanotube (CNT) in MEMS/NEMS applications," *Microelectronic Engineering,* vol. 132, pp. 192-206, 2015.

[39] K. Liu, C. L. Hsin, D. Fu *et al.*, "Self-passivation of defects: effects of high-energy particle irradiation on the elastic modulus of multilayer graphene," *Advanced Materials,* vol. 27, no. 43, pp. 6841-6847, 2015.

[40] J. Lee, M. J. Krupcale, and P. X.-L. Feng, "Effects of γ-ray radiation on two-dimensional molybdenum disulfide (MoS2) nanomechanical resonators," *Applied Physics Letters,* vol. 108, no. 2, pp. 023106, 2016.

[41] J. R. Lamarsh, *Introduction to nuclear reactor theory*: Addison Wesley Publishing Company, 1966.

[42] W. Liao, W. Liu, J. E. Rogers *et al.*, "Piezeoelectric micromachined ultrasound tranducer array for photoacoustic imaging," *Solid-State Sensors, Actuators and Microsystems (TRANSDUCERS & EUROSENSORS XXVII), 2013 Transducers & Eurosensors XXVII: The 17th International Conference on*, pp. 1831-1834, 2013.

[43] S. D. Senturia, *Microsystem design*: Springer Science & Business Media, 2007.

[44] W.-T. Hsu, "Recent progress in silicon MEMS oscillators," in 40th Annual Precise Time and Time Interval (PTTI) Meeting Reston, Virginia 2008, pp. 135-146.

[45] C. Jeong, S. Seok, B. Lee *et al.*, "A study on resonant frequency and Q factor tunings for MEMS vibratory gyroscopes," *Journal of Micromechanics and Microengineering,* vol. 14, no. 11, pp. 1530-1536, 2004.

[46] S. B. Majumder, B. Roy, R. S. Katiyar *et al.*, "Effect of acceptor and donor dopants on polarization components of lead zirconate titanate thin films," *Applied Physics Letters,* vol. 79, no. 2, pp. 239-241, 2001.

[47] J. Robertson, W. L. Warren, B. A. Tuttle *et al.*, "Shallow Pb3+ hole traps in lead zirconate titanate ferroelectrics," *Applied Physics Letters,* vol. 63, no. 11, pp. 1519-1521, 1993.

[48] M. V. Raymond, and D. M. Smyth, "Defects and charge transport in perovskite ferroelectrics," *Journal of Physics and Chemistry of Solids,* vol. 57, no. 10, pp. 1507-1511, 1996.

[49] B. M. Gol'tsman, V. K. Yarmarkin, and V. V. Lemanov, "Influence of mobile charged defects on the dielectric non-linearity of thin ferroelectric PZT films," *Physics of the Solid State,* vol. 42, no. 6, pp. 1116-1119, 2000.

[50] J. Robertson, "Band structures and band offsets of high K dielectrics on Si," *Applied Surface Science,* vol. 190, no. 1-4, pp. 2-10, 2002.

[51] J. R. Schwank, R. D. Nasby, S. L. Miller *et al.*, "Total-dose radiation-induced degradation of thin film ferroelectric capacitors," *IEEE Transactions on Nuclear Science,* vol. 37, no. 6, pp. 1703-1712, 1990.

[52] D. M. Fleetwood, "Radiation-induced charge neutralization and interface-trap buildup in metal-oxide-semiconductor devices," *Journal of Applied Physics,* vol. 67, no. 1, pp. 580-583, 1990.

[53] Q.-M. Wang, T. Zhang, Q. Chen *et al.*, "Effect of DC bias field on the complex materials coefficients of piezoelectric resonators," *Sensors and Actuators A: Physical,* vol. 109, no. 1-2, pp. 149-155, 2003.

[54] D. A. Parks, and B. R. Tittmann, "Ultrasonic NDE in a reactor core," *Sensors, 2011 IEEE*, pp. 618-622, 2011.

[55] W. Liao, E. X. Zhang, M. L. Alles *et al.*, "Total Ionization Effects on Al/SiO$_2$ Bimorph Electrothermal Microscanner," *IEEE Transactions on Nuclear Science,* vol. 65, no. 8, pp. 2260-2267, 2018.

[56] S. Janson, H. Helvajian, and K. Breuer, "MEMS, microengineering and aerospace systems," *30th Fluid Dynamics Conference*, pp. 3802-3806, 1999.

[57] C. Lee, and C.-Y. Wu, "Study of electrothermal V-beam actuators and latched mechanism for optical switch," *Journal of Micromechanics and Microengineering,* vol. 15, no. 1, pp. 11-19, 2004.

[58]   A. Espinosa, K. Rabenorosoa, C. Clevy *et al.*, "Piston motion performance analysis of a 3DOF electrothermal MEMS scanner for medical applications," *International Journal of Optomechatronics,* vol. 8, no. 3, pp. 179-194, 2014.

[59]   S. B. Dutta, A. J. Ewin, M. D. Jhabvala *et al.*, "Development of individually addressable micromirror arrays for space applications," *MOEMS and Miniaturized Systems,* vol. 4178, pp. 365-372, 2000.

[60]   J. L. Champion, R. Osiander, M. A. Darrin *et al.*, "MEMS louvers for thermal control," *Integrated Micro/Nano Technology for Spacecraft Applications*, Document ID: 19990067639, Report Number: PCN-545-91486, 1998.

[61]   C. T. Scalione, H. Swenson, F. DeLuccia *et al.*, "Design evolution of the NPOESS VIIRS instrument since CDR," *Geoscience and Remote Sensing Symposium, 2003. IGARSS'03. Proceedings. 2003 IEEE International,* vol. 5, pp. 3039-3042, 2003.

[62]   K. Jia, S. Pal, and H. Xie, "An electrothermal tip–tilt–piston micromirror based on folded dual S-shaped bimorphs," *Journal of Microelectromechanical Systems,* vol. 18, no. 5, pp. 1004-1015, 2009.

[63]   S. T. Todd, A. Jain, H. Qu *et al.*, "A multi-degree-of-freedom micromirror utilizing inverted-series-connected bimorph actuators," *Journal of Optics A: Pure and Applied Optics,* vol. 8, no. 7, pp. S352-S359, 2006.

[64]   K. Jia, "Development and applications of high fill-factor, small footprint MEMS micromirrors and micromirror arrays," University of Florida, 2009.

[65]   A. H. Johnston, "Super recovery of total dose damage in MOS devices," *IEEE Transactions on Nuclear Science,* vol. 31, no. 6, pp. 1427-1433, 1984.

[66]   J. R. Schwank, P. S. Winokur, P. J. McWhorter *et al.*, "Physical mechanisms contributing to device rebound," *IEEE Transactions on Nuclear Science,* vol. 31, no. 6, pp. 1434-1438, 1984.

[67]   D. M. Fleetwood, and H. A. Eisen, "Total-dose radiation hardness assurance," *IEEE Transactions on Nuclear Science,* vol. 50, no. 3, pp. 552-564, 2003.

[68]   D. M. Fleetwood, "Total ionizing dose effects in MOS and low-dose-rate-sensitive linear-bipolar devices," *IEEE Transactions on Nuclear Science,* vol. 60, no. 3, pp. 1706-1730, 2013.

[69]   M. W. McCurdy, M. H. Mendenhall, R. A. Reed *et al.*, "Vanderbilt Pelletron-low energy protons and other ions for radiation effects on electronics," *2015 IEEE Radiation Effects Data Workshop (REDW)*, pp. 146-151, 2015.

[70]   C. Lee, A. Johnston, W. Tang *et al.*, "Total dose effects on microelectromechanical systems (MEMS): Accelerometers," *IEEE Transactions on Nuclear Science,* vol. 43, no. 6, pp. 3127-3132, 1996.

[71]   SRIM: http://www.srim.org.

[72]   H. E. Boesch, F. B. McLean, J. M. McGarrity *et al.*, "Hole transport and charge relaxation in irradiated SiO_2 MOS Capacitors," *IEEE Transactions on Nuclear Science,* vol. 22, no. 6, pp. 2163-2167, 1975.

[73]   J. P. Watt, G. F. Davies, and R. J. O'Connell, "The elastic properties of composite materials," *Reviews of Geophysics,* vol. 14, no. 4, pp. 541-563, 1976.

[74]   W. Liao, W. Liu, Y. Zhu *et al.*, "A tip-tilt-piston micromirror with symmetrical lateral-shift-free piezoelectric actuators," *IEEE Sensors Journal,* vol. 13, no. 8, pp. 2873-2881, 2013.

[75]   J.-T. Lin, P. D. Shuvra, W. Liao *et al.,* "Surface carrier concentration effect on elastic modulus of piezoelectric MEMS silicon cantilevers," *Solid-State Sensors, Actuators and Microsystems (TRANSDUCERS), 2017 19th International Conference on*, pp. 1175-1178, 2017.

[76]   Z. Marka, S. K. Singh, W. Wang *et al.*, "Characterization of X-ray radiation damage in $Si/SiO_2/$structures using second-harmonic generation," *IEEE Transactions on Nuclear Science,* vol. 47, no. 6, pp. 2256-2261, 2000.

[77]   A. R. Frederickson, "Upsets related to spacecraft charging," *IEEE Transactions on Nuclear science,* vol. 43, no. 2, pp. 426-441, 1996.

[78]   H. Zhu, *Graphene: Fabrication, Characterizations, Properties and Applications*: Academic Press, 2017.

[79]   S. Maharubin, X. Zhang, F. Zhu *et al.*, "Synthesis and applications of semiconducting graphene," *Journal of Nanomaterials,* vol. 2016, 2016.

[80]   K. S. Kim, Y. Zhao, H. Jang *et al.*, "Large-scale pattern growth of graphene films for stretchable transparent electrodes," *Nature,* vol. 457, no. 7230, pp. 706-710, 2009.

[81] J. S. Bunch, A. M. Van Der Zande, S. S. Verbridge *et al.*, "Electromechanical resonators from graphene sheets," *Science,* vol. 315, no. 5811, pp. 490-493, 2007.

[82] S. K. Min, W. Y. Kim, Y. Cho *et al.*, "Fast DNA sequencing with a graphene-based nanochannel device," *Nature Nanotechnology,* vol. 6, no. 3, pp. 162-165, 2011.

[83] A. Hashimoto, K. Suenaga, A. Gloter *et al.*, "Direct evidence for atomic defects in graphene layers," *Nature,* vol. 430, no. 7002, pp. 870-873, 2004.

[84] E. X. Zhang, A. Newaz, B. Wang *et al.*, "Low-energy X-ray and ozone-exposure induced defect formation in graphene materials and devices," *IEEE Transactions on Nuclear Science,* vol. 58, no. 6, pp. 2961-2967, 2011.

[85] J.-H. Chen, W. G. Cullen, C. Jang *et al.*, "Defect scattering in graphene," *Physical Review Letters,* vol. 102, no. 23, pp. 236805, 2009.

[86] F. Hao, D. Fang, and Z. Xu, "Mechanical and thermal transport properties of graphene with defects," *Applied Physics Letters,* vol. 99, no. 4, pp. 041901, 2011.

[87] F. Banhart, J. Kotakoski, and A. V. Krasheninnikov, "Structural defects in graphene," *ACS Nano,* vol. 5, no. 1, pp. 26-41, 2010.

[88] G. Compagnini, F. Giannazzo, S. Sonde *et al.*, "Ion irradiation and defect formation in single layer graphene," *Carbon,* vol. 47, no. 14, pp. 3201-3207, 2009.

[89] S. Mathew, T. Chan, D. Zhan *et al.*, "The effect of layer number and substrate on the stability of graphene under MeV proton beam irradiation," *Carbon,* vol. 49, no. 5, pp. 1720-1726, 2011.

[90] S. Kumar, A. Tripathi, F. Singh *et al.*, "Purification/annealing of graphene with 100-MeV Ag ion irradiation," *Nanoscale Research Letters,* vol. 9, no. 1, pp. 126-134, 2014.

[91] N. Jing, Q. Xue, C. Ling *et al.*, "Effect of defects on Young's modulus of graphene sheets: a molecular dynamics simulation," *Rsc Advances,* vol. 2, no. 24, pp. 9124-9129, 2012.

[92] L. Liu, M. Qing, Y. Wang *et al.*, "Defects in graphene: generation, healing, and their effects on the properties of graphene: a review," *Journal of Materials Science & Technology,* vol. 31, no. 6, pp. 599-606, 2015.

[93] W. Eckstein, *Computer simulation of ion-solid interactions*, p.^pp. 32-36: Springer Science & Business Media, 2013.

[94] G. H. Kinchin, and R. S. Pease, "The displacement of atoms in solids by radiation," *Reports on Progress in Physics,* vol. 18, no. 1, pp. 1-51, 1955.

[95]   A. Merrill, C. D. Cress, J. E. Rossi *et al.*, "Threshold displacement energies in graphene and single-walled carbon nanotubes," *Physical Review B,* vol. 92, no. 7, pp. 075404, 2015.

[96]   W. Li, X. Wang, X. Zhang *et al.*, "Mechanism of the defect formation in supported graphene by energetic heavy ion irradiation: the substrate effect," *Scientific Reports,* vol. 5, pp. 9935, 2015.

[97]   L. Ossi, "Irradiation effects in graphene and related materials," University of Helsinki, 2011.

[98]   O. Lehtinen, J. Kotakoski, A. V. Krasheninnikov *et al.*, "Effects of ion bombardment on a two-dimensional target: atomistic simulations of graphene irradiation," *Physical Review B,* vol. 81, no. 15, pp. 153401, 2010.

[99]   L. G. Cançado, A. Jorio, E. M. Ferreira *et al.*, "Quantifying defects in graphene via Raman spectroscopy at different excitation energies," *Nano Letters,* vol. 11, no. 8, pp. 3190-3196, 2011.

[100]   E. X. Zhang, A. M. Newaz, B. Wang *et al.*, "Ozone-exposure and annealing effects on graphene-on-SiO2 transistors," *Applied physics letters,* vol. 101, no. 12, pp. 121601, 2012.

[101]   J.-H. Kim, J. H. Hwang, J. Suh *et al.*, "Work function engineering of single layer graphene by irradiation-induced defects," *Applied Physics Letters,* vol. 103, no. 17, pp. 171604, 2013.

[102]   R. A. Weller, M. H. Mendenhall, R. A. Reed *et al.*, "Monte Carlo simulation of single event effects," *IEEE Transactions on Nuclear Science,* vol. 57, no. 4, pp. 1726-1746, 2010.

[103]   R. A. Reed, R. A. Weller, M. H. Mendenhall *et al.*, "Physical processes and applications of the Monte Carlo radiative energy deposition (MRED) code," *IEEE Transactions on Nuclear Science,* vol. 62, no. 4, pp. 1441-1461, 2015.